

Interplay of Magnetism, Superconductivity and Charge density wave in $\text{Lu}_2\text{Ir}_3\text{Si}_5$ and $\text{R}_2\text{Ir}_3\text{Sn}_5$ (R=rare earth) Compounds

A thesis submitted to the
Indian Institute of Technology Guwahati
for the degree of
Doctor of Philosophy in Physics

by

Sangeetha N. S.

Thesis Supervisors

Dr. Dilip Pal & Prof. Saurabh Basu



Department of Physics
Indian Institute of Technology Guwahati
Guwahati-781039, India

August 2012





dedicated to my beloved parents



DECLARATION

I hereby declare that this thesis entitled “**Interplay of Magnetism, Superconductivity and Charge density wave in $\text{Lu}_2\text{Ir}_3\text{Si}_5$ and $\text{R}_2\text{Ir}_3\text{Sn}_5$ (R=rare earth) Compounds**” is the result of my own research except as cited in the references. This thesis has not been accepted for any degree and is not concurrently submitted in candidature of any other degree. The work was done under the guidance of Dr. Dilip Pal and Prof. Saurabh Basu at Indian Institute of Technology Guwahati.

Sangeetha N. S.

Research student (Roll# 07612104)

Solid State lab

Department of Physics

Indian Institute of Technology Guwahati

Guwahati-781039, Assam



CERTIFICATE

It is certified that the work contained in the thesis entitled “**Interplay of Magnetism, Superconductivity and Charge density by wave in $\text{Lu}_2\text{Ir}_3\text{Si}_5$ and $\text{R}_2\text{Ir}_3\text{Sn}_5$ (R=rare earth) Compounds**” by Sangeetha N. S, a student of Department of Physics, Indian Institute of Technology Guwahati, for the award of the degree of Doctor of Philosophy has been carried out under our supervision. This work has not been submitted elsewhere for any degree.

Dr. Dilip Pal

Assistant Professor
Department of Physics
IIT Guwahati
Guwahati-781039, India

Prof. Saurabh Basu

Professor
Department of Physics
IIT Guwahati
Guwahati-781039, India



Acknowledgments

First and foremost, I would like to express my respect and gratitude towards my thesis supervisors Dr. Dilip Pal and Prof. Saurabh Basu for providing me the opportunity to work under their guidance. Their involvement, enthusiasm and immense knowledge in research have been invaluable. Their guidance gave me right path in all the time of research and writing of this thesis.

I would like to extend my sincere gratitude towards Dr. Dilip Pal for providing me a good platform for the research. His dedicated help, advice, encouragement, and patience throughout my PhD are to be acknowledged. He was always very supportive and gave me the complete freedom to pursue my research. My special word of thanks should also go to Prof. Saurabh Basu for his tireless support, cooperation and for facilitating all the requirements, going out of his way. His constant guidance, motivation and support have always kept me going ahead.

I sincerely thank and appreciate the members of my doctoral review committee: Prof. S. Ravi, Dr. P. K. Padmanabhan, and Dr. Gopal Das, for periodically assessing my research work and providing insightful comments, and suggestions for its betterment.

I am grateful to Prof. S. Ramakrishnan for allowing me to work in his group and providing the access to various experimental facilities at Tata Institute of Fundamental Research (TIFR), Mumbai. Discussing the experimental results with him was very informative and fruitful. I also express my sincere thanks to Prof. A. Thamizhavel (TIFR) with whom I learnt various crystal growth techniques. Every discussion with him was very enlightening and helped to clear my concepts. I express my sincere thanks to Prof. A. K Grover, TIFR for various kind of support in my research work and for the nice hospitality during my stay at TIFR.

At this point I would also thanks Prof. C. V. Tomy, IIT Bombay with whom I performed the specific heat measurement using PPMS and Dr. A. M. Awasthi, IUC-DAEF, Indore for providing me the opportunity to use DSC set up to perform specific heat measurement for some of the samples.

I would like to express my sincere gratitude towards Dr. Tatak Nath Dey, IITG for his immense support during the submission of my PhD thesis.

Thanks to Mr. Basab for his help in various ways and other staff members in the Physics Department, IITG for their nice co-operations.

I would also like to take this opportunity to thank Sannabhaditji, Anil and Ruta, scientific staff members at TIFR, for their help in characterization of my samples. I am thankful to Low Temperature Facility at TIFR for their nice cooperation.

I would like to thank my colleagues and friends at IITG, Aneesh, Suresh, Shyni, Sunita, Arpita, Santhosh, Padam Rajender, Munendhar, Rahul, Bhargav, Poulumi, Pc Mapuia, Tribedi, my seniors Meera, Veena, Poulumi, Sabita, Sunish and all others who helped me some way or other during my stay at IITG. The list wont be completed unless I add Resmi and Gauri, with you guys I had a whale of time at Subansiri. Thanks for just being around.

My special thanks to Dr. Naren who helped me a lot for carrying out my experiments at TIFR. I am also thankful to Neeraj, Bhanu Joshi, Om Prakash and Pranav for their cooperation and help in the lab. The supports and help received from Dr. Nagalakshmi, Dr. Devang Joshi, Dr. Prasanna, Dr. Pradip Das and Dr. Ravi Prakash Singh are also to be acknowledged.

The thesis would not have seen the light of this day without the support and perseverance of my teachers from C.M.S college, Kottayam and Sree Krishna College, Guruvayur. I would like to thank Dr. Rajan K. John who inspired me by the way of his teaching, dedication and sincerity. His constant motivation and support made me to reach this point. Thanks to Prof. M. K. Menon who at various stages motivated me to venture into doing a PhD. I must thank many of my B. Sc and M. Sc friends- Soumya, Vineetha, Melvi, Gopi, Remya, Sanoop, Vijitha, Linsha and Sreekala for their constructive criticisms and accompanying me during the filp-flops of my life. At this point, I remember the wonderful days I spent at SKC.

Last but not least, I express my love and respects towards my parents for their understanding, encouragement and patience in my every endeavour. I feel privileged to have a loving, caring and supportive family -my parents, brother and grandma. I would only say that this thesis is a result of their love and blessings.

Sangeetha N. S
IIT Guwahati
August 2012

Contents

Synopsis	9
List of Publications	15
1 Introduction	17
1.1 Rare Earth Magnetism	18
1.1.1 The Rare Earth Metals (RE)	18
1.1.2 The transition Metals (TM)	20
1.1.3 Magnetism in RE-TM alloys	20
1.1.4 The Kondo effect	22
1.2 Superconductivity	23
1.3 Charge Density Wave	25
1.3.1 Charge density wave Materials and Experiments	28
1.3.2 Coexistence of Superconductivity and the Charge Density Wave Ordering	32
1.4 Outline of the thesis	35
2 Experimental Techniques	37
2.1 Sample Preparation and characterization	37
2.2 Measurement Techniques	40
2.2.1 Electrical Resistivity Measurements	40
2.2.2 Magnetic Susceptibility Measurements	41
2.2.3 Heat Capacity Measurements	42
2.2.4 Differential Scanning Calorimetry	42
3 Interplay of superconductivity and charge density wave ordering in $\text{Lu}_2\text{Ir}_3(\text{Si}_{1-x}\text{Ge}_x)_5$, $\text{Lu}_2(\text{Ir}_{1-x}\text{Rh}_x)_3\text{Si}_5$ and $(\text{Lu}_{1-x}\text{Sc}_x)_2\text{Ir}_3\text{Si}_5$ systems	45
3.1 Introduction: CDW transition in $\text{Lu}_2\text{Ir}_3\text{Si}_5$	45
3.2 Experiment	47
3.3 Results	48
3.3.1 $\text{Lu}_2\text{Ir}_3(\text{Si}_{1-x}\text{Ge}_x)_5$	48
3.3.2 $\text{Lu}_2(\text{Ir}_{1-x}\text{Rh}_x)_3\text{Si}_5$	62
3.3.3 $(\text{Lu}_{1-x}\text{Sc}_x)_2\text{Ir}_3\text{Si}_5$	70
3.4 Discussion	75
3.5 Summary	79

4	Interplay of charge density wave and superconductivity in $\text{Lu}_2\text{Ir}_3\text{Si}_5$ single crystal	81
4.1	Introduction	81
4.2	Experiment	81
4.3	Result & Discussion	82
4.3.1	X-ray studies	82
4.3.2	Electrical resistivity	84
4.3.3	Magnetic susceptibility	86
4.3.4	Heat capacity	89
4.4	Summary	93
5	Magnetic ordering and crystal field effects in the $\text{R}_2\text{Ir}_3\text{Sn}_5$ (R=La-Nd, Gd-Tm) system	95
5.1	Introduction	95
5.2	Experiment	96
5.3	Results	98
5.3.1	Magnetic susceptibility and magnetization studies	98
5.3.2	Resistivity studies of $\text{R}_2\text{Ir}_3\text{Sn}_5$ (R = La, Ce - Tm)	103
5.3.3	Heat capacity studies of $\text{R}_2\text{Ir}_3\text{Sn}_5$ (R = La - Tm)	107
5.3.4	Crystal - field analysis	110
5.4	Discussion	115
5.5	Summary	118
6	Transport and Magnetic properties of $\text{Ce}_2\text{Ir}_3\text{Sn}_5$ single crystal	121
6.1	Introduction	121
6.2	Experiment	122
6.3	Results & Discussion	122
6.3.1	Resistivity studies	124
6.3.2	Magnetic susceptibility studies	126
6.3.3	Heat-capacity studies	129
6.4	Summary	130
7	Conclusion	131
	Bibliography	137

List of Figures

0.1	Plot of T_{CDW} and T_{SC} versus Ge concentration (x) for $\text{Lu}_2\text{Ir}_3(\text{Si}_{1-x}\text{Ge}_x)_5$ ($x = 0.00, 0.004, 0.01, 0.02, 0.05, 0.1, 0.15$ and 0.2).	11
0.2	Plot of T_{CDW} and T_{SC} versus Rh concentration (x) for $\text{Lu}_2(\text{Ir}_{1-x}\text{Rh}_x)_3\text{Si}_5$ with $x = 0.00, 0.01, 0.03, 0.1, 0.2$ and 0.3	12
0.3	Plot of T_{CDW} and T_{SC} versus Sc concentration (x) for $(\text{Lu}_{1-x}\text{Sc}_x)_2\text{Ir}_3\text{Si}_5$ with $x = 0.02, 0.04$ and 0.05	13
1.1	(a) A schematic representation of the atomic orbitals of a rare-earth atom with the circles indicating the approximate positions of the charge density maxima. The $5s-5p$ orbit illustrates the size of the Xenon core. (b) Radial distribution of different atomic orbitals in the Ce atom [<i>courtesy</i> [25]].	19
1.2	The qualitative temperature variation of the resistivity and susceptibility of a single ion Kondo system.	23
1.3	Peierls transition in a one-dimensional metal with a half filled band is demonstrated, (a) Energy dispersion of undistorted metal shown within the first Brillouin zone, E_F is Fermi level, k_F is Fermi wave vector, a is lattice constant, T_P Peierls transition temperature and the same for (b) Peierls insulator with Δ representing half of the gap that opens at the Fermi level [14].	26
1.4	Fermi surface nesting of electron systems of (a) 1D, (b) 2D, (c) 3D and (d) warped 1D FS. The arrows indicate pairs of states, one full and one empty, differing by the vector $q=2k_F$ [<i>courtesy</i> [14]].	27
1.5	The schematic chain structure of the NbSe_3 compounds. (a) The stacking of the prisms along the b -axis in the NbSe_3 structure (b) A projection of the NbSe_3 structure perpendicular to the b -axis [<i>courtesy</i> [46]].	29
1.6	The crystal structure of RTe_n . The axes are shown for convenience [<i>courtesy</i> [47]].	30
1.7	The crystal structure of $\text{Lu}_5\text{Ir}_4\text{Si}_{10}$ [<i>courtesy</i> [48]].	31
1.8	Signatures of a CDW transition is demonstrated (a) The temperature dependence of the dc resistivity of NbSe_3 [46]. Note the increase of ρ_{dc} at $T_{CDW}^1 = 149$ K and $T_{CDW}^2 = 59$ K. (b) The magnetic susceptibility of NbSe_3 shows a decrease below 150 K which are associated with the upper CDW transition [49]. (c) The specific heat of NbSe_3 as a function of temperature: top scale for T_{CDW}^1 ; bottom scale for T_{CDW}^2 [<i>courtesy</i> [50]].	32
1.9	Pressure dependence of the CDW ordering, T_{CDW} and SC transition temperature, T_{SC} in 2H- NbSe_2 [<i>courtesy</i> [58]].	34

2.1	(a) A schematic diagram of the Czochralski growth arrangement. (b) Experimental set up of tetra-arc furnace and the photograph taken during crystal growth.	38
2.2	(a) A schematic of Laue Diffraction machine used to align the crystals. (b) Triple axis goniometer, where the sample is mounted on to fix a crystallographic axis. (c) Experimental set up of the Laue diffraction machine. . . .	39
2.3	A schematic block diagram of the resistivity set up via a four probe technique. At a time four different samples can be measured.	41
3.1	The crystal structure of $\text{Lu}_2\text{Ir}_3\text{Si}_5$. The large (red) spheres correspond to the Lu atom, Ir atoms with medium (yellow) spheres and Si atoms with small (green) spheres.	46
3.2	Powder x-ray diffraction data of the $\text{Lu}_2\text{Ir}_3\text{Si}_{4.95}\text{Ge}_{0.05}$. The solid line represents the simulated data using FULLPROF (Reitveld Program).	49
3.3	Ge (x) concentration dependence of the c/a ratio and volume for $\text{Lu}_2\text{Ir}_3(\text{Si}_{1-x}\text{Ge}_x)_5$, ($x = 0.00, 0.004, 0.01, 0.02, 0.05, 0.1, 0.15$ and 0.2).	49
3.4	The temperature dependence of the dc susceptibility for the samples of $\text{Lu}_2\text{Ir}_3(\text{Si}_{1-x}\text{Ge}_x)_5$ with $x = 0.00, 0.004, 0.01$ and 0.02 . The left panels demonstrate low temperature behavior of dc susceptibility which highlights superconducting transition. The right panels show the CDW transition for these samples.	51
3.5	The temperature dependence of the dc susceptibility for the samples of $\text{Lu}_2\text{Ir}_3(\text{Si}_{1-x}\text{Ge}_x)_5$ with $x = 0.05, 0.1, 0.15$ and 0.2 . The left panel demonstrates low temperature behavior of dc susceptibility which highlights superconducting transition. The right panels panel show the CDW transition.	52
3.6	The temperature dependence of the electrical resistivity for $\text{Lu}_2\text{Ir}_3(\text{Si}_{1-x}\text{Ge}_x)_5$ with $x = 0.00, 0.004, 0.01$ and 0.02 . The main panels shows the variation of resistivity from 1.8 to 300 K. The insets show resistivity data between 1.8 to 9 K to highlight SC transition.	53
3.7	The temperature dependence of the electrical resistivity for $\text{Lu}_2\text{Ir}_3(\text{Si}_{1-x}\text{Ge}_x)_5$ with $x = 0.05, 0.1, 0.15$ and 0.2 . The main panels shows the variation of resistivity from 1.8 to 300 K. The insets show resistivity data between 1.8 to 9 K to highlight SC transition.	54
3.8	The temperature dependence of the specific heat for $\text{Lu}_2\text{Ir}_3(\text{Si}_{1-x}\text{Ge}_x)_5$ ($x = 0.00, 0.004, 0.01$ and 0.02). The main panels demonstrates the data from 120 to 300 K. The fit to model is shown in upper two panels by a continuous line. In second panel, the step change in specific heat is shown clearly.	58
3.9	The temperature dependence of the specific heat for $\text{Lu}_2\text{Ir}_3(\text{Si}_{1-x}\text{Ge}_x)_5$ ($x = 0.05, 0.1, 0.15$ and 0.2) from 120 to 300 K. The peak is the signature of the CDW transition.	59
3.10	The temperature dependence of the ΔC_{CDW} and ΔS_{CDW} across CDW-ordering transitions for $\text{Lu}_2\text{Ir}_3(\text{Si}_{1-x}\text{Ge}_x)_5$ ($x = 0.00, 0.004, 0.01, 0.02, 0.05, 0.1, 0.15$ and 0.2).	61
3.11	Rh concentration (x) dependence of the volume for $\text{Lu}_2(\text{Ir}_{1-x}\text{Rh}_x)_3\text{Si}_5$ for $x = 0.00, 0.01, 0.03, 0.1, 0.2$ and 0.3	63

3.12	The temperature dependence of the dc susceptibility for the samples of $\text{Lu}_2(\text{Ir}_{1-x}\text{Rh}_x)_3\text{Si}_5$ ($x = 0.00, 0.01, 0.03, 0.1, 0.2$ and 0.3). The left panel shows the dc susceptibility data from 2 to 10 K and the right panels show the data from 100 to 300 K. . . .	64
3.13	The temperature dependence of the electrical resistivity for $\text{Lu}_2(\text{Ir}_{1-x}\text{Rh}_x)_3\text{Si}_5$ ($x = 0.00, 0.01, 0.03, 0.1, 0.2$ and 0.3). The left panel shows the resistivity data between 1.8 to 10 K indicating the SC transition. The right panel shows the data from 1.8 K till 300 K highlighting the CDW transition.	66
3.14	Plot of specific heat versus temperature for $\text{Lu}_2(\text{Ir}_{1-x}\text{Rh}_x)_3\text{Si}_5$ ($x = 0.00, 0.01, 0.03, 0.1, 0.2$ and 0.3). The main panels demonstrate the data from 150 to 300 K. The solid line is the fit to the critical fluctuation model (see text).	68
3.15	Plot of ΔC_{CDW} and ΔS_{CDW} versus temperature across CDW-ordering transitions for $\text{Lu}_2(\text{Ir}_{1-x}\text{Rh}_x)_3\text{Si}_5$ $x = 0.00, 0.01, 0.03, 0.1$, and 0.2	69
3.16	Plot of Sc (x) concentration versus volume for the pseudoternary system $(\text{Lu}_{1-x}\text{Sc}_x)_2\text{Ir}_3\text{Si}_5$ $x = 0.00, 0.02, 0.04$ and 0.05	70
3.17	Plot of the temperature dependence of the dc susceptibility of $(\text{Lu}_{1-x}\text{Sc}_x)_2\text{Ir}_3\text{Si}_5$ ($x = 0.02, 0.04$ and 0.05). The left panel demonstrates dc susceptibility data from 2 to 10 K and the right panel show the data from 50 K till 300 K.	71
3.18	The temperature dependence of the electrical resistivity for $(\text{Lu}_{1-x}\text{Sc}_x)_2\text{Ir}_3\text{Si}_5$ ($x = 0.02, 0.04$ and 0.05). The left panel shows the resistivity data between 1.8 to 10 K indicating the SC transition. The right panel shows the data from 1.8 K till 300 K highlighting the CDW transition.	73
3.19	(a) The temperature dependence of the specific heat for $(\text{Lu}_{1-x}\text{Sc}_x)_2\text{Ir}_3\text{Si}_5$ ($x = 0.02, 0.04$ and 0.05). The main panels demonstrate the data from 120 to 300 K. The solid line is the fit to the critical fluctuation model (see text). (b) Plot of ΔC_{CDW} and ΔS_{CDW} versus temperature across CDW-ordering transitions for $(\text{Lu}_{1-x}\text{Sc}_x)_2\text{Ir}_3\text{Si}_5$ ($x = 0.02, 0.04$ and 0.05).	74
3.20	Plot of T_{CDW} and T_{SC} vs Ge concentration (x) for $\text{Lu}_2\text{Ir}_3(\text{Si}_{1-x}\text{Ge}_x)_5$ ($x = 0.00, 0.004, 0.01, 0.02, 0.05, 0.1, 0.15$ and 0.2).	76
3.21	Plot of T_{CDW} and T_{SC} vs Rh concentration (x) for $\text{Lu}_2(\text{Ir}_{1-x}\text{Rh}_x)_3\text{Si}_5$ with $x = 0.00, 0.01, 0.03, 0.1, 0.2$ and 0.3	77
3.22	Plot of T_{CDW} and T_{SC} vs Sc concentration (x) for $(\text{Lu}_{1-x}\text{Sc}_x)_2\text{Ir}_3\text{Si}_5$ with $x = 0.02, 0.04$ and 0.05	78
4.1	The as grown crystal and observed and simulated Laue pattern of $\text{Lu}_2\text{Ir}_3\text{Si}_5$ along the [100] axis.	83
4.2	Powder x-ray diffraction data of $\text{Lu}_2\text{Ir}_3\text{Si}_5$. The solid line is the simulated data using FULLPROF (Reitveld Program).	84
4.3	The temperature dependence of the electrical resistivity $\rho(T)$ of $\text{Lu}_2\text{Ir}_3\text{Si}_5$. Main panels demonstrate the CDW transition at high temperatures, along the three principle axes, for both the cooling (shown by \leftarrow) and warming (shown by \rightarrow) of the sample. Inset shows the low temperature resistivity data between 2 and 6 K to look at the SC transition along a , b and c axes.	85

4.4	The temperature dependence of the dc susceptibility $\rho(T)$ of $\text{Lu}_2\text{Ir}_3\text{Si}_5$. (a), (b) and (c) demonstrate CDW transition at high temperatures along three principle axes (a , b and c) for both the cooling (shown by \leftarrow) and warming (shown by \rightarrow) of the sample. (d) The low temperature susceptibility data between 2 and 6 K to look at SC transition along a , b and c axes.	87
4.5	(a) The lower critical field $H_{C1}(T)$ and (b) the upper critical field $H_{C2}(T)$ vs temperature extracted from M vs H measurement for $\text{Lu}_2\text{Ir}_3\text{Si}_5$	88
4.6	The temperature dependence of specific heat measurements (DSC data) on both warming and cooling of $\text{Lu}_2\text{Ir}_3\text{Si}_5$ after subtracting the smooth background. (a) The agreement between data points (open circles) and fit (solid line) to the model of critical fluctuation plus a mean-field contribution in the vicinity of CDW transition. (b) The plot of $\Delta C_P/T$ vs T (left axis) and the entropy change ΔS (right axis) associated with the transition.	91
4.7	The specific heat capacities of $\text{Lu}_2\text{Ir}_3\text{Si}_5$ in the field of 9 T while warming. Inset shows the specific heat on an enlarged temperature scale (left axis) and the calculated entropy change around 230 K (right axis).	92
5.1	Crystal structure of the unit cell of the series $\text{R}_2\text{Ir}_3\text{Sn}_5$ (Ce: medium isolated red spheres, Ir : small yellow spheres and Sn: small green spheres).	97
5.2	Variation of inverse dc susceptibility (χ^{-1}) of $\text{R}_2\text{Ir}_3\text{Sn}_5$ ($\text{R} = \text{Ce} - \text{Gd}$) from 1.8 to 300 K in the field of 4 kOe. The inset shows the susceptibility (χ) behavior in low temperatures. The solid line is a fit to the Curie - Weiss relation.	99
5.3	Variation of inverse dc susceptibility (χ^{-1}) of $\text{R}_2\text{Ir}_3\text{Sn}_5$ ($\text{R} = \text{Tb} - \text{Tm}$) from 1.8 to 300 K in the field of 4 kOe. The inset shows the susceptibility (χ) behavior in low temperatures. The solid line is a fit to the Curie - Weiss relation.	100
5.4	Isothermal magnetization measurement of field dependence in $\text{R}_2\text{Ir}_3\text{Sn}_5$ series of compounds with $\text{R} = \text{Ce}, \text{Pr}, \text{Gd}$ and Tb	102
5.5	Isothermal magnetization measurement of field dependence in $\text{R}_2\text{Ir}_3\text{Sn}_5$ series of compounds with $\text{R} = \text{Dy}, \text{Ho}, \text{Er}, \text{Tm}$	102
5.6	The temperature dependence of resistivity (ρ) of $\text{R}_2\text{Ir}_3\text{Sn}_5$ ($\text{R} = \text{La} - \text{Nd}$ and Gd) from 1.8 to 300 K. The inset shows low temperature ρ data. The solid line in the main plots are fit to parallel resistor model.	103
5.7	The temperature dependence of resistivity (ρ) of $\text{R}_2\text{Ir}_3\text{Sn}_5$ ($\text{R} = \text{Tb} - \text{Tm}$) from 1.8 to 300 K. The inset shows low temperature ρ data. The solid line in the main plots are fit to parallel resistor model.	104
5.8	Temperature dependence of the heat capacity [(C_P) , marked by $(-\bigcirc-)$] of $\text{R}_2\text{Ir}_3\text{Sn}_5$ ($\text{R} = \text{La} - \text{Nd}$ and Gd) from 1.8 to 30 K. The calculated entropy S_{mag} [solid line] (after subtractions of lattice contribution from C_P of $\text{La}_2\text{Ir}_3\text{Sn}_5$) is shown in the right hand side of the same figure. The inset shows the low temperature C_{mag}/T vs T^2 data.	108

5.9	Temperature dependence of the heat capacity [(C_P) , marked by $(-\circ-)$] of $R_2Ir_3Sn_5$ ($R = Dy - Tm$) from 1.8 to 30 K. The calculated entropy S_{mag} [solid line] (after subtraction of lattice contribution from C_P of $La_2Ir_3Sn_5$) is shown in the right hand side of the same figure. The inset shows the low temperature C_{mag}/T vs T^2 data.	109
5.10	Plot of the magnetic contribution to the heat capacity (C_{mag}) and the entropy (S_{mag}) vs T of $R_2Ir_3Sn_5$ ($R = Pr, Nd, Dy, Ho, Er$ and Tm). The solid line are fit to the CEF model.	113
5.11	Variation of the inverse susceptibility of $R_2Ir_3Sn_5$ ($R = Pr, Nd, Dy, Ho, Er$ and Tm) series in a field of 4 kOe from 2 to 300 K. The solid lines are fits to the CEF model.	114
5.12	Plots of the ordering temperature of the compounds of the series $R_2Ir_3Sn_5$ ($R = Ce - Nd, Gd - Tm$) normalized to the T_N value for Gd . The dashed lines is the theoretical de Gennes scaling with only spin quantum number and the solid lines is related to de Gennes scaling with total angular momentum	118
6.1	The as-grown single crystal and Laue pattern of $Ce_2Ir_3Sn_5$ along the [010] direction. Right figure shows simulated pattern of Laue picture along the [010] axis.	123
6.2	Powder x-ray diffraction data of the $Ce_2Ir_3Sn_5$. The solid line is the simulated data using FULLPROF (Reitveld Program).	124
6.3	(a) The dc electrical resistivity in the temperature range from 1.8 to 300 K for $Ce_2Ir_3Sn_5$ along the [100], [010] and [001] directions. (b) Logarithmic temperature dependence of resistivity for $Ce_2Ir_3Sn_5$. Solid line at high temperature is a fit to the Kondo equation and the dotted line in low temperature part is a fit to Fermi liquid behaviour.	125
6.4	The inverse dc susceptibility in $Ce_2Ir_3Sn_5$ for $H \parallel [100], [010]$ and [001] directions in the temperature range from 1.8 K to 300 K in the field of 1 kOe. The inset shows the susceptibility (χ) behaviour in low temperature is shown in a log scale. The solid line is a fit to the Curie Weiss relation.	127
6.5	Isothermal magnetization curves of the magnetic field dependence in $Ce_2Ir_3Sn_5$ along [100], [010] and [001] axes.	128
6.6	The temperature dependence of the specific heat capacity of $Ce_2Ir_3Sn_5$. In Fig (a), main panel shows C vs T in the temperature range between 1.8 to 250 K and the inset shows specific heat fit in C/T vs T^2 plot. (b) C_{mag}/T vs T of $Ce_2Ir_3Sn_5$. The calculated entropy is plotted on the right axis.	129



List of Tables

3.1	Lattice parameters of $\text{Lu}_2\text{Ir}_3(\text{Si}_{1-x}\text{Ge}_x)_5$	48
3.2	CDW transition parameters obtained from the temperature dependence of the resistivity of $\text{Lu}_2\text{Ir}_3(\text{Si}_{1-x}\text{Ge}_x)_5$	55
3.3	Parameters obtained from the low temperature specific heat data of $\text{Lu}_2\text{Ir}_3(\text{Si}_{1-x}\text{Ge}_x)_5$	56
3.4	Parameters obtained from the specific heat data of $\text{Lu}_2\text{Ir}_3(\text{Si}_{1-x}\text{Ge}_x)_5$	57
3.5	The fitting parameters extracted from the specific heat data of $\text{Lu}_2\text{Ir}_3(\text{Si}_{1-x}\text{Ge}_x)_5$ using the model of critical fluctuations and mean-field contributions.	62
3.6	Lattice parameters of $\text{Lu}_2(\text{Ir}_{1-x}\text{Rh}_x)_3\text{Si}_5$	63
3.7	CDW transition parameters obtained from the temperature dependence of the resistivity data of $\text{Lu}_2(\text{Ir}_{1-x}\text{Rh}_x)_3\text{Si}_5$	65
3.9	Parameters obtained from the high temperature specific heat data of $\text{Lu}_2(\text{Ir}_{1-x}\text{Rh}_x)_3\text{Si}_5$	67
3.8	Parameters obtained from the low temperature specific heat data of $\text{Lu}_2(\text{Ir}_{1-x}\text{Rh}_x)_3\text{Si}_5$	68
3.10	The fitting parameters extracted from the specific heat data of $\text{Lu}_2(\text{Ir}_{1-x}\text{Rh}_x)_3\text{Si}_5$ using the model of critical fluctuations and mean-field contributions.	69
3.11	Lattice parameters of $(\text{Lu}_{1-x}\text{Sc}_x)_2\text{Ir}_3\text{Si}_5$	70
3.12	Parameters obtained from the temperature dependence of the resistivity of $(\text{Lu}_{1-x}\text{Sc}_x)_2\text{Ir}_3\text{Si}_5$ near the CDW region.	72
3.13	Parameters obtained from the specific heat data of $(\text{Lu}_{1-x}\text{Sc}_x)_2\text{Ir}_3\text{Si}_5$ near the CDW region.	74
3.14	The fitting parameters extracted from the specific heat data of $(\text{Lu}_{1-x}\text{Sc}_x)_2\text{Ir}_3\text{Si}_5$ using a model of critical fluctuations and mean-field contributions near CDW region.	75
4.1	Refined crystallographic parameters for $\text{Lu}_2\text{Ir}_3\text{Si}_5$ using room temperature powder x-ray diffraction data.	82
4.2	CDW transition parameters obtained from the temperature dependence of the resistivity of $\text{Lu}_2\text{Ir}_3\text{Si}_5$	86
4.3	CDW transition parameters obtained from the temperature dependence of the dc susceptibility of $\text{Lu}_2\text{Ir}_3\text{Si}_5$	88
4.4	Different superconducting parameters of $\text{Lu}_2\text{Ir}_3\text{Si}_5$ are noted.	89
4.5	Summary of specific heat anomalies of $\text{Lu}_2\text{Ir}_3\text{Si}_5$ compared to the well-studied CDW systems $\text{K}_{0.3}\text{MoO}_3$ and NbSe_3	90
4.6	The fitting parameters extracted from the specific heat data of $\text{Lu}_2\text{Ir}_3\text{Si}_5$ to a model of critical fluctuations in addition to mean-field contributions.	91
5.1	Lattice parameters of $\text{R}_2\text{Ir}_3\text{Sn}_5$	98

5.2	$R_2Ir_3Sn_5$ compounds obtained from the high temperature susceptibility fit to Curie - Weiss relation. μ_{th} is the theoretical free ion value for trivalent rare - earth ions.	101
5.3	Transition temperatures T_N observed from different measurement techniques.	105
5.4	Parameters obtained from power law fit in low temperature resistivity for $R_2Ir_3Sn_5$	105
5.5	$R_2Ir_3Sn_5$ series at high temperature ($100 < T < 300$ K) using parallel resistor model. $\theta_D(HC)$ is observed from heat capacity studies.	107
5.6	Parameters obtained from heat capacity studies of $R_2Ir_3Sn_5$	110
5.7	Parameters obtained from CEF fit.	113
6.1	The fitting parameters extracted from the resistivity data of $Ce_2Ir_3Sn_5$. . .	126
6.2	$Ce_2Ir_3Sn_5$ compounds along three different principle axes, [100], [010] and [001], obtained from the high temperature susceptibility fit to Curie Weiss relation. μ_{th} is the theoretical free ion value for trivalent rare earth ions. . .	127



Synopsis

Intermetallic compounds based on rare-earth (R) and 3*d* transition (T) elements have attracted considerable research interest for several decades owing to the fascinating physical phenomena that they exhibit. One observes various unusual ground states like, Kondo behavior, large positive magnetoresistance, valence fluctuation, superconductivity, re-entrant superconductivity, charge/spin density wave (CDW/SDW), topological superconductors etc.. Such ground states can also compete/coexist with each other, such as coexistence of superconductivity and CDW/SDW, interplay between magnetism and superconductivity etc. [1-6]. Hence the combination of rare earth and 3*d* transition metals have formed an excellent source of materials to study the physics of strongly correlated electron systems [7-9].

In rare earth compounds, RKKY (Ruderman-Kittel-Kasuya-Yosida) type of interaction plays an important role in magnetic ordering of 4*f* moments. Due to localization of 4*f* electrons, the mutual interaction between them should be indirect exchange interaction via conduction electrons. Such interaction through conduction electrons also give rise to Kondo effect, where the localized magnetic moments are observed to be quenched, in addition to the increase of resistance at low temperatures. On the other hand, for 3*d* transition elements, the delocalized free ions are interacting either through direct exchange (with near by ions) or superexchange (through their neighbouring non-magnetic ions) interaction.

With the discovery of pnictide superconductors, there have been renewed interest to study the interplay between magnetism, superconductivity and CDW/SDW [10-12]. Superconductivity is a phenomenon occurring in certain materials at low temperature, and is characterized by the complete disappearance of electrical resistance and appearance of diamagnetism. It originates because of the interaction between conduction electrons mediated via phonons. Charge density wave (CDW) is another ground state of the conduction electrons which is a result of a periodic modulation of the conduction electron density associated with lattice distortion. This appears to be due to the nesting of the Fermi surface at low dimensions [13, 14]. Both CDW and SC results in the opening of a

gap at the Fermi surface. However competition/coexistence of CDW and SC are common to low dimensional materials in contrast to that of the three dimensional materials [15-18].

The thesis consists of seven chapters.

Chapter 1 briefly introduces the various phenomena observed generally in correlated rare-earth systems and a detailed discussion is included. Further, it contains discussion on rare-earth magnetism along with Kondo effect and RKKY mechanism, as they help us to understand the magnetism in rare earth based alloys. A brief discussion on the exchange interactions between the rare-earth and transition atoms is also presented. Besides, some background introduction about superconductivity and the basic ideas of charge density wave ordering with specific examples of materials which show such phenomena are incorporated in chapter 1. The interplay and competition between superconductivity and charge density wave is also discussed briefly.

Chapter 2 focuses on various experimental techniques used during the course of the present work. Synthesis of both single crystal and polycrystalline sample are indispensable part of the thesis. Polycrystalline ingots are prepared by using arc melting method and single crystals have grown based on the Czochralski method. These techniques are well described in this chapter. The working principle of various instruments which are used for the characterization of the as-prepared samples are also emphasized, for example, energy-dispersive-spectroscopy (EDAX) and electron probe micro analyzer (EPMA) for confirming the stoichiometry ratio of the samples, Powder x-ray diffraction (XRD) to confirm the phase purity and crystal structure and Laue diffraction pattern for orienting single crystals along three principle crystallographic directions. In addition to that, a description of resistivity set up used for measurements is given. Various other commercial magnetometers such as Vibrating Sample Magnetometer (VSM) and Superconducting quantum interference device (SQUID) magnetometer used to measure magnetic properties of the samples are also described. The working principle of Quantum Design Physical Properties Measurement System (PPMS) and Differential Scanning Calorimeter (DSC) which are used to measure heat capacity properties of the samples are included here.

Chapter 3 describes the interplay and competition between superconductivity (SC) and charge-density-wave (CDW) ordering transition. The compound $\text{Lu}_2\text{Ir}_3\text{Si}_5$ is a member of a class of ternary transition metal silicides, which crystallizes in the three-dimensional orthorhombic $\text{U}_2\text{Co}_3\text{Si}_5$ type structure. It has a superconducting transition at 3.5 K and undergoes another phase transition below 190 K which has been shown to be a strongly coupled charge density wave ordering [19]. Similar behavior has been reported in $\text{Lu}_5\text{Ir}_4\text{Si}_{10}$, where one observes significant effect in the variation of transition temperature

of CDW/SC when pressure (chemical) is applied or the density of electrons in the Fermi surface is changed [20]. Since the main features of the structural arrangement of $\text{Lu}_2\text{Ir}_3\text{Si}_5$ are almost identical to $\text{Lu}_5\text{Ir}_4\text{Si}_{10}$, it would be important to investigate the consequence of the chemical pressure and variation of electrons in the Fermi surface in $\text{Lu}_2\text{Ir}_3\text{Si}_5$. Hence a detailed investigation has been undertaken on pseudo-ternary alloys $(\text{Lu}_{1-x}\text{Sc}_x)_2\text{Ir}_3\text{Si}_5$, $\text{Lu}_2(\text{Ir}_{1-x}\text{Rh}_x)_3\text{Si}_5$ and $\text{Lu}_2\text{Ir}_3(\text{Si}_{1-x}\text{Ge}_x)_5$ via magnetization, thermal and transport measurements. We track the evolution of the superconducting transition temperature T_{SC} and the CDW-ordering transition temperature T_{CDW} as a function of doping concentration x to present a temperature-concentration phase diagram for each of the series of compounds, displayed in Figure 0.1, Figure 0.2 and Figure 0.3. In Figure 0.1, we find that

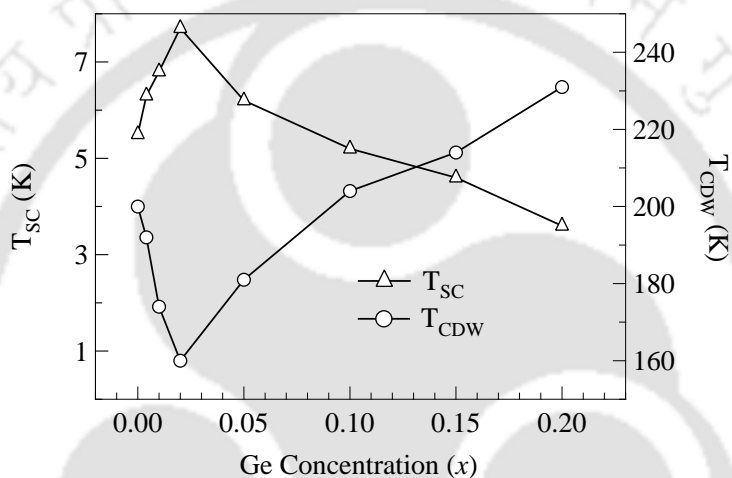


Figure 0.1: Plot of T_{CDW} and T_{SC} versus Ge concentration (x) for $\text{Lu}_2\text{Ir}_3(\text{Si}_{1-x}\text{Ge}_x)_5$ ($x = 0.00, 0.004, 0.01, 0.02, 0.05, 0.1, 0.15$ and 0.2).

as we increase x , T_{CDW} and T_{SC} show a non-monotonic behaviour in $\text{Lu}_2\text{Ir}_3(\text{Si}_{1-x}\text{Ge}_x)_5$. Here, we observed that both CDW and SC survive till 20% of Ge substitution. In $\text{Lu}_2(\text{Ir}_{1-x}\text{Rh}_x)_3\text{Si}_5$, as Rh concentration increases, T_{CDW} varies rapidly from 207 to 284 K, whereas the T_{SC} reduces gradually from 5.5 to 2.5 K, shown in Figure 0.2. In addition, the temperature-concentration phase diagram of $(\text{Lu}_{1-x}\text{Sc}_x)_2\text{Ir}_3\text{Si}_5$ is shown in Figure 0.3 noted that Sc substitution at Lu site of $\text{Lu}_2\text{Ir}_3\text{Si}_5$ displays a slight change in CDW transition temperature, without affecting the SC ordering temperature too much. Our study reveals that the CDW anomalies are broadened and smeared out, probably, by substitutional disorder effects. The heat capacity data in the vicinity of the CDW transition for all the substituted alloys have been analyzed using a model of critical fluctuations in addition to a mean-field contribution plus a smooth lattice background. The critical exponent changes appreciably with increasing disorder, which suggests that the first order

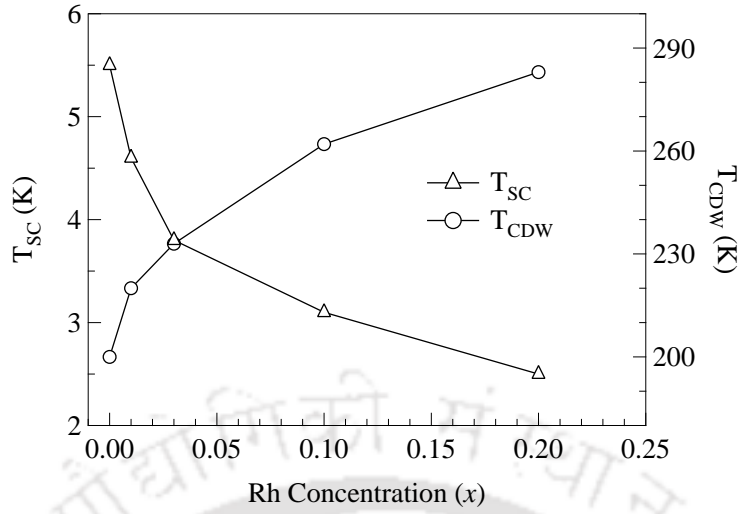


Figure 0.2: Plot of T_{CDW} and T_{SC} versus Rh concentration (x) for $\text{Lu}_2(\text{Ir}_{1-x}\text{Rh}_x)_3\text{Si}_5$ with $x = 0.00, 0.01, 0.03, 0.1, 0.2$ and 0.3 .

CDW transition in parent compound $\text{Lu}_2\text{Ir}_3\text{Si}_5$ changes to a second order transition upon doping.

Chapter 4 describes the strongly coupled first-order charge density wave transition in $\text{Lu}_2\text{Ir}_3\text{Si}_5$ single crystal. The as-grown high quality of single crystal charge density wave compound $\text{Lu}_2\text{Ir}_3\text{Si}_5$ is established to exhibit superconductivity below 3.5 K. The susceptibility and the resistivity show sharp jump at CDW transition temperature around 233 K. The compound shows a huge thermal hysteresis between cooling and warming scans across CDW transition temperature in all the measurements which is consistent with the first order phase transition. The first order nature of CDW is also ascertained by a very narrow and huge cusp (55 J/mol K) in the specific heat, in contrast to those in weakly-coupled CDW materials. A quantitative analysis for the specific heat data near the fluctuation region yields a critical exponent $\alpha \sim 2$, much larger than the predicted value $\alpha = 0.5$ in the extended mean-field theory. It gives a unit ratio of $\gamma^*/\gamma = 8.9$, which is about 6.2 times larger than the BCS weak-coupling limit value 1.43, indicating strong coupling nature of the CDW transition. In addition, anisotropic superconducting properties in $\text{Lu}_2\text{Ir}_3\text{Si}_5$ single crystal are investigated. The superconducting parameters, deduced from the anisotropic Ginzburg-Landau theory, reveal that $\text{Lu}_2\text{Ir}_3\text{Si}_5$ is a hard type-II superconductor with a large κ value. The compound is found to show quasi-one dimensional superconductivity with enhanced conduction along the c -axis and anisotropy parameter (H_{C2}^c/H_{C2}^a) of about 1.8. The low value anisotropy suggests a strong coupling between the planes unlike that of chalcogenides such as, 2H-NbSe_2 . The lower superconducting

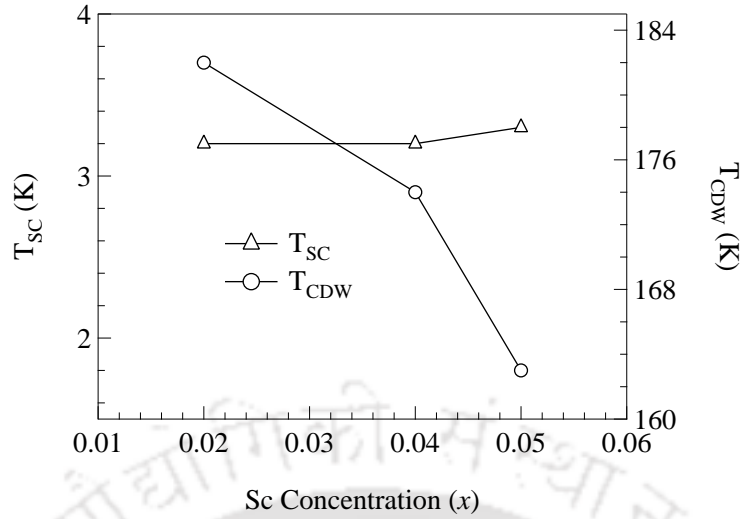


Figure 0.3: Plot of T_{CDW} and T_{SC} versus Sc concentration (x) for $(Lu_{1-x}Sc_x)_2Ir_3Si_5$ with $x = 0.02, 0.04$ and 0.05 .

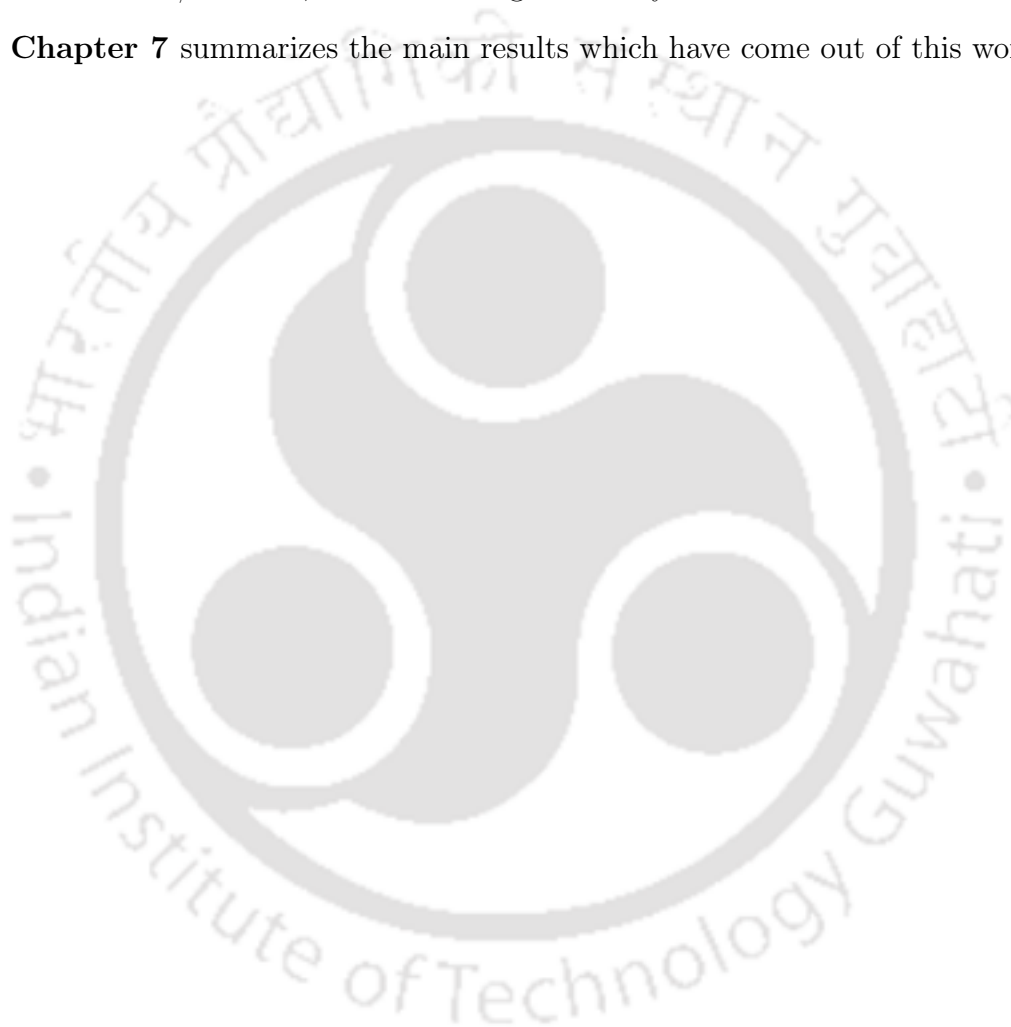
transition temperature, longer magnetic penetration depths etc. reflect subtle differences in the Fermi surface topologies, which may be controlled by the CDW transition.

Chapter 5 describes the detailed magnetic properties of polycrystalline ternary rare earth intermetallic stannide compounds $R_2Ir_3Sn_5$ by analyzing the results of crystal structure, magnetic susceptibility, isothermal magnetization, electrical resistivity and heat capacity data. The polycrystalline samples are prepared for $R = La, Ce - Nd, Gd - Tm$. The notable finding in this series is that, except for $La_2Ir_3Sn_5$, all the other compounds of $R_2Ir_3Sn_5$ ($R = Ce - Nd, Gd - Tm$) crystallize in the orthorhombic $Y_2Rh_3Sn_5$ ($Cmc2_1$) type of structures. $La_2Ir_3Sn_5$, crystallizes in the $U_2Co_3Si_5$ type orthorhombic crystal structure with the space group $Ibam$. Magnetic studies reveal that $Ce_2Ir_3Sn_5$ is a Kondo system, which undergoes an antiferromagnetic ordering at 2.9 K while no magnetic ordering was observed in $Pr_2Ir_3Sn_5$ and $Nd_2Ir_3Sn_5$ down to 1.8 K. The higher rare-earths from Gd - Tm of this series exhibit magnetic ordering below 10 K. Crystal field analysis was done on both the magnetic susceptibility and heat capacity to find the crystal field level schemes. From the detailed magnetic measurements, it is clear that the magnetic ordering temperature deviates from the expected de-Gennes scaling which indicates that the crystal field effects should also be included in the de-Gennes scaling theory to account for this deviation.

Chapter 6, describes magnetic, transport, thermal and crystallographic properties for single crystal of $Ce_2Ir_3Sn_5$. The compound crystallizes in the orthorhombic $Y_2Rh_3Sn_5$ ($Cmc2_1$) type structure. $Ce_2Ir_3Sn_5$ orders antiferromagnetically with a Néel temperature T_N of 3.6 K. Its resistivity shows a shallow minimum at around 30 K and a logarithmic

mic dependence of temperature below this temperature. These features suggest a Kondo behaviour in $\text{Ce}_2\text{Ir}_3\text{Sn}_5$. Further, the reduced value of magnetization below the ordering temperature, together with the reduced entropy at the magnetic ordering temperature and the enhanced low temperature heat capacity indicate that the Kondo effect plays a significant role in this compound. Obvious anisotropy has been observed in both resistivity and susceptibility data, reflecting orthorhombic symmetry of the crystal structure. The specific heat capacity data at low temperatures exhibit an enhanced Sommerfeld coefficient of 269 mJ/mol K^2 , thus indicating the heavy fermion nature of $\text{Ce}_2\text{Ir}_3\text{Sn}_5$.

Finally, **Chapter 7** summarizes the main results which have come out of this work.



List of Publications

Journals

1. Magnetic ordering and crystal field effects in the $RE_2Ir_3Sn_5$ (RE = La, Nd, Gd, Tm) system.
N. S. Sangeetha, A. Thamizhavel, C. V Tomy, Saurabh Basu, S. Ramakrishnan and D. Pal, Phys. Rev. B **84**, 064430 (2011).
2. Interplay of superconductivity and charge density wave ordering in pseudoternary alloy compounds: $Lu_2Ir_3(Si_{1-x}Ge_x)_5$, $Lu_2(Ir_{1-x}Rh_x)_3Si_5$ and $(Lu_{1-x}Sc_x)_2Ir_3Si_5$.
N. S. Sangeetha, A. Thamizhavel, C. V Tomy, Saurabh Basu, A. M. Awasthi, S. Ramakrishnan and D. Pal, Phys. Rev. B **86**, 024524 (2012).
3. Magnetic ordering and crystal effects in single crystal of $Ce_2Ir_3Sn_5$
N. S. Sangeetha, A. Thamizhavel, C. V Tomy, Saurabh Basu, S. Ramakrishnan and D. Pal (under process)
4. Interplay of Charge density wave and SC in single crystal of $Lu_2Ir_3Si_5$
N. S. Sangeetha, A. Thamizhavel, C. V Tomy, Saurabh Basu, A. M. Awasthi, S. Ramakrishnan and D. Pal (under process)

Conferences

1. Interplay of superconductivity and charge density wave ordering in pseudoternary alloy system: $Lu_2Ir_3(Si_{1-x}Ge_x)_5$.
N. S. Sangeetha, A. Thamizhavel, Saurabh Basu, S. Ramakrishnan and D. Pal, M2S conference, Washington, D.C, July 29-August 3, 2012 (abstract accepted).
2. Transport and Magnetic Properties of $R_2Ir_3Sn_5$ (R = La, Ce, Pr, and Nd) System.
N. S. Sangeetha, A. Thamizhavel, Saurabh Basu, S. Ramakrishnan and D. Pal, AIP Conf.Proc. **1349**, 1215-1216 (2011).

3. Transport and Magnetic Properties of $\text{Lu}_2(\text{Ir}_{1-x}\text{Rh}_x)_3\text{Si}_5$.

N. S. Sangeetha, Saurabh Basu, A. Thamizhavel, A. K. Grover, S. Ramakrishnan and D. Pal, DAE SSPS 54, I39 (2009)



Chapter 1

Introduction

Magnetism and superconductivity are two distinct many body phenomena that have attracted researchers for decades. Similarly, charge/spin density wave (CDW/SDW) has also recently drawn ample attention due to the strong electron-electron correlations present therein and of course its close analogy to superconductivity. Hence, the question about the interplay, competition and coexistence between these different ground state phenomena center around the behaviour of the correlated electron systems. However, it is now well established that the coexistence of multiple ground states are common in certain rare earth based alloy superconductors, manganites, Ruthenates and high T_C cuprates. Many of these studies have revealed the emergence of several new concepts such as competition between several ordered ground states, the presence of quantum critical points, importance of charge ordering, topologically frustrated magnetic systems, mixed valent Kondo systems and so on. More recently, the discovery of iron based (pnictide) superconductors have renewed interest to explore the interplay of superconductivity (SC), magnetic ordering and charge/spin density wave. These materials demonstrated SDW in its pure form, however it was found that SDW can be suppressed by external/chemical pressure which led to appearance of superconductivity, with the transition temperature over 50 K [21]. Moreover, while there are enough experimental measurements which support both CDW/SDW and SC scenario, it is still an open problem whether CDW/SDW boosts or competes with superconductivity. Understanding that these novel quantum phenomena are crucial to the progress of fundamental physics, it is important to study different intermetallic compounds with different crystal structures. In the specific context of rare earth based intermetallic compounds, the magnetic moments of localized f electrons interact with the conduction electrons and this s - f interaction results in a variety of fascinating physical phenomena and unusual ground states such as magnetic ordering of the localized rare-earth moments, Kondo behavior, large positive magnetoresistance, along

with valence fluctuation, superconductivity, charge/spin density wave (CDW/SDW), the coexistence of superconductivity and charge density wave, the interplay of magnetism and superconductivity etc. [1, 2, 3].

The following section will give crisp introduction to magnetism in the rare earth based systems and the magnetic exchange mechanism, besides providing a elementary background information about superconductivity and charge density wave ordering.

1.1 Rare Earth Magnetism

1.1.1 The Rare Earth Metals (RE)

The “Rare Earth” elements are commonly called the lanthanides (Lanthanum La-57 to Lutetium Lu-71), which are the members of Group III.A of the periodic table. The electronic configuration of the lanthanides is $[Xe]4f^n5d^16s^2$, where the $4f$ -shell is successively filled up by increasing the atomic number (from La($4f^0$) to Lu($4f^{14}$)) [23]. The f -shell in the atom is pushed deep into the interior of the completely filled $5s$ and $5p$ shells because of the strong centrifugal potential [24]. Hence the rare-earth ions possess strongly localized magnetic moments, as indicated by the f -shell electrons. A schematic diagram of rare-earth orbitals and the radial distribution of the atomic orbital of the rare earth ion is shown in Figure 1.1. One can notice that the tail of the wave function, see Figure 1.1(b), spreads beyond the closed $5s$ and $5p$ shell and this extension is highly influenced by potential energy and the distance between the lanthanide atoms. This results in hybridization of the $4f$ electrons with the conduction electrons. Because of their “deep-lying” $4f$ electrons, the f -shell is shielded by the conduction electrons from the crystalline electric field (CEF) of the neighbouring ions. The orbital moment is therefore not quenched¹ and the total magnetic moment has both orbital and spin components. The shielding of one $4f$ electron by another is imperfect due to the shapes of the orbitals resulting in an anisotropy of the f subshell and this plays an important role in compounds comprising of rare earth elements. Thus with each atomic number increment, the effective nuclear charge experienced by each $4f$ electron increases, causing a reduction in size of the entire $4f^n$ shell which is known as Lanthanide contraction, that plays an important role indicating the ground state properties.

¹In crystals, the electron orbits are essentially coupled to the lattice which prevents the orbital magnetic moments from turning into field direction by applying an external magnetic field. In this case, it says that the orbital moments are quenched ($L=0$).

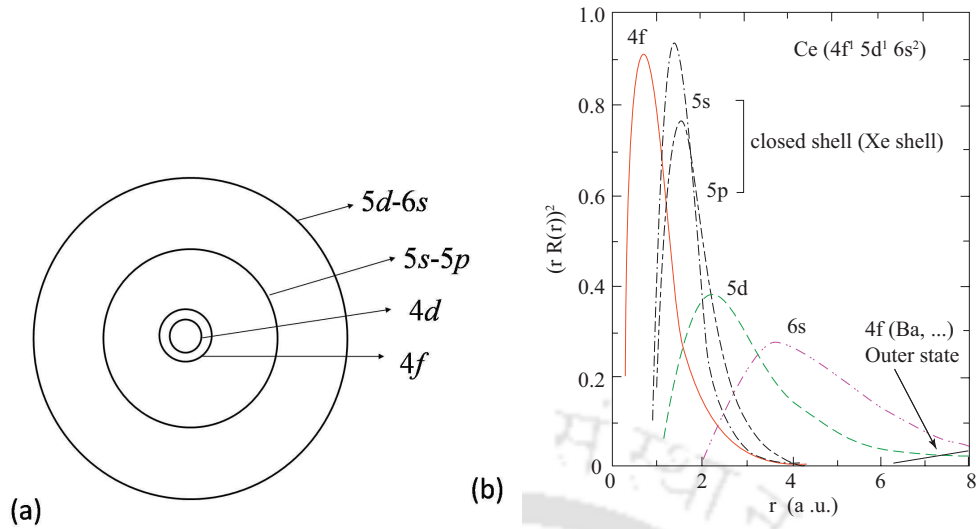


Figure 1.1: (a) A schematic representation of the atomic orbitals of a rare-earth atom with the circles indicating the approximate positions of the charge density maxima. The $5s$ - $5p$ orbit illustrates the size of the Xenon core. (b) Radial distribution of different atomic orbitals in the Ce atom [courtesy [25]].

Due to the weak crystal field and the absence of orbital quenching in rare earth based compounds, the spin-orbit coupling is strong. According to the Russell-Saunders coupling scheme the values of total angular momentum $\mathbf{J} = \mathbf{L} \mp \mathbf{S}$, depending on whether the $4f$ shell is less (-ve) or more (+ve) than half filled. The values of the total orbital momentum $\mathbf{L} = \sum_i \mathbf{l}_i$ and the total spin momentum $\mathbf{S} = \sum_i \mathbf{s}_i$ are given by Hund's rule. For most accessible temperatures, the lowest \mathbf{J} multiplet determines the magnetic properties of the rare earth compounds as the energetic distance of the lowest lying multiplet to the first excited multiplet is large (~ 1000 K).

The effective magnetic moment magnitude for free ions in units of Bohr magnetons (μ_B) is given by $\mu_{eff} = g_J \sqrt{J(J+1)}$. For the rare earth trivalent ions (R^{3+}), the experimental values of this quantity agree reasonably well with the predictions based on the Hund's rules. However, a discrepancy occurs for some of the rare-earths like Ce, Sm, Eu and Yb and this is due to low-lying excited state with different a \mathbf{J} from the ground state. But for Ce^{4+} , Eu^{2+} and Yb^{2+} , the most energetically favorable ground state either has a half filled or completely filled (completely empty) $4f$ shell.

In the case of heavy rare earth metals (Gd-Tm), the contribution of conduction electrons is more effective, which results in a reduced magnetic moment compared to the one predicted by Hund's rules. In the paramagnetic regime, the magnetic susceptibility

of the rare earth metals can be well estimated by a Curie-Weiss law given as,

$$\chi = N_A \frac{g_J^2 \mu_B^2 J(J+1)}{3k_B(T - \theta_P)} \quad (1.1)$$

Here, N_A is the Avagadro's number, μ_B is the Bohr magneton, k_B is the Boltzmann constant, T is the temperature, and θ_P is the Curie temperature. The Landé factor g_J in the case of Russel-Saunders coupling is, $g_J = \frac{3}{2} + \frac{S(S+1) - L(L+1)}{2J(J+1)}$. The non-magnetic rare earths Y, Sc, La and Lu have frequently been used as hosts for dilute alloy measurements.

1.1.2 The transition Metals (TM)

The TM are elements with partially filled $3d$, $4d$ and $5d$ bands. For $3d$ elements, the electrons in the outermost shell are delocalized to the extent that they are capable of interacting with other such electrons and their surroundings. This results in a non-negligible electric field which is determined by the symmetry of the crystalline environment and thus crystal effects become important in transition metals. Because of strong crystal field, the orbitals may be "quenched" ($L = 0$) in this system. Hence the ground state is $L = 0$, $J = S$. For the case of $3d$ ions, the effective moment can be written as, $\mu_{eff} = g_J \sqrt{S(S+1)}$. This produces much better agreement with the experimental data for free ions, since the spin-orbit coupling can effectively be ignored in such system, which is against the Hund's third rule. The situation in higher transition metal ions (the $4d$ and $5d$ series) is less clear because the heavier ions have a larger spin-orbit coupling strength and the effects of the crystal field and the spin-orbit interaction can be comparable. Therefore the magnetic moment due to electron spin is important particularly in $3d$ metals as alloying with other components can have a marked effect on the magnetic behaviour.

1.1.3 Magnetism in RE-TM alloys

There are several factors that have generated ample interest in RE-TM alloys. The first concerns with the magnetic ordering and large magnetic moments of rare earth elements at low temperatures, while the second is relevant to the large difference in atomic radii between RE and TM ($3d$ -metal) atoms which leads to the formation of several intermetallic compounds with various crystal structures. Thirdly, many of these intermetallic compounds exhibit magnetic ordering by virtue of the coupling of the rare earth magnetic moments with the $3d$ moments of the transition elements.

In the $3d$ magnetic elements, large $3d$ exchange interactions stabilize magnetic ordering well above room temperature, but because the orbital moments are “quenched”, the magnetic anisotropy is generally very small, thus limiting the coercivity of the $3d$ elements. The rare earths on the contrary exhibit large orbital moments, but the $4f$ magnetic interactions are much smaller than those of the $3d$ electrons and the ordered magnetic state is attained only below room temperature. In RE - TM alloys however $4f$ and $3d$ electron interactions can occur, so that the $3d$ interactions stabilize the magnetic ordering to temperatures above the room temperature and the $4f$ anisotropy remains strong at room temperature. Thus, an ingenious was of combining of the magnetic and crystal characteristics, in some RE - TM alloys, can lead to a exotic magnetic ground states.

Before the magnetic properties of Rare earth intermetallic compounds are discussed, it is essential to point out the crucial difference between the rare earth and the transition metals. In the transition metals, the outermost $3d$ electrons are delocalized on single ion site. Their wavefunctions reach far enough to overlap between neighbouring (d electrons) wave functions. The magnetic ordering in d -systems is established through the direct Coulomb interaction between the spins of these overlapping shells. In contrast to this system, $4f$ -shells of rare earth ions are strongly localized and are well screened by completely filled $5s$ and $5p$ shell. In the case of rare earth metals, direct overlap between the neighbouring f -shells is not possible due to the small spatial extent of $4f$ -orbital (≈ 0.3) compared to the inter-ionic distance ($\approx 3 - 5$). Hence, the rare earth moments interact mainly by an (Heisenberg type exchange interaction) indirect exchange between the localized spins (\mathbf{S}) of $4f$ shells mediated by conduction electrons (\mathbf{s}), the Hamiltonian can be expressed as

$$H = -J_{RKKY} \mathbf{s} \cdot \mathbf{S} \quad (1.2)$$

and this is known as Rudermann-Kittle-Kasuya-Yosida (RKKY) interaction [26, 27, 28]. The interaction is characterized by a coupling coefficient $J_{RKKY}(R) \propto \frac{\cos(2k_F R)}{(2k_F R)^3}$, where k_F is the Fermi wave vector. Hence, depending on the distance between a pair of ions, the RKKY exchange coefficient, $J_{RKKY}(R)$ can lead to either positive (ferromagnetic) or negative (antiferromagnetic) interaction.

The RKKY interaction along with CEF effects on rare earth intermetallic compounds are expected to show a variety of anomalous behaviour in their magnetic properties. This anomalous behaviour can be attributed to the largeness of the c - f hybridization

with itinerant conduction electrons which gives a certain delocalized character to the $4f$ moments. This hybridization between d and f orbitals are taken into account for a wide variety of unusual phenomena in RE intermetallic compounds, like the Kondo effect, valence fluctuation, reduced moment magnetism, Heavy Fermion behavior, the re-entrant superconductivity etc.

If the hybridization is strong, the $4f$ electron can make spontaneous fluctuations between the $4f$ shell and the conduction band giving rise to “valence fluctuations” (also called intermediate or mixed valence). This effect is predominantly observed in the middle or end of the RE series, since they have a tendency for attaining half-filled or completely filled shell configuration. In case of Ce, Eu and Yb based compounds, it can be seen that the RE ion has a heterogeneous mixed valence state [30, 31, 32].

1.1.4 The Kondo effect

The effect was first explained theoretically by Jun Kondo in 1964 [33]. It is a many-electron effect which describes the scattering of conduction electrons in a metal due to magnetic impurities. Alternatively, Kondo effect is due to the interaction between a single magnetic atom and the many electrons in an otherwise non-magnetic metal. Such an impurity, typically has an intrinsic angular momentum or spin that interacts with the electrons. For example, being a quantum particle, the impurity spin can tunnel out of the impurity site to a classically forbidden region outside the impurity and then can be replaced by an electron from the metal. This can effectively flip the spin of the impurity spin. Many such events combine to produce the Kondo effect, which leads to the appearance of an extra resonance at the Fermi energy. This resonance is very effective in explaining the scattering of electrons near the Fermi level. Since the transport properties are determined by electron near the Fermi level, this extra resonance results in the increase in resistivity. The resistivity minimum observed in a Kondo system at low temperature can be explained by above mentioned approach. The temperature dependence of the resistivity at low temperature including the Kondo effect is written as

$$\rho(T) = \rho_0 + aT^2 + c_m \ln(T/T_F) + bT^5 \quad (1.3)$$

where ρ_0 is the residual resistance, aT^2 shows the contribution from the Fermi liquid character and the term aT^5 comes from the lattice vibrations, while a , c_m and b are constants. Kondo derived the logarithmic temperature dependence $\ln\left(\frac{T}{T_F}\right)$, of resistivity as in the third term which gives good agreement with the observed features of the scattering-related

resistivity minimum at low temperature. This is shown schematically in Figure 1.2(a). However, it can be seen that Kondo's expression for the resistivity diverges below a characteristic temperature T_K , which is known as Kondo temperature.

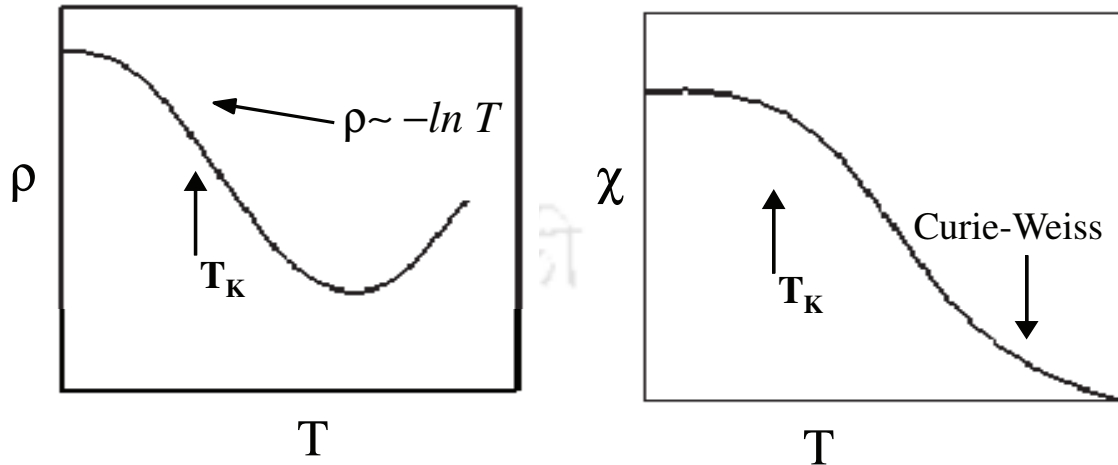


Figure 1.2: The qualitative temperature variation of the resistivity and susceptibility of a single ion Kondo system.

Kondo showed that mobile electrons in a metal like to align their spins opposite to that of a nearby magnetic impurity. At low temperatures, an electron moving past an impurity would then tend to flip its spin and be simultaneously deflected from its path, thereby qualitatively explaining the observed resistance rise. In addition to the logarithmic upturn in the resistivity, the susceptibility below T_K has a weak temperature dependence. The behaviour of the resistivity and susceptibility of a single ion Kondo system as a function of temperature is shown in Figure 1.2.

1.2 Superconductivity

One of the hallmarks of the 20th century physics was the discovery of superconductivity. The phenomena was first discovered by Kamerlingh Onnes in 1911 at the University of Leiden. It is characterized by zero electrical resistance and perfect diamagnetism (Meissner effect). External magnetic fields decide the superconducting properties of materials. Thus according to the different behaviour exhibited in presence of a magnetic field, superconductors are classified into two groups, viz., Type-I and Type-II superconductors. Type-I superconductors are those which on application of an external magnetic field exhibit complete expulsion of the field till a thermodynamic critical field H_C . These

superconductors perfectly obey Meissner effect. Type-II superconductors exclude the field completely up to the field H_{C_1} . Above H_{C_1} , the field is partially excluded, but the specimen remains electrically superconducting. At a much higher field, H_{C_2} , the flux penetrates completely and the superconductivity vanishes, where it becomes a normal conductor. Besides the Meissner state, type II superconductors have another state between the lower critical field (H_{C_1}) and upper critical magnetic field (H_{C_2}) which is known as a vortex state or the mixed state, where the magnetic flux penetrates into the superconductors in the form of vortices with flux quantum, $\varphi_0 = h/2e$. The vortices interact with each other and arrange themselves in a regular structure known as a vortex lattice (Abrikosov vortex lattice). The core of a vortex is in the normal state and it has a radius of the order ξ . Alloys and high T_C superconductors are examples of Type-II superconductors. A Type-I and a Type-II superconductor is distinguished based on a dimensionless ratio, $\kappa = \lambda/\xi$. If the coherence length ξ is longer than the penetration depth λ , the superconductor will be Type-I with $\kappa = \lambda/\xi < 1/\sqrt{2}$. But when ξ smaller than λ the superconductor will be Type-II and $\kappa > 1/\sqrt{2}$ [34].

A number of the elements in the periodic table become superconducting at low temperatures. Among the elements, Niobium (Nb) has the highest critical temperature T_C of 9.2 K. In addition, superconductivity has been extensively studied in a wide range of alloys, intermetallic and ionic compounds with all of them exhibiting critical temperature below 20 K, and these compounds are classified as conventional superconductor. Interestingly, the so-called A15 compounds such as Nb_3Sn , Nb_3Ga and Nb_3Ge which have registered the highest transition temperatures, viz. $T_C = 23$ K. Subsequently, the compounds $\text{La}_{2-x}\text{Ba}_x\text{CuO}_4$ and $\text{YBa}_2\text{Cu}_3\text{O}_7$ were discovered which yield a $T_C = 38$ K and 92 K respectively, ushering in the era of “high temperature superconductivity”.

In addition to high temperature superconductors, there also many other interesting superconducting materials. Some of these have exotic properties which are still not understood and under active investigation. These include oxide-based superconducting materials, organic superconductors (generally referred to as $\kappa\text{-(ET)}_2\text{X}$), C_{60} based fullerene superconductors, and heavy fermion superconductors (CeCu_2Si_2 , UBe_{13} , etc.). Other superconductors have surprising properties, such as coexistence of magnetism and superconductivity, coexistence of CDW/SDW and SC or evidence of other exotic “unconventional” superconducting phases. As an example of the latter, MgB_2 is a two band superconductor which gives evidence for two gap nature of superconductivity. The NbSe_2 is also believed to have two distinct gaps which are structurally similar to MgB_2 . Another aspect to consider is stacking sequence of 2H-NbSe_2 which makes the material closer to layered

superconductors. An additional feature of NbSe₂ is charge density wave state observed below 33 K.

Besides, one of the most important discoveries for the past few years is the invention of new family of high T_C superconductors known as “pnictide” superconductors. Like the high- T_C copper-oxides, the exact mechanism that causes superconductivity in these materials is a mystery. Other important achievement in this area of research is the experimental observation of topological superconductor in 3D bulk materials, Cu-intercalated topological insulator Bi₂Se₃ (Cu_xBi₂Se₃), where the material becomes a superconductor in the bulk of the material, but still becomes a normal metal on the surface [35].

On the other hand, the studies on ternary compounds [36] unraveled new phenomena such as the coexistence of SC and AFM, field induced superconductivity etc. The SC and magnetism are individually observed in many systems [37, 38, 39], however, the reentrant SC and the coexistence of AFM and SC have been observed only in a very few systems (e.g. some ternary superconductors, heavy fermion superconductors and high temperature oxide superconductors). A few of the most studied compounds [40] are the Chevrel phases RMo₆(S,Se)₈ and ternary borides RRh₄B₄ and in which almost all of the compounds show AFM and superconductivity. There are only a few well-established examples of ferromagnetic superconductors the best known and most studied are HoMo₆S₈ and ErRh₄B₄ [41, 42]. Continuing further investigations in the case of the ternary rear-earth transition metal silicides, it has been discovered that R₂Fe₃Si₅ system forms in a tetragonal structure (space group $P4/mnc$) with no transition metal clusters. These compounds display a variety of unusual properties including several examples of occurrence of SC in the absence of magnetic ordering (R = Y, La, Sc) [7, 43]. Till today a large number of pseudo-ternary systems have been synthesized and some of them have been studied in great details but still the origin of superconductivity in most compounds is not established.

1.3 Charge Density Wave

Density waves are broken symmetry ground states of metals which arise as a consequence of electron-electron or electron-phonon interaction. This phenomenon of electron instabilities at low temperatures is coupled to an underlying lattice in a one-dimensional metal, as was first point out by Peierls (1955), called as Peierls instability [13]. He showed that the ground state for such a coupled electron-phonon system are characterized by a periodic modulation of the conduction electron density associated with the modulation

of the lattice atomic positions. The periodically varying lattice distortion leads in turn to a single particle energy gap at the Fermi level, turning the material into an insulator. This is the so-called Peierls transition. If we take into account the wave nature of the electrons, the electronic charge modulates with respect to a underlying distorted lattice. This smooth periodic variation of the charges is termed as charge-density wave (CDW).

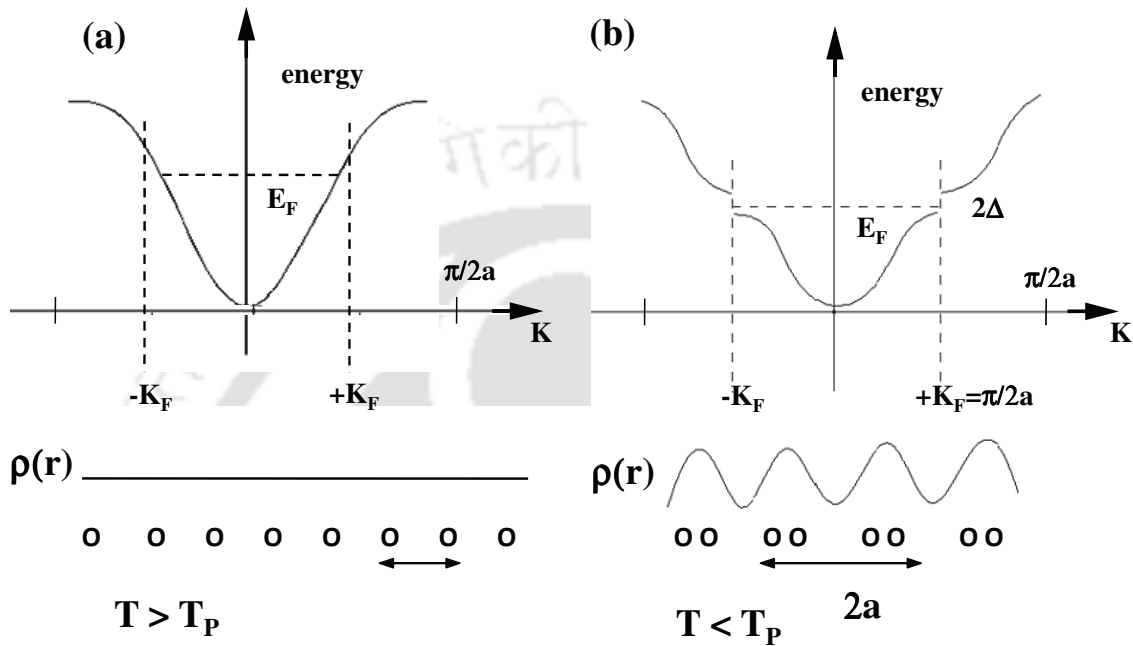


Figure 1.3: Peierls transition in a one-dimensional metal with a half filled band is demonstrated, (a) Energy dispersion of undistorted metal shown within the first Brillouin zone, E_F is Fermi level, k_F is Fermi wave vector, a is lattice constant, T_P Peierls transition temperature and the same for (b) Peierls insulator with Δ representing half of the gap that opens at the Fermi level [14].

This situation is shown schematically in Figure 1.3. In a metal, the electron density, $\rho(r)$ is highly uniform in the absence of electron-electron and electron-phonon (e-p) interaction. The equilibrium positions of the ions form a perfectly periodic lattice with lattice constant ' a ' and the electron states are filled up to the Fermi level E_F , as shown in Figure 1.3(a). In the presence of e-p interaction, Peierls point out that since the lattice no longer remains perfectly rigid and since the motion of ions affect the electron states, it is energetically favourable for the lattice to distort periodically, with a wavelength, λ given by, $2\pi/\lambda = 2k_F$. The effect of a lattice distortion of wave vector $2k_F$ leads to opening of a gap, 2Δ , in the energy spectrum at $\pm k_F$, which lowers the energy of all the occupied states as shown in Figure 1.3(b). The doubling of unit cell (superstructure) will

reduce the Brillouin zone into half. This alternating deformation of electron density is called charge density wave. The spatially dependent charge density modulation can be described as $\rho(r) = \rho_0 + \rho \cos(2k_F r + \phi)$ where ρ_0 is the electron density in the absence of electron-phonon interaction and ϕ is phase of the CDW.

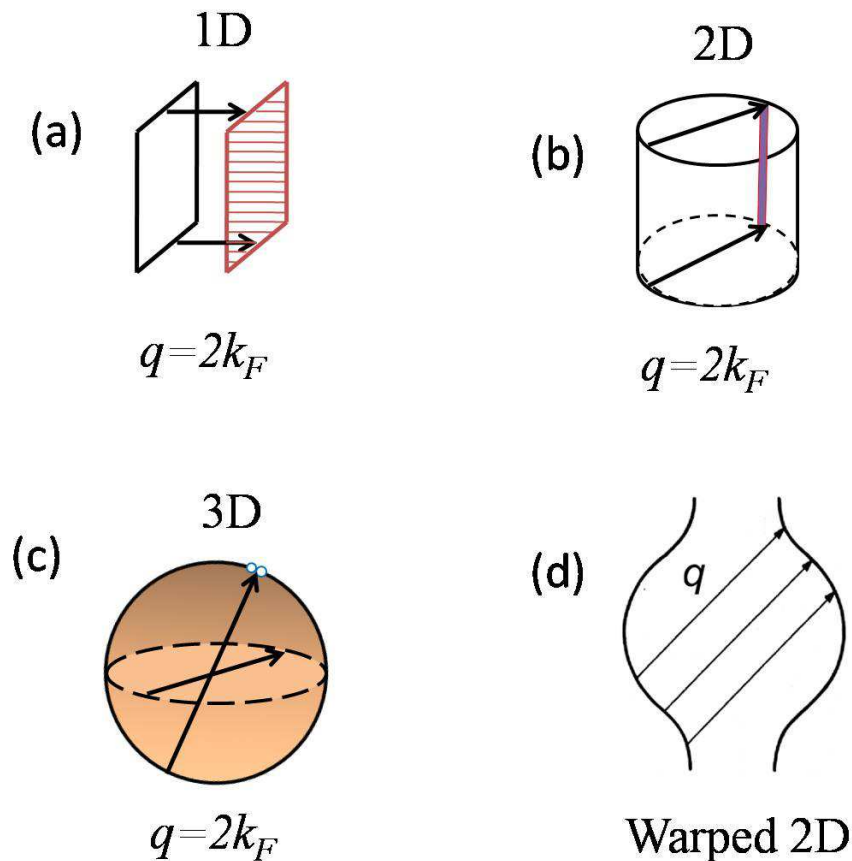


Figure 1.4: Fermi surface nesting of electron systems of (a) 1D, (b) 2D, (c) 3D and (d) warped 1D FS. The arrows indicate pairs of states, one full and one empty, differing by the vector $q=2k_F$ [courtesy [14]].

The charge density wave is an example of a cooperative state in which both the ionic lattice and the electron gas develop a distortion to lower the total (electronic+elastic) free energy of the sample. CDW is theoretically predicted to occur only when the transverse distortion exhibits in low dimensional materials having strongly anisotropic electronic structure. This is in particular importance in (quasi) low dimensional materials since the sections of Fermi surfaces (FS) are parallel to each other and thus they provide an optimal condition for nesting to induce the electron energy instability. 3D CDW order cannot produce the energy gap at all points on the Fermi surface. The formation of the

density wave is related to the nesting of the FS. The Fermi nesting structures for 1D, 2D and 3D CDW are shown in Figure 1.4.

Only for the one dimensional case, the nesting with respect to the translation $q=2k_F$ is perfect, that is ideal nesting of the entire regions of FS occurs (Figure 1.4(a)). In contrast, the 2D or 3D free electron gas do not have such ideal nesting vectors (Figure 1.4(b) and (c)). The warped FS depicted in Figure 1.4(d) shows how the FS nesting can deviate from the ideal nesting, as the topology of the FS changes. The arrows indicate perfect nesting for small dispersion in one direction. With increased dispersion, perfect nesting is no longer possible. If the nesting wave vector q turns out to be π/a where 'a' is the spacing between atoms, then the charge-density wave is said to be commensurate with the lattice. On the other hand, it is much more usual viz the nesting wave vector $q=2k_F$, not to be a simple multiple of π/a so that the charge-density wave is incommensurate.

In conclusion, the CDW is a ground state with spontaneously broken translational symmetry and is accompanied by development of a periodic modulation of the conduction electron density associated with lattice distortion. This causes a gap to open up at the Fermi level. However, this is not the whole story. CDW conductors show strikingly non-linear and anisotropic electrical properties, gigantic dielectric constants (several million times that of semiconductor, which allows them to store enormous amounts of charge. Hence their potential use as capacitors, tunable capacitor), unusual elastic properties and unusual dynamics make investigation of these materials extremely interesting. For these reasons, CDW materials are among the most remarkable electrically conducting materials ever discovered and have been the focus of intense research in the past few decades [44].

1.3.1 Charge density wave Materials and Experiments

The CDW transitions are readily observed in the materials which have chain or layered structures and transition is a second order one. This brings out the fact that low dimensional materials allow possibility of nesting of Fermi surface, as predicted theoretically. There are large number of organic and inorganic materials having linear chains, show a transition to a CDW phase has been discovered extensively. Such materials include $(\text{TMTSF})_2\text{PF}_6$ (Bechgaard salt), NbSe_3 , $\text{K}_{0.3}\text{MoO}_3$, $(\text{TaSe}_4)_2\text{I}$ and KCP (Krogmann's salt) or $\text{K}_2\text{Pt}(\text{CN})_4\text{Br}_{0.3}\cdot 3.2\text{H}_2\text{O}$ etc., which have a chain structure [44, 45].

For example, transition Metalchalcogenides (MX_3 , MX_2 and $(\text{MX}_4)_n\text{Y}$) form a variety of linear chain compounds that host CDW transition, where $\text{M}=\text{Nb}$ or Ta (group IV or V transition metals), $\text{X}=\text{S}$ or Se chalcogen atoms and $\text{Y}=\text{I}$, Br or Cl halogen atoms.

The first inorganic linear-chain material in which CDW transition was found is NbSe_3 , the crystal structure of which is shown in Figure 1.5. The crystal symmetry of NbSe_3 was

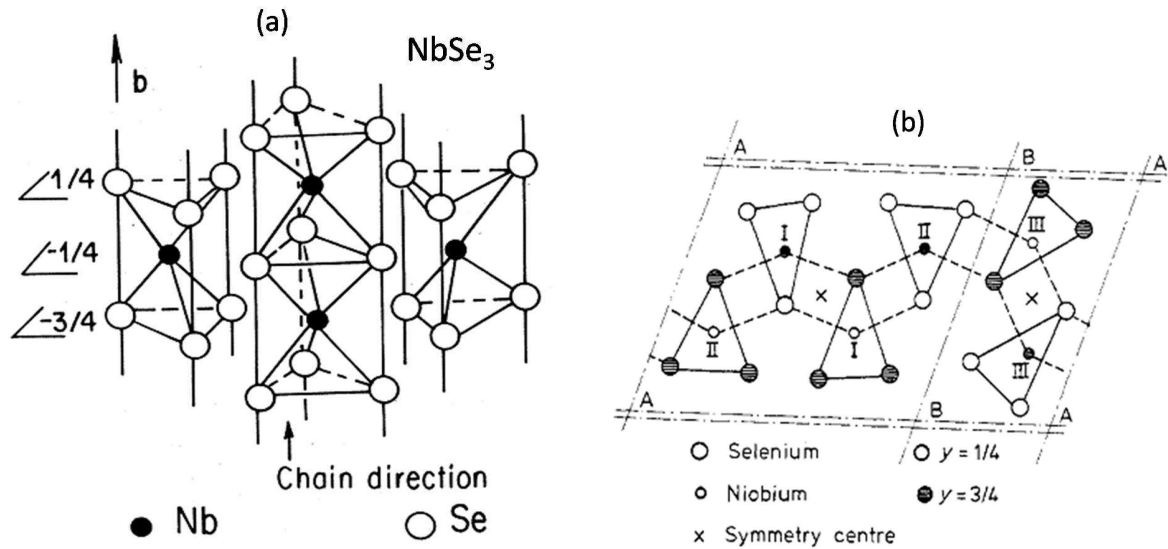


Figure 1.5: The schematic chain structure of the NbSe_3 compounds. (a) The stacking of the prisms along the b -axis in the NbSe_3 structure (b) A projection of the NbSe_3 structure perpendicular to the b -axis [courtesy [46]].

monoclinic and that the structure consists of infinite chains of Se trigonal prisms stacked on top of each other by sharing the triangular faces, as shown in Figure 1.5(a). The Nb atoms are located approximately at the centre of the prisms. The chains were found to be parallel to the b -axis. Figure 1.5(b) shows a projection of the structure perpendicular to the b -axis. The chain of Se trigonal prisms are linked together with Nb-Se bonds in the c direction so as to form infinite slabs parallel to bc plane, resulting in NbSe_3 as a true bidimensional material. These slabs are two trigonal prisms thick and they are linked together by weak Se-Se bonds. Inside the slab, there exist two types of units, which can be grouped as a set of four chain and a set of two chain. Each chain is displaced and rotated with respect to the adjacent one by $\frac{b}{2}$ and approximately 180° respectively. The two transitions taking place in NbSe_3 along b -axis are related to the four chain and two chain units, would strongly support the 1D character of NbSe_3 [46].

Compared to the one dimensional materials, CDW states are also observed in quasi 2D materials: RTe_n and R_2Te_n , where R is a rare earth element [47]. These layered compounds can be described in terms of nominally tetragonal structure based on alternating layers of square-planar Te sheets and a corrugated RTe slab, as shown in Figure 1.6. This square Te planar layers possibly tune the properties of the CDW states. The material

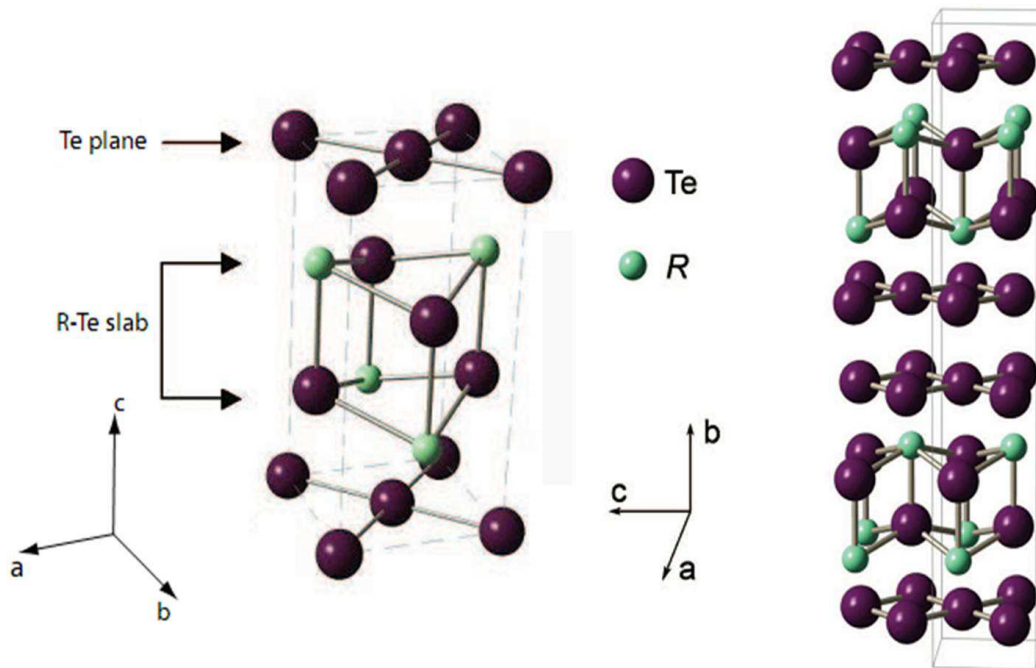


Figure 1.6: The crystal structure of $R\text{Te}_n$. The axes are shown for convenience [courtesy [47]].

indicates a strongly anisotropic two dimensional Fermi surface.

But recently the 2-3-5 ($R_2T_3X_5$) as well as the 5-4-10 ($R_5T_4X_{10}$) series compounds, which are considered to have a 3D structure, have provided evidence of CDW ordering, accompanied by a first order transition. The compound $\text{Lu}_5\text{Ir}_4\text{Si}_{10}$ where the SC and CDW coexist with that of the conventional low dimensional CDW systems like NbSe_2 and NbSe_3 . $\text{Lu}_5\text{Ir}_4\text{Si}_{10}$ adopts the tetragonal $\text{Sc}_5\text{Co}_4\text{Si}_{10}$ - type structure, as shown in Figure 1.7. Here, Ir and Si atoms form planar rings, which are stacked parallel to the basal planes, are connected along c -axis via Ir-Si-Ir zigzag chains. The Lu atoms form a quasi one- dimensional zigzag chain along c -axis which are well separated from Ir-Si ring. The distance between adjacent Lu-Lu and Ir-Ir atoms are large, whereas Ir-Si and Si-Si distances are small, indicating strong covalent interactions. The chain like structure of Lu atoms along the c -axis may not only form a quasi-one-dimensional electronic band but also achieve a CDW ground state [48].

These materials undergo a metal-to-insulator (or metal-to-semimetal) transition at temperatures below the room temperature, as evidenced by a wide range of transport, magnetic, and specific-heat studies. Furthermore, detail structural measurements, like x-ray and neutron diffraction studies, together with measurements of local properties (like

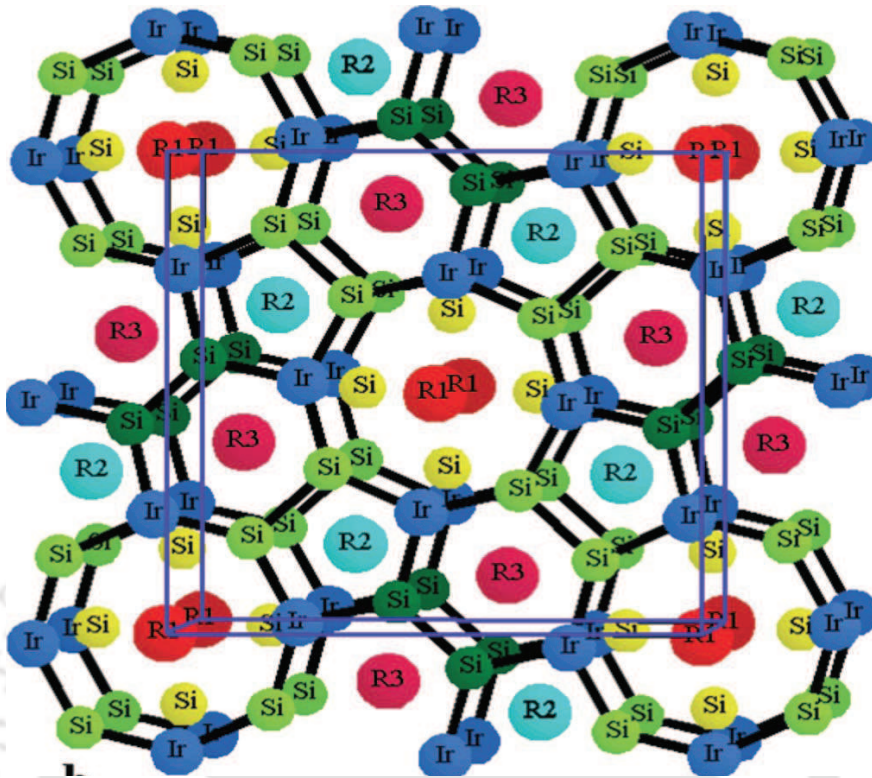


Figure 1.7: The crystal structure of $\text{Lu}_5\text{Ir}_4\text{Si}_{10}$ [courtesy [48]].

nuclear magnetic resonance for example) lead to the examination of the structural changes which accompany the phase transitions.

As an example, Figure 1.8 displays evidence of a CDW transition in NbSe_3 as observed in different measurements. The temperature dependence of dc resistivity along the b -axis of NbSe_3 is shown in Figure 1.8(a). It shows a sharp increase in the resistivity at temperatures, $T_{CDW}^1 = 149$ K and $T_{CDW}^2 = 59$ K, where a metal to a semimetal transition can be observed, unlike a metal to an insulator transition as predicted by Peierls. This indicates partial destruction of the Fermi surface at these temperatures, which is confirmed by the Hall effect and the Magnetoresistance studies. Figure 1.8(b) shows the susceptibility across the CDW transition which decreases below T_{CDW} and this is related to the opening up of a gap (or FS) across the CDW transition. Figure 1.8(c) depicts the heat capacity of the compound as a function of temperature. The well defined anomalies at $T_{CDW}^1 = 149$ K and $T_{CDW}^2 = 59$ K identify the CDW transition. The peaks which are observed at the transition temperatures are significantly large and the data reveal their broadness, instead of a sharp jump at T_{CDW} , hence indicating a second-order nature of the transition. Further, the electron and x-ray diffraction studies provide direct

evidence for such distortions by demonstrating that both CDW states are associated with the development of incommensurate lattice distortions along the chain direction.

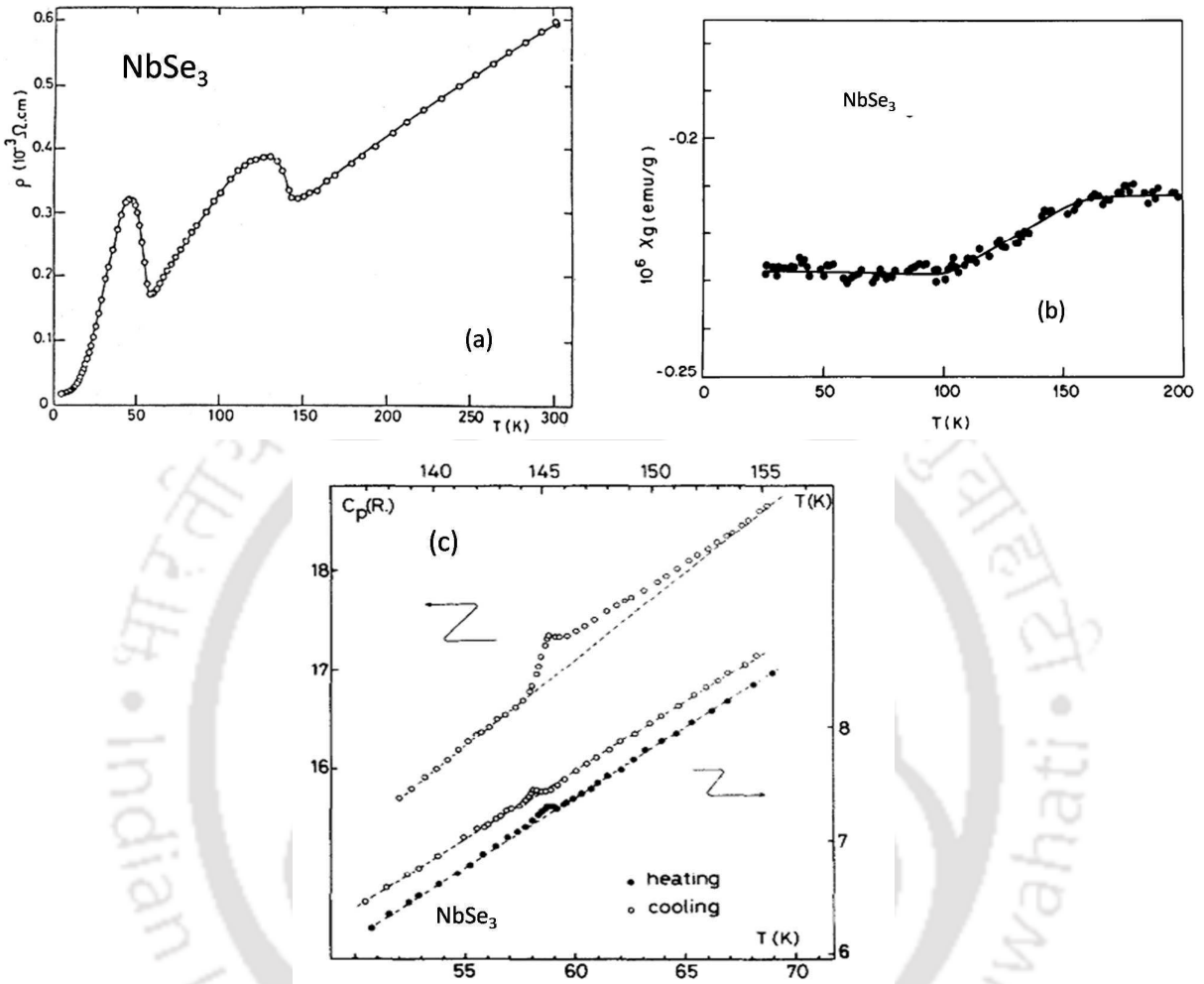


Figure 1.8: Signatures of a CDW transition is demonstrated (a) The temperature dependence of the dc resistivity of NbSe₃ [46]. Note the increase of ρ_{dc} at $T_{CDW}^1 = 149$ K and $T_{CDW}^2 = 59$ K. (b) The magnetic susceptibility of NbSe₃ shows a decrease below 150 K which are associated with the upper CDW transition [49]. (c) The specific heat of NbSe₃ as a function of temperature: top scale for T_{CDW}^1 ; bottom scale for T_{CDW}^2 [courtesy [50]].

1.3.2 Coexistence of Superconductivity and the Charge Density Wave Ordering

Superconductivity and the CDW states are two very different cooperative electronic phenomena, and yet both occur due to Fermi surface instabilities and electron-phonon

coupling. A number of CDW-bearing materials are also superconducting, and the idea that superconductivity and CDW states are competing electronic states at low temperatures is one of the fundamental concepts of condensed matter physics [51, 52, 53, 54].

There is an extensive experimental evidence for the coexistence of SC and CDW order. The ever increasing group of CDW superconductors includes the layered transition metal dichalcogenides (2H-TaSe₂, 2H-TaS₂, 2H-NbSe₂ and 2H-NbS₂) and NbSe₃. The high- T_C cuprate superconductors and also the recently discovered iron-based class of superconductors exhibit CDW and SC together. It is a well known fact that CDW leads to a reconstruction of the band structure where the FS is nested [55]. Depending on the underlying band structure, the formation CDW can change the number of bands crossing the Fermi level. Therefore, even in one-band systems the formation of CDW order can result in two bands crossing the Fermi level. Thus, as mentioned earlier, one will have to deal with multi-band superconductivity. In this case, a CDW can coexist with SC. In those material where coexistence of CDW and SC transition found, it is observed that the CDW transition occur at a much higher temperature than that of the superconducting transition. It is also important to mention that the dielectric gap due to the CDW phase transition is much larger than the superconducting gap. Therefore, the question of interest is whether the gapping of the FS due to the CDW phase transition is favorable or destructive to the superconductivity which occurs at low temperatures.

Recently, it has been shown that certain materials known for exhibiting CDW ordering can also show SC simply by tuning the concentration of specific dopants or by application of external pressure. These tuning parameters modify the Fermi surface or the electron-phonon coupling, and thus tip the balance in favour of one or the other state as the choice of ground state, indicative of the competition between them. There are a variety of compounds which have established well the competition between SC and CDW. NbSe₂, TaS₂, (TaSe₂)₂I and NbSe₂ (pressure) [52, 56], TaS₂ (doping) [57] and Lu₅Ir₄Si₁₀ (pressure+doping) [18] are the best known examples for the competition that are being talked about in the present context. To certain extent there is some consensus on the stability of superconducting transition in the presence of density wave order. A strong case for the above scenario was observed in 2H-NbSe₂, exhibiting the coexistence of CDW and SC, which undergoes a CDW transition (T_{CDW}) at 33 K and a superconducting transition (T_{SC}) at 7.2 K. Figure 1.9 shows variation of T_{CDW} and T_{SC} in 2H-NbSe₂ as a function of pressure. The resistivity measurement in presence of a hydrostatic pressure upto 35 kbar showed that the CDW transition decreases linearly and above a pressure of 36 kbar the CDW transition completely disappears. Besides, it has clearly been observed that the

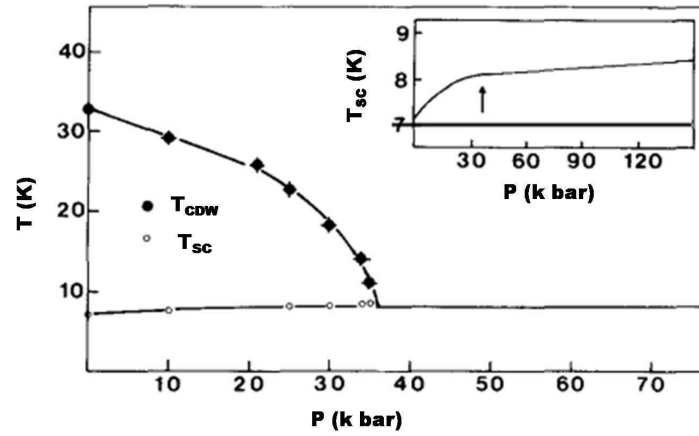


Figure 1.9: Pressure dependence of the CDW ordering, T_{CDW} and SC transition temperature, T_{SC} in 2H-NbSe₂ [courtesy [58]].

superconducting transition increases rapidly with pressure $T_{SC}(P)$ (5×10^{-5} K/bar) upto about 35 kbar, above which it remains nearly constant for high pressure upto 140 kbar, and thus this results gave the first clear evidence that the enhancement of superconductivity in 2H-NbSe₂ (and presumably in other MX₂ compounds) was due to the progressive removal of the CDW by the application of pressure.

However, there is also an opposite viewpoint [59, 60]. The superconducting transition temperature is theoretically shown to rise as a result of presence of the Peierls instability within a simple incomplete-nesting model in two dimensions. The implication of this is discussed for the high- T_C superconductors La_{2-x}M_xCuO₄. Such a situation has not been experimentally verified yet. The recently discovered iron based (pnictides) superconductors, (representatives of the quasi 2D systems), have renewed the interest to do a study exploring the competition between CDW/SDW and SC [10, 21, 61]. The interesting fact that the pnictide parent compound (for example, RFeAsO, AFe₂As₂) undergoes SDW transition at high temperatures along with a structural transition and the superconductivity in iron pnictides appears only after substituting the parent compounds with charge carriers [22, 62]. This type of competition of both kind of order ranging from concurrence to mutual cooperation has opened a new route for the materials that exhibit interplay of DW and SC behavior in addition to high T_C cuprates, so far considered as one of the greatest puzzles of contemporary solid state physics.

Thus the question about the interplay and competition between superconductivity and charge-density ordering remains of immense interest to both theoreticians and experimentalists alike.

1.4 Outline of the thesis

The aim of this thesis is to study the rare earth magnetism, competition/interplay of superconductivity (SC) and charge-density-wave (CDW) in rare earth ternary inter-metallic compounds with respect to crystal structure, transport, magnetic and thermal properties. As a part of study we have selected the compounds namely $\text{Lu}_2\text{Ir}_3\text{Si}_5$ and $\text{R}_2\text{Ir}_3\text{Sn}_5$ (R=rare earth) belonging to 2-3-5 family. Even though $\text{Lu}_2\text{Ir}_3\text{Si}_5$ have a three dimensional crystal structure, but it is reported that is one observes both SC and CDW transition in this compound, which is very unusual, as CDW are commonly observed in low dimensional materials. Hence, in order to perform a complete study of the subject, we have considered three compounds, where each of the atomic species in $\text{Lu}_2\text{Ir}_3\text{Si}_5$ is substituted by 3 different elements viz $(\text{Lu}_{1-x}\text{Sc}_x)_2\text{Ir}_3\text{Si}_5$, $\text{Lu}_2(\text{Ir}_{1-x}\text{Rh}_x)_3\text{Si}_5$ and $\text{Lu}_2\text{Ir}_3(\text{Si}_{1-x}\text{Ge}_x)_5$. In this context we have further explored the compounds $\text{R}_2\text{Ir}_3\text{Sn}_5$ with resembles the crystal structure of $\text{Lu}_2\text{Ir}_3\text{Si}_5$. It is of importance because the cell volume is larger than that of $\text{Lu}_2\text{Ir}_3\text{Si}_5$ and hence the possibility of appearance of CDW at high temperatures. In these compounds, we also extended our studies to magnetism and Kondo effect.

Chapter 2 focuses on the synthesis of both polycrystalline and single crystalline samples and various experimental techniques used for their characterization.

Chapter 3 describes the interplay and competition between SC and CDW ordering transition on pseudo ternary alloys of $\text{Lu}_2\text{Ir}_3\text{Si}_5$ to investigate the effects of atomic disorder $(\text{Lu}_{1-x}\text{Sc}_x)_2\text{Ir}_3\text{Si}_5$, density of states $\text{Lu}_2(\text{Ir}_{1-x}\text{Rh}_x)_3\text{Si}_5$ and lattice volume $\text{Lu}_2\text{Ir}_3(\text{Si}_{1-x}\text{Ge}_x)_5$ on both CDW and SC transition.

Chapter 4 describes the study of coexistence of CDW and SC in $\text{Lu}_2\text{Ir}_3\text{Si}_5$ single crystals.

Chapter 5 describes the synthesis of polycrystalline samples of $\text{R}_2\text{Ir}_3\text{Sn}_5$ (R=rare earth) and its systematic study of magnetic ordering, through the choice of compound, between local moments and surrounding of conduction electrons.

Chapter 6 describes the study of transport and magnetic properties in single crystals of $\text{Ce}_2\text{Ir}_3\text{Sn}_5$.

Finally, chapter 7 discusses the main outlook of the study and concludes the thesis.



Chapter 2

Experimental Techniques

2.1 Sample Preparation and characterization

In this thesis, we have investigated intermetallic compounds of the type $R_2T_3X_5$ where R is a rare-earth element, T is a transition metal element and X is Si, Ge or Sn. The measurements are reported in this thesis are for both polycrystalline and single crystalline samples. Polycrystalline samples were prepared by arc-melting appropriate amounts of constituent elements, the purity of the R and T elements were 99.99%, whereas that of Si, Ge and Sn were 99.999%, on a water cooled copper hearth under Ti-gettered atmosphere of continuously flowing high purity argon gas. Usually samples were re-melted several times and ascast ingots are annealed to get homogenous materials. For annealing procedure, samples were wrapped in Tantalum foil and sealed under vacuum of at least 10^{-5} mbar in a quartz tube and heated up to 950°C for ten days before slowly cooling down to room temperature. Single crystals used in this thesis work were grown by using Czochralski tetra-arc technique. A schematic view of the equipment is shown in Figure 2.1. The stoichiometric ratio of constituent elements were melted in a water-cooled copper crucible and heated by four arcs under argon atmosphere. The material continuously solidifies at the liquid-solid interface between the melt and polycrystalline or single crystalline seed, which is pulled out. In the absence of a seed crystal, a tungsten tip is used. To achieve thermal and compositional homogeneity, the crucible and the seed are counter-rotated at an appropriate speed. This influences the heat convection through the melt and in turn stabilizes the meniscus.

For the synthesis of single crystals $\text{Ce}_2\text{Ir}_3\text{Sn}_5$ and $\text{Lu}_2\text{Ir}_3\text{Si}_5$, we first prepared 12 gms of polycrystalline sample by melting the stoichiometric ratio of elements in a tetra-arc furnace. This was used then as the starting material for the crystal growth. A thin

tungsten seed rod was immersed into the melt and pulled at a speed of 11 mm/h in pure and dry argon atmosphere. After confirming the phase homogeneity of the grown crystal by using powder x-ray diffraction, we used the first prepared single crystal rod as a seed in order to synthesize good quality single crystals of $\text{Ce}_2\text{Ir}_3\text{Sn}_5/\text{Lu}_2\text{Ir}_3\text{Si}_5$. The as-grown ingot was approximately 3-4 mm in diameter and 6 cm in length.

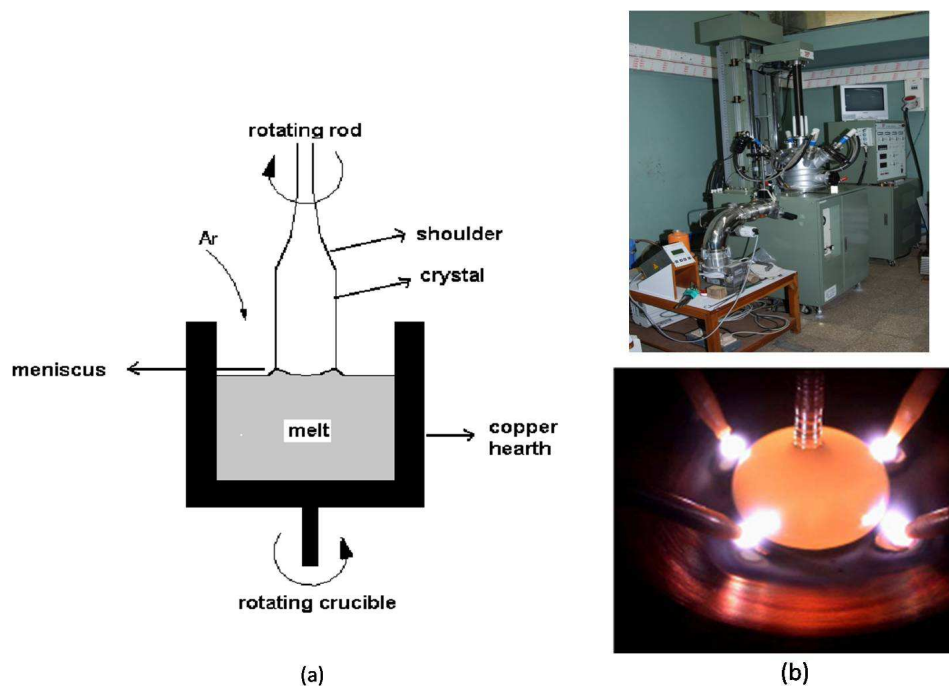


Figure 2.1: (a) A schematic diagram of the Czochralski growth arrangement. (b) Experimental set up of tetra-arc furnace and the photograph taken during crystal growth.

The phase of the as-grown samples were first confirmed by the EDAX-Energy Dispersive x-ray spectroscopy which is an analytical technique used for the elemental analysis and chemical characterization of a sample [64]. It relies on the investigation of a sample through interactions between electromagnetic radiation and matter, analyzing x-rays emitted by the matter in response to being hit with charged particles. The energy of x-ray gives a qualitative information on what elements were present in the given specimen and the intensity gives the quantitative information, as of what fraction of specimen is composed of the particular element. The crystals were also examined by using electron microprobe analysis (EPMA). The homogeneity of the composition is checked by imaging secondary electrons and by comparing the measured intensities with those of the standard sample. The homogeneity is checked on a polished surface of sample and the amount of the second phase was found to be of less than 1%.

2.1 Sample Preparation and characterization

Importantly, the phase purity of the grown single and polycrystalline samples were characterized at room temperature by means of x-ray powder diffraction using PANalytical commercial x-ray diffractometer with Cu $K\alpha$ radiation. A piece of the sample is finely crushed into a powder and a layer of such a powder is formed on a glass slide. This ensures that all sets of planes intercept the beam. A monochromatic x-ray beam falls on such a film and diffracts into many specific directions. The diffracted beam intensity peaks is satisfied for any set of planes when Bragg's law $n\lambda = 2d\sin\theta$, where 'n' is the order of diffraction, ' λ ' is the wavelength of the x-ray beam (Cu $K\alpha$ line of 1:5406 was used), 'd' is the distance between the diffracting planes and ' θ ' is half the angle between the incident and the diffracted beams [65]. By collecting data at different θ 's we obtain the entire diffraction pattern. This pattern is then compared and analyzed with the theoretical pattern expected for our compound in a program called FULLPROF [66].

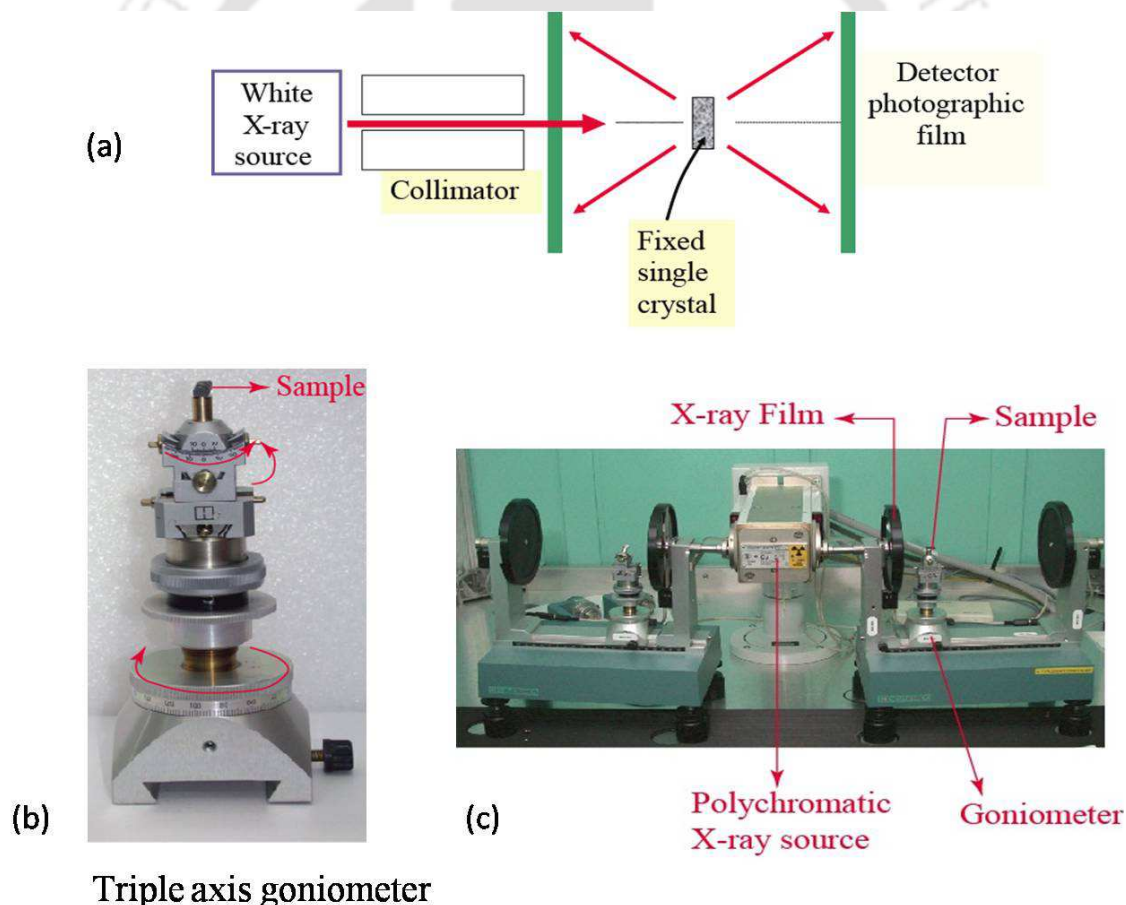


Figure 2.2: (a) A schematic of Laue Diffraction machine used to align the crystals. (b) Triple axis goniometer, where the sample is mounted on to fix a crystallographic axis. (c) Experimental set up of the Laue diffraction machine.

Single crystals were inspected by means of x-ray back scattering in standard Laue geometry. Figure 2.2 displays the Laue diffractometer, the goniometer used and the schematic diagram of Laue x-ray diffraction. The crystal is mounted on the goniometer (which can be rotated along all three axes as shown in Figure 2.2) such that x-ray beam falls on the plane we want to expose. Radiation from anode was used as an incident beam and beam reflected from the sample recorded on a photographic film [65]. The Laue diffraction pattern from the crystal is observed on a photographic film as a regular array of spots. This Laue spots gives information about the orientation of the crystal. The difference between this method and the powder diffraction method described earlier is that the angle is kept constant here and the wavelength is effectively varied due to the polychromatic nature of the source. The pattern obtained on the film helps us to orient the crystal according to the plane we require. After proper orientation by means of Laue technique, samples with desired shape and dimensions are cut by means of spark-erosion in an oil bath to prevent oxidation. On the other hand polycrystalline samples were cut in an oil bath by using diamond cutter.

2.2 Measurement Techniques

2.2.1 Electrical Resistivity Measurements

Electrical resistivity is one of the important tools to understand the transport properties of a material. For any kind of phase transition, temperature vs resistivity graph shows a change of slope due to decrease in spin, charge disorder scattering. The temperature dependence of the electrical resistivity between 1.5 to 300 K was measured by standard four-probe method in a glass cryostat assembly with an outer cryostat in which we put liquid nitrogen and an inner cryostat in which liquid He is transferred. The resistivity insert consists of two concentric thin walled stainless steel tubes which are dipped in liquid He. The sample rod goes into the inner tube and maintaining the vacuum between the two tubes gives us control over the cooling and heating power. The temperature control is achieved by a Lake Shore temperature controller (DRC-93CA). The resistivity was read on the LR-700 (Linear Research USA) AC resistance bridge with a typical accuracy of 100 n Ω . Figure 2.3 shows a block diagram of the resistivity measurement setup. Electrical contacts were made by using silver paint and gold wires of 100 μm thickness on single/polycrystalline samples cut in shape of a rectangular bar. Although the sensitivity of the resistance measurement was 100 n Ω the absolute accuracy of the resistivity data

is only about 10% due to errors introduced in the estimation of geometric factors and possible micro-cracks in the samples.

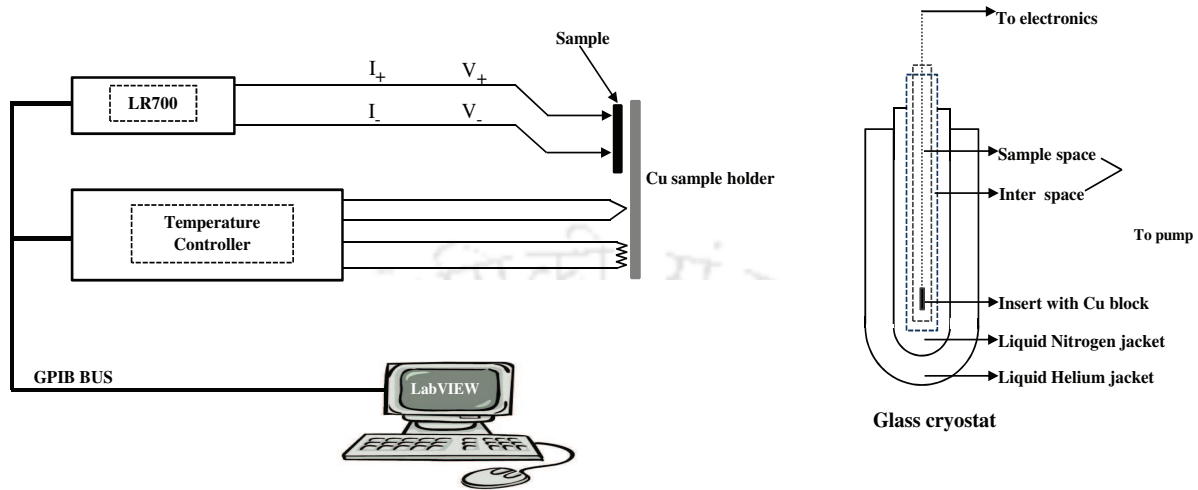


Figure 2.3: A schematic block diagram of the resistivity set up via a four probe technique. At a time four different samples can be measured.

2.2.2 Magnetic Susceptibility Measurements

The dc susceptibility measurements between 1.8 to 300 K and isothermal magnetization measurements in fields upto 7 Tesla, were performed using a commercial Superconducting Quantum Interference Device (SQUID) magnetometer (MPMS5, Quantum Design, USA). The isothermal magnetization measurements on some of the samples in presence of fields upto 12 Tesla were carried out in Vibrating Sample Magnetometer (VSM) (Oxford instruments, UK). The dc magnetization measurement using both the SQUID and VSM involve motion of the sample within a magnet. In a VSM the sample motion gives rise to induced voltages in pick-up coils surrounding the sample and is detected by a lock-in amplifier. In a SQUID magnetometer as the sample moves through the detection coils, the magnetic moment of the sample induces an electric current in the coils. Since the SQUID functions has a highly linear current-to-voltage converter, the variations in the current in the detection coils produce corresponding variations in the SQUID output voltage which are proportional to the magnetic moment of the sample. The movement of the sample results in an oscillating induced ac current signal that is detected by the SQUID sensor. The sensitivity obtained in SQUID is of the order of 10^{-7} - 10^{-8} emu whereas the sensitivity obtained in the VSM is $\sim 10^{-6}$ emu [67].

2.2.3 Heat Capacity Measurements

The heat capacity measurements in zero and non-zero field data for the temperature range from 1.5 to 300 K were carried out on the Physical Property Measurement System (PPMS, Model P 650). The set up uses thermal relaxation technique, to measure specific heat of the sample, that controls the heat added to and removed from a sample while monitoring the resulting change in temperature. A known amount of heat is applied at constant power for a fixed time and then this heating period is followed by a cooling period of the same duration. The heat capacity puck utilizes the standard PPMS 12 pin format for electrical connections, and it provides a small microcalorimeter platform for mounting the sample. Samples are mounted to this platform by a standard cryogenic grease or adhesive such as Apiezon N or H Grease. Typical mass of the sample used was of the order of 10s of mg. A single heat capacity measurement consists of several distinct stages. First, the sample platform and puck temperatures are stabilized at some initial temperature. Power is then applied to the sample platform heater for a pre determined length of time, causing the sample platform temperature to rise. When the power is terminated, the temperature of the sample platform relaxes towards the puck temperature. The sample platform temperature is monitored throughout both heating and cooling, providing the raw data of the heat capacity calculation. The raw data are analyzed by the two-tau model [68] which assumes that the sample is not in good thermal contact with the sample platform. The values of the heat capacity and other physical parameters are determined by optimizing the agreement between the measured data and the two-tau model. In the two-tau model, the first time constant (τ_1) represents the relaxation time between the sample platform and the puck, and the second time constant (τ_2) represents the relaxation time between the sample platform and the sample itself. A second analysis is also performed using a simpler model that assumes perfect thermal coupling between the sample and the sample platform. The heat capacity software determines which model fits best the measured data. The heat capacity of the sample is determined by subtracting the addenda from the total heat capacity.

2.2.4 Differential Scanning Calorimetry

Differential scanning calorimetry (DSC) measurements were carried out in temperature range between 120 and 320 K using bulk samples in a hermetically sealed aluminum pan. For the specific heat measurements, a “baseline” run with empty aluminum pans in the sample and reference holders is initially run. The sample is inserted into the sample

aluminum pan and an identical sweep then followed. During both the runs, the differential power is measured as a function of time (temperature) [69].

DSC is a thermo-analytic technique in which the difference in the amount of heat required to increase the temperature of a sample and a reference material is measured as a function of temperature. The DSC curves are recorded either under a constant heating (or cooling) rate or under isothermal conditions (time scan at a constant temperature). A typical DSC set up consists of two isolated sealed pans, one containing the sample and the other a reference material (generally, Al_2O_3 or just the empty Al pan). The two pans are heated or cooled uniformly while the heat flow difference between the two is monitored. The basic principle underlying this technique is the following, when the sample undergoes a physical transformation such as phase transition, more or less heat will need to flow to it in comparison with the reference in order to maintain both at the same temperature. More or less heat flowing to the same would depend on the process being endothermic or exothermic. In the power compensation type DSC, heat is supplied to either of the pans so that both are maintained at the same temperature. The heat flow (dH/dt) is then estimated from this data. In a DSC based on the heat-flux technique, the temperature difference (T) between the two isolated pans is measured from which the heat flow is estimated.



Chapter 3

Interplay of superconductivity and charge density wave ordering in $\text{Lu}_2\text{Ir}_3(\text{Si}_{1-x}\text{Ge}_x)_5$, $\text{Lu}_2(\text{Ir}_{1-x}\text{Rh}_x)_3\text{Si}_5$ and $(\text{Lu}_{1-x}\text{Sc}_x)_2\text{Ir}_3\text{Si}_5$ systems

3.1 Introduction: CDW transition in $\text{Lu}_2\text{Ir}_3\text{Si}_5$

As we have seen in chapter 1, CDW is observed in quasi-low-dimensional (2D/1D) materials. It was therefore a bit of a surprise when CDW ordering was observed in $\text{Lu}_2\text{Ir}_3\text{Si}_5$, a compound which has essentially a 3-dimensional structure. The compound shows superconducting transition at 3.5 K and undergoes another phase transition below 190 K which has been shown to be a strongly coupled charge density wave ordering [19, 70]. Transmission electron microscopy (TEM) studies by Lee *et.al.*, revealed the direct evidence of CDW formation with observation of CDW superlattice reflections [71]. Among other isostructural compounds of the series $\text{R}_2\text{Ir}_3\text{Si}_5$, only $\text{Er}_2\text{Ir}_3\text{Si}_5$ shows a signature of CDW transition at 150 K [72]. However, 5-4-10 systems $\text{R}_5\text{Ir}_4\text{Si}_{10}$ (R=Lu, Dy, Ho, Er, Tm and Yb), adopts 3D structure, have been shown to exhibit similar CDW transition in their measurements, among which many of them showed coexistence of magnetism/superconductivity and CDW transition [9, 73]. Their results imply that the transition temperature of the CDW is affected either by chemical pressure or external pressure. A significant effect in the variation of transition temperature of CDW and SC of $\text{Lu}_5\text{Ir}_4\text{Si}_{10}$ has been reported on application of (chemical) pressure or by changing the density of electrons in the Fermi surface [74].

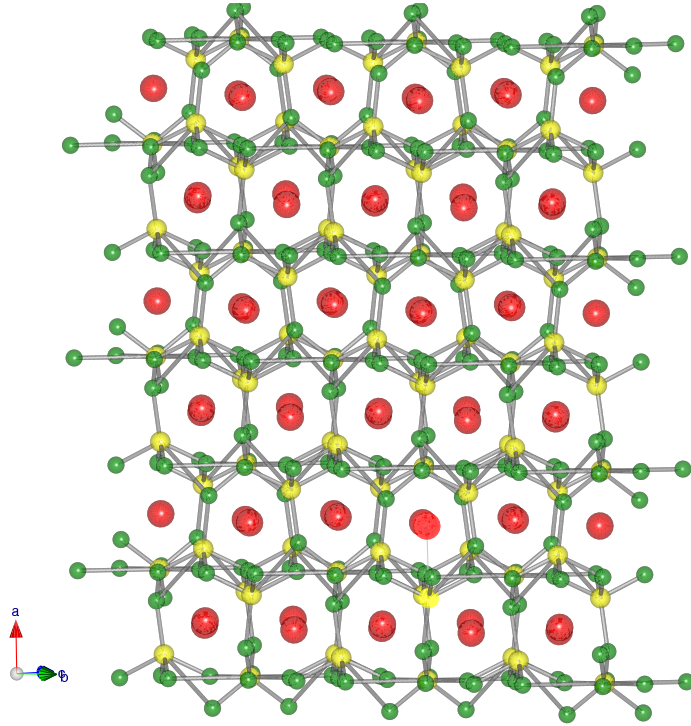


Figure 3.1: The crystal structure of $\text{Lu}_2\text{Ir}_3\text{Si}_5$. The large (red) spheres correspond to the Lu atom, Ir atoms with medium (yellow) spheres and Si atoms with small (green) spheres.

To appreciate why the observation of CDW ordering in these 3D compounds ($\text{Lu}_2\text{Ir}_3\text{Si}_5$ and $\text{Lu}_5\text{Ir}_4\text{Si}_{10}$) in contrast to that of the conventional low dimensional CDW systems discussed in chapter 1, let us look at the crystal structure of $\text{Lu}_2\text{Ir}_3\text{Si}_5$ compound. Figure 3.1 shows unit cell of $\text{Lu}_2\text{Ir}_3\text{Si}_5$ which adopts the orthorhombic $\text{U}_2\text{Co}_3\text{Si}_5$ type structure. The Ir-Si-Ir bond formed as a cage around Lu atom. The Lu atoms form a two dimensional array with the shortest Lu - Lu distance of 3.911 Å. One observes the absence of transition metal (Ir-Ir) contacts. Further Ir and Si atoms form planar rings which are stacked parallel to the basal plane which are connected along the *c*-axis via Ir-Si-Ir zigzag chains. The Lu atoms form a quasi one-dimensional zigzag chain along the *c*-axis which are well separated from Ir-Si ring. The distance between adjacent Lu-Lu and Ir-Ir atoms are large, whereas Ir-Si and Si-Si distances are small, thereby indicating strong covalent interactions. By analyzing the distances between other atoms, these Lu atoms have the shortest distance with respect to all other bonds; suggesting a quasi-1D conducting channel in the Lu - Lu chain, developing along the *c*-axis. A relook at the crystal structure of $\text{Lu}_5\text{Ir}_4\text{Si}_{10}$ [48] reveals that the main features of the structural arrangement are almost identical to that of $\text{Lu}_2\text{Ir}_3\text{Si}_5$. In both compounds, if one observes the crystal structure

along the c -axis, the Lu atoms are found to be placed in the center of the Ir-Si rings. The Lu atoms form a quasi-one dimensional chain along the c -axis which is separated from the rings. Eventhough the crystal structure has a 3D nature, the origin of CDW in this compound is most probably related to quasi one dimensional chain formed by Lu atoms along the c -axis.

Hence, in order to gain a comprehensive understanding of the coexistence/ competition/interplay of charge density wave with superconductivity, we have used pseudo-ternary system of $\text{Lu}_2\text{Ir}_3\text{Si}_5$ to investigate the effects of the lattice volume $\text{Lu}_2\text{Ir}_3(\text{Si}_{1-x}\text{Ge}_x)_5$, atomic disorder $(\text{Lu}_{1-x}\text{Sc}_x)_2\text{Ir}_3\text{Si}_5$ and the density of states at the Fermi level $\text{Lu}_2(\text{Ir}_{1-x}\text{Rh}_x)_3\text{Si}_5$ on both CDW and superconductivity. $\text{Lu}_2\text{Ir}_3\text{Ge}_5$ is isostructural to that of $\text{Lu}_2\text{Ir}_3\text{Si}_5$ but differs only by the size of unit cell, hence one would expect a CDW transition also in $\text{Lu}_2\text{Ir}_3\text{Ge}_5$. However, $\text{Lu}_2\text{Ir}_3\text{Ge}_5$ is found to show only a superconducting transition below 1.8 K without any signature of CDW ordering [75]. Thus it is of interest to investigate how the CDW and SC evolve when we substitute Ge in the Si site of $\text{Lu}_2\text{Ir}_3\text{Si}_5$. Further, it is well-known that in 2-3-5-systems density of electrons in the Fermi surface is governed mostly by the transition metals [76]. Hence it is of interest to examine the influence of Rh at Ir site of this compound, as it has been already established that $\text{Lu}_2\text{Rh}_3\text{Si}_5$ show normal behavior till 1.8 K [77]. Furthermore, it would be of interest to see the influence of Sc on the Lu site, as it was demonstrated earlier that the Lu atom was responsible for the origin of CDW in $\text{Lu}_5\text{Ir}_4\text{Si}_{10}$ [48].

This chapter deals with the evolution of the superconducting transition temperature T_{SC} and the charge density wave ordering temperature T_{CDW} in pseudo-ternary alloy system $(\text{Lu}_{1-x}\text{Sc}_x)_2\text{Ir}_3\text{Si}_5$, $\text{Lu}_2(\text{Ir}_{1-x}\text{Rh}_x)_3\text{Si}_5$ and $\text{Lu}_2\text{Ir}_3(\text{Si}_{1-x}\text{Ge}_x)_5$.

3.2 Experiment

The polycrystalline samples of $(\text{Lu}_{1-x}\text{Sc}_x)_2\text{Ir}_3\text{Si}_5$, $\text{Lu}_2(\text{Ir}_{1-x}\text{Rh}_x)_3\text{Si}_5$ and $\text{Lu}_2\text{Ir}_3(\text{Si}_{1-x}\text{Ge}_x)_5$ were prepared by arc melting the stoichiometric mixtures of constituent elements (the purity of Lu, Si, Ge - 99.999%; and that of Sc, Ir, Rh - 99.99%) on a water cooled copper hearth within a Ti-gettered argon atmosphere. The resulting ingots were flipped over and remelted at least six times to promote the homogeneity of the mixture. The samples were wrapped in the Tantalum foil, then sealed in a quartz tube under vacuum and finally annealed at 1000°C for ten days. The room temperature powder x-ray diffraction (XRD) with Cu $K\alpha$ radiation was taken on the annealed samples by using PANalytical commercial x-ray diffractometer. A commercial superconducting quantum interference

device (SQUID) magnetometer (MPMS5, Quantum Design, USA) was used to measure dc magnetic susceptibility in the temperature range from 1.8 to 300 K for the field of 10 Oe to estimate the superconducting transition and in the field of 5 T to look at the CDW transition in the temperature range of 50 to 300 K. The temperature dependence of the electrical resistivity between 1.8 and 300 K was measured using a home built electrical resistivity set up with the standard dc four probe technique. The specific heat data were taken on the samples in zero field between 1.8 to 10 K using a commercial physical property measurement system (PPMS, Quantum Design, USA) whereas for the temperature between 120 to 300 K, it was measured in a commercial DSC system to probe the CDW transition.

3.3 Results

3.3.1 $\text{Lu}_2\text{Ir}_3(\text{Si}_{1-x}\text{Ge}_x)_5$

3.3.1.1 X-ray diffraction studies

The x-ray diffraction (XRD) pattern of the samples clearly reveals the absence of any impurity phase and also confirms that the samples crystallize in the $\text{U}_2\text{Co}_3\text{Si}_5$ type of structure with the space group $Ibam$. The lattice constants a , b and c were estimated

x	a (Å)	b (Å)	c (Å)	v (Å ³)	c/a
0.00	9.915	11.287	5.722	640.298	0.5771
0.004	9.917	11.302	5.728	641.982	0.5775
0.01	9.924	11.302	5.732	642.945	0.5776
0.02	9.926	11.331	5.738	645.349	0.5781
0.05	9.910	11.348	5.748	646.340	0.5800
0.10	9.909	11.389	5.759	650.008	0.5812
0.15	9.854	11.423	5.786	651.285	0.5872
0.20	9.709	11.562	5.984	671.790	0.6163

Table 3.1: Lattice parameters of $\text{Lu}_2\text{Ir}_3(\text{Si}_{1-x}\text{Ge}_x)_5$

from the Reitveld fit of their powder x-ray diffraction patterns by using the FULLPROF

program [78]. The refinement was done using the site occupation for constituent elements determined by the electron probe micro analyzer (EPMA), shown in Figure 3.2.

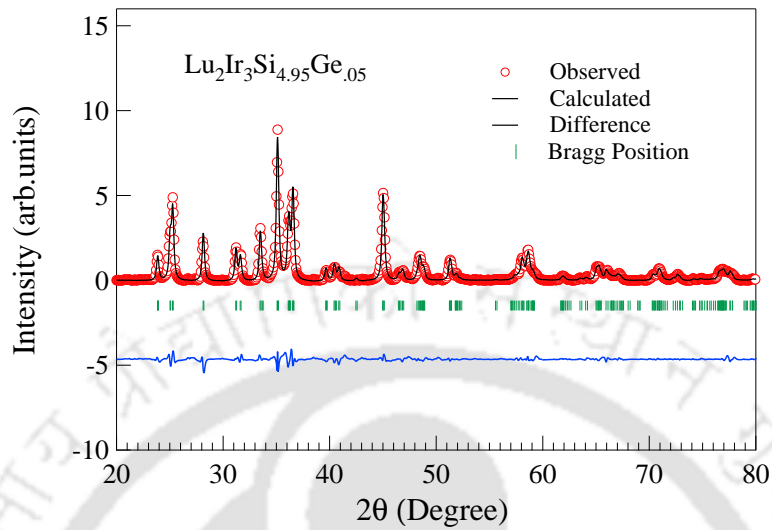


Figure 3.2: Powder x-ray diffraction data of the $\text{Lu}_2\text{Ir}_3\text{Si}_{4.95}\text{Ge}_{0.05}$. The solid line represents the simulated data using FULLPROF (Reitveld Program).

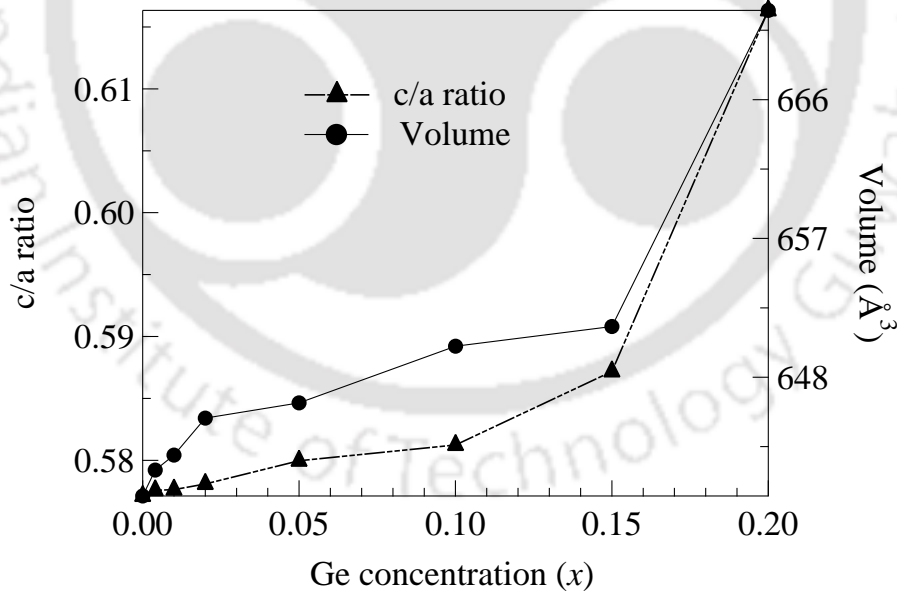


Figure 3.3: Ge (x) concentration dependence of the c/a ratio and volume for $\text{Lu}_2\text{Ir}_3(\text{Si}_{1-x}\text{Ge}_x)_5$, ($x = 0.00, 0.004, 0.01, 0.02, 0.05, 0.1, 0.15$ and 0.2).

The results are listed in Table 3.1 and the corresponding unit cell volume and c/a ratio

are plotted in Figure 3.3. The a -axis of the unit cell increases progressively as the Ge concentration increases upto 2 % ($x < 0.02$) in the alloy and above which the value it decreases whereas, the lattice volume and the c/a ratio increases linearly upon Ge doping as shown in Figure 3.3. Even though EPMA shows contrast in the photograph, the ratio of the constituent elements does not show any significant variation at various regions of the sample. We also have performed an energy-dispersive x-ray analysis and confirmed the stoichiometry of $\text{Lu}_2\text{Ir}_3(\text{Si}_{1-x}\text{Ge}_x)_5$ ($x = 0.0 - 0.2$) crystals as well.

3.3.1.2 Magnetic susceptibility studies

Figure 3.4 and Figure 3.5 show the temperature dependence of the dc susceptibility for the pseudo ternary alloys of $\text{Lu}_2\text{Ir}_3(\text{Si}_{1-x}\text{Ge}_x)_5$ for low concentration of $x=0.00 - 0.02$ and $x=0.05 - 0.2$ respectively. The left panels in the figure show the low temperature (1.8 to 10 K) zero field cooling data (ZFC) (it is warming data in a field after the sample was cooled in zero field) data in the field of 1 mT to observe the existence of superconductivity in the samples. The field cooling data (FC) (sample was cooled in the presence of the field and then warming up data in presence of field was recorded) does show a bifurcation from the ZFC data at the onset of the diamagnetic signal. The superconducting transition is clearly seen with the appearance of the diamagnetic signal around the ordering region, however, the transition is not complete till 1.8 K and shows features of superconductivity. The superconducting transition temperature for the undoped sample ($x = 0.00$) matches with the previously reported value [70], but it is 2 K higher than that reported by Singh *et.al.*, [19]. The difference can be seen with all the doped compounds which may be due to the disorder, defects or inhomogeneities (on the atomic scale) present in our samples. We suspect that the differences in the transition temperature, T_{SC} are caused by strain induced disorder in the sample arising from defects or localized atomic disorder. Hence as the chemical pressure is not uniform throughout the sample, so different regions undergo transitions at different temperatures and hence the two step transition was observed. It can also be related to the presence of a different phase suggested by the EPMA result.

The right panels show the susceptibility data over temperatures from 100 to 300 K in a field of 5 T to highlight the CDW transition. The diamagnetic drop in χ (right panels of the figure) is the striking feature of the CDW transition for the nonmagnetic samples, which is consistent with the previous result [19]. This is attributed to a reduction of the electronic density of states at the Fermi level which results in the partial opening of an energy gap at the Fermi level. It can immediately be seen that even a small Ge concentration affects the CDW strongly. As the Ge concentration increases in the alloy

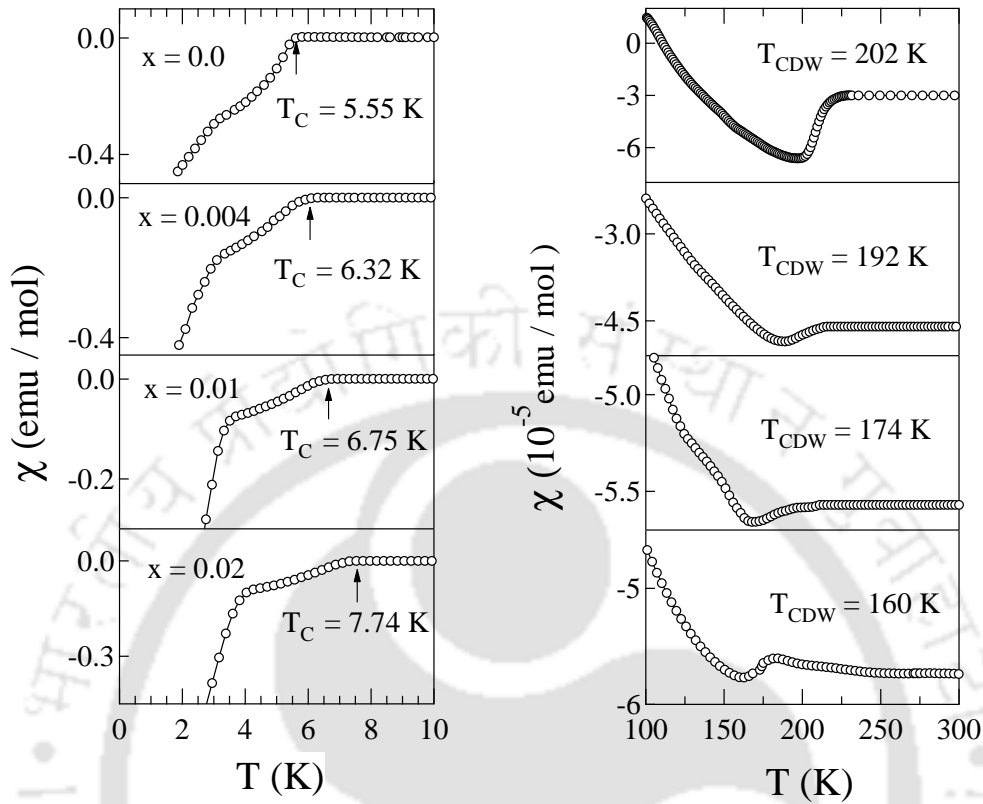


Figure 3.4: The temperature dependence of the dc susceptibility for the samples of $\text{Lu}_2\text{Ir}_3(\text{Si}_{1-x}\text{Ge}_x)_5$ with $x = 0.00, 0.004, 0.01$ and 0.02 . The left panels demonstrate low temperature behavior of dc susceptibility which highlights superconducting transition. The right panels show the CDW transition for these samples.

from $x = 0.00$ to $x = 0.02$, T_{CDW} starts to decrease from 200 K corresponding to the undoped sample $\text{Lu}_2\text{Ir}_3\text{Si}_5$, down to 160 K and then increases gradually upto 231 K for the higher concentration of Ge ($x > 0.02$) (see the right panels of Figure 3.4). The value of the T_{CDW} is determined by the peaks in the derivative ($d\chi/dT$ vs T) plots. Importantly, there is a corresponding change in the superconducting transition temperature T_{SC} . The observed transition temperature varies systematically as a function of x ; the T_{SC} rises to a maximum value of 7.7 K for $x = 0.2$ and then drops to 3.6 K (see the left panel of Figure 3.5). It is interesting to note that both SC and CDW orderings do not vanish even with 20 % of the Ge substitution in the alloy. Moreover, they compete with each other. We shall return to this point as we discuss further.

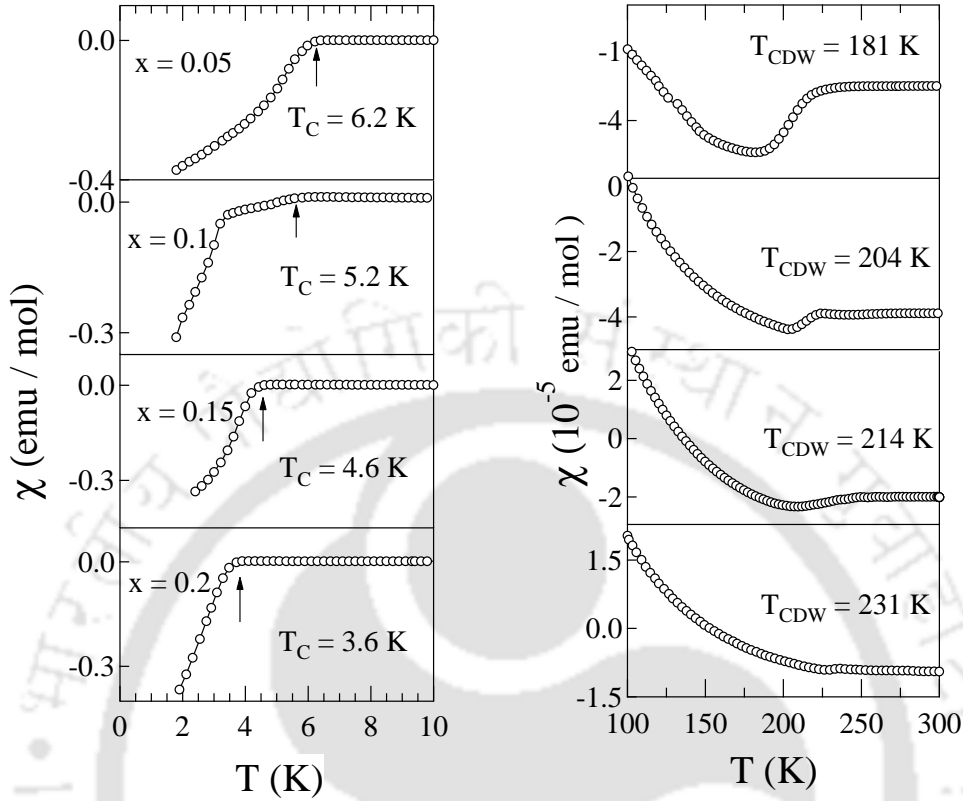


Figure 3.5: The temperature dependence of the dc susceptibility for the samples of $\text{Lu}_2\text{Ir}_3(\text{Si}_{1-x}\text{Ge}_x)_5$ with $x = 0.05, 0.1, 0.15$ and 0.2 . The left panel demonstrates low temperature behavior of dc susceptibility which highlights superconducting transition. The right panels panel show the CDW transition.

3.3.1.3 Resistivity studies

Figure 3.6 and Figure 3.7 are the plots of the normalized electrical resistivity as a function of temperature from 1.8 to 300 K of the pseudo-ternary systems $\text{Lu}_2\text{Ir}_3(\text{Si}_{1-x}\text{Ge}_x)_5$ for $x = 0.00, 0.004, 0.01$, and 0.02 and for $x = 0.05, 0.1, 0.15$ and 0.2 respectively. The main panel demonstrates the CDW transition at higher temperatures. The insets of the figure show the low temperature behavior of resistivity between 1.8 to 9 K, where we can clearly observe a sharp drop in resistivity at a certain temperature, highlighting the SC transition. Again, the resistive drop does not become zero till 1.8 K, in corroboration of the low temperature susceptibility data. We anticipate that the resistivity for the above compounds will go to zero below 1.8 K, the lowest temperature available in our set up.

It is to be noted that $\rho(T)$ at higher temperatures depicts the semimetallic CDW

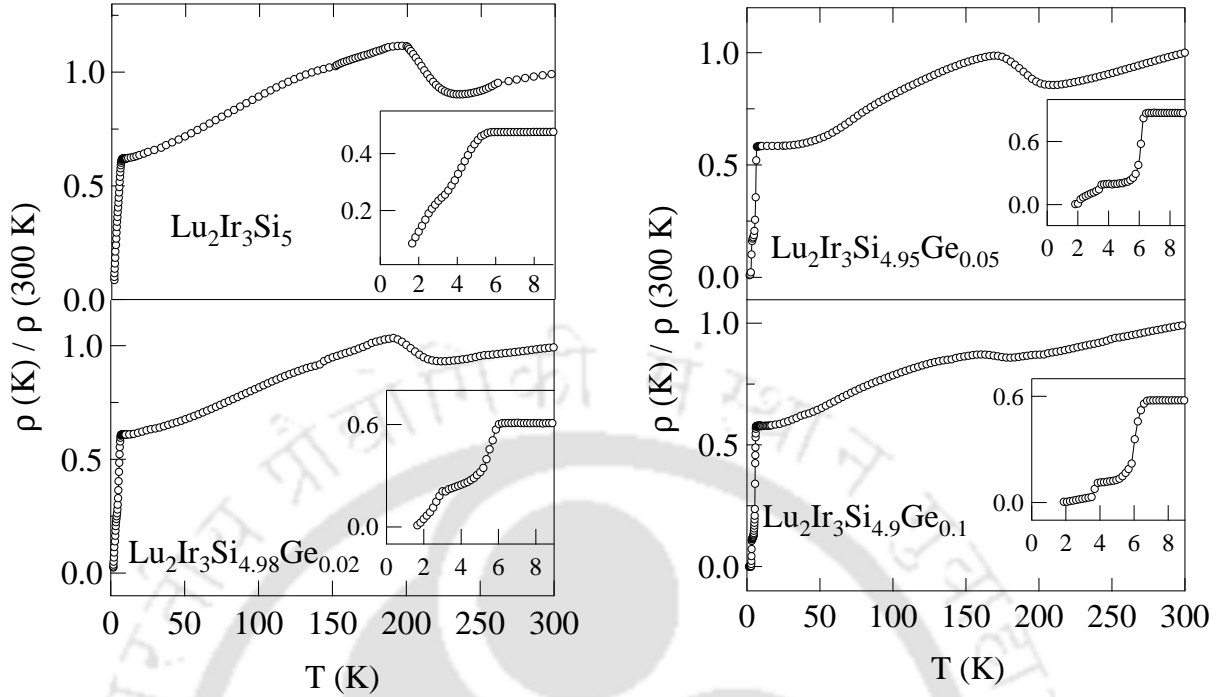


Figure 3.6: The temperature dependence of the electrical resistivity for $\text{Lu}_2\text{Ir}_3(\text{Si}_{1-x}\text{Ge}_x)_5$ with $x = 0.00, 0.004, 0.01$ and 0.02 . The main panels shows the variation of resistivity from 1.8 to 300 K. The insets show resistivity data between 1.8 to 9 K to highlight SC transition.

character of the pseudo-ternary alloys of $\text{Lu}_2\text{Ir}_3(\text{Si}_{1-x}\text{Ge}_x)_5$. The multiple transition at the low temperature region corroborates with the susceptibility data and may have its origin in the EPMA results. It is noticed that the step in the transition gradually vanishes with the increase in Ge concentration and the plausible explanation is that it occurs due to the relaxation of the lattice chain via lattice expansion. The upturn in the resistivity data at higher temperatures occur due to the opening up of a gap at the Fermi level indicating the CDW ordering. After reaching the maximum, the resistivity continues to show metallic behavior down to the lowest temperature and then finally undergoes the superconducting transition. Thus the electronically separated phase transition is associated with the metal-insulator-metal transition due to the partial gap of the Fermi surface. We also observe an increase in T_{SC} (from 5.5 to 7.7 K) as the Ge concentration increases from $x = 0.004$ to $x = 0.02$, while T_{CDW} shifts to lower temperatures (from 200 to 160 K) for these samples (see Figure 3.6). For the samples with a higher Ge substitution, a reverse trend is observed in both the T_{SC} and T_{CDW} transition [*i.e.* the decrease in the SC transition temperature while the CDW ordering temperature is enhanced from 160 to 231 K (see

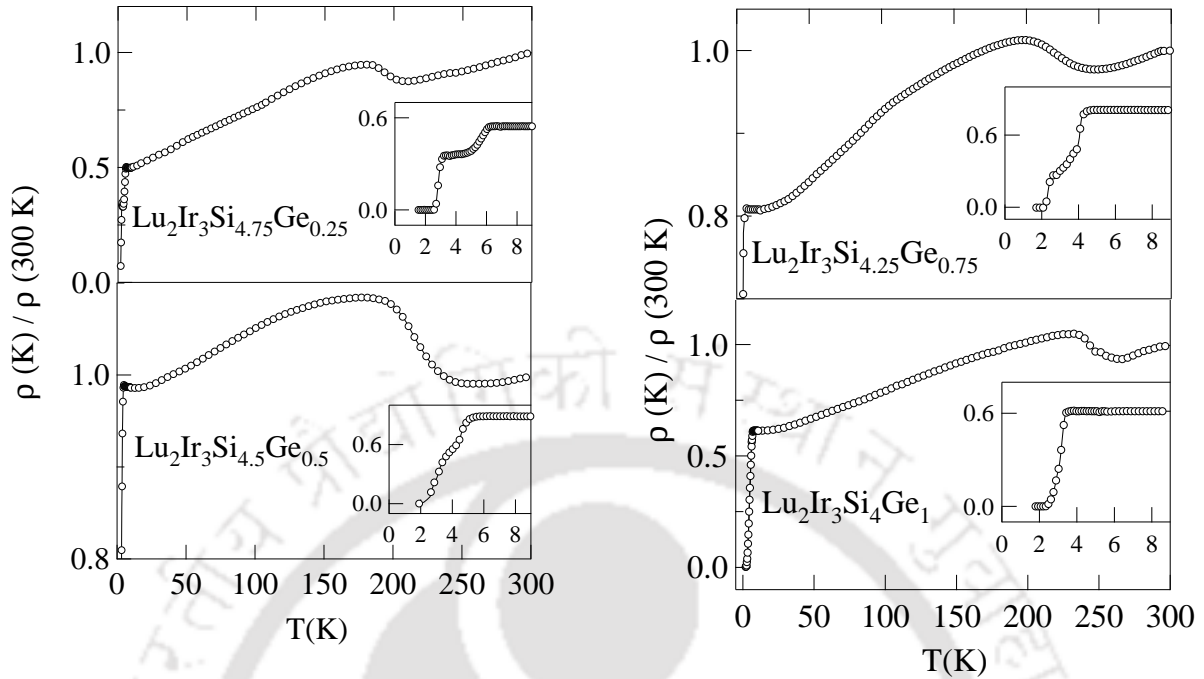


Figure 3.7: The temperature dependence of the electrical resistivity for $\text{Lu}_2\text{Ir}_3(\text{Si}_{1-x}\text{Ge}_x)_5$ with $x = 0.05, 0.1, 0.15$ and 0.2 . The main panels shows the variation of resistivity from 1.8 to 300 K. The insets show resistivity data between 1.8 to 9 K to highlight SC transition.

Figure 3.7)]. The dc susceptibility data are in good agreement with the above inference.

It has been suggested that the CDW formation and superconductivity are competing phenomena, since both compete for the density of states near the Fermi surface. Hence the presence of impurities in a CDW material may lead to a change in the CDW transition temperature and also possible smearing of the CDW transition. In addition to impurity, scattering of electrons and inducing a finite electron lifetime may also induce Friedel oscillations in the electron-charge distribution, leading to a static lattice distortion which leads to the modification of the CDW transition temperature [9]. All these facts may contribute in its own way and hence the CDW transition temperature shows a modulation as the amount of Ge in the alloy $\text{Lu}_2\text{Ir}_3(\text{Si}_{1-x}\text{Ge}_x)_5$ varies.

T_{CDW} is determined from the temperature of the peak position in the plot of $d\rho/dT$ vs T and the transition width ΔT_{CDW} is defined by the full width at half maximum (FWHM) of the peaks at the transition, as observed in the derivatives of the resistivity data. The temperature dependence of the CDW transition temperature T_{CDW} , the

x	T_{CDW} (K)	$\frac{\Delta\rho}{\rho(300K)}$ (%)	$\frac{\Delta T_{CDW}}{T_{CDW}}$ (%)	T_C (K)
0.00	200	22	14	5.5
0.004	192	11	13	6.3
0.01	174	12	12	6.8
0.02	160	3.4	12	7.7
0.05	181	16	14	6.2
0.10	204	10	16	5.2
0.15	214	15	18	4.6
0.20	231	10	9	3.6

Table 3.2: CDW transition parameters obtained from the temperature dependence of the resistivity of $\text{Lu}_2\text{Ir}_3(\text{Si}_{1-x}\text{Ge}_x)_5$.

amplitude of the anomaly in resistivity $\Delta\rho/\rho(300\text{ K})$, the superconducting transition temperature T_{SC} for the different composition of the alloy $\text{Lu}_2\text{Ir}_3(\text{Si}_{1-x}\text{Ge}_x)_5$ and the sharpness of the transition $\Delta T_{CDW}/T_{CDW}$ are listed in the Table 3.2. One can see that the reduction of $\Delta\rho$ and ΔT_{CDW} anticorrelates with the T_{SC} increase for the Ge concentration ratio between 0.00 and 0.02. In the region of doping concentration, $x = 0.05 - 0.2$, the value of $\Delta\rho$ does not show any change which may be due to the saturation of the influence of disorder in the system.

3.3.1.4 Heat-capacity studies

The temperature dependence of heat capacity (C_P) for $\text{Lu}_2\text{Ir}_3(\text{Si}_{1-x}\text{Ge}_x)_5$ is fitted above the superconducting transition using the given expression,

$$C_{Tot} = C_{elec} + C_{Ph} = \gamma T + \beta T^3, \quad (3.1)$$

where C_{elec} is due to the electronic contribution and C_{Ph} is due to the phonon contribution, with γ and β being constants. From the γ and β values, we can calculate the enhanced density of states at the Fermi level,

$$N^*(E_F) = 3\gamma/2\pi^2 N x k_B^2 \quad (3.2)$$

as well as the Debye temperature,

$$\theta_D = \left(\frac{12\pi^4 N x k_B}{5\beta} \right)^{1/3} \quad (3.3)$$

where N is the Avogadro number, x is the number of atoms per formula unit, and k_B is the Boltzmann constant. Using the value of θ_D and T_{SC} , we can calculate the electron phonon scattering parameter, λ_{SC} , from McMillan's theory[63], the expression is given as,

$$\lambda_{SC} = \frac{1.04 + \mu^* \ln(\theta_D/1.45 T_{SC})}{(1 - 0.62\mu^*) \ln(\theta_D/1.45 T_{SC}) - 1.04} \quad (3.4)$$

Hence, the bare density of states is obtained as,

$$N(E_F) = N^*(E_F)/(1 + \lambda_{SC}) \quad (3.5)$$

The estimated superconducting parameters from C_P data are presented in Table 3.3.

x	γ ($J/molK^2$) $\times 10^{-3}$	Θ_D	$N^*(E_F)$ (states/eV)	λ_{ep}	$N(E_F)$ (states/eV)
0.00	7.5	376	0.17	0.54	0.11
0.004	8.7	367	0.19	0.57	0.12
0.01	9.1	367	0.20	0.59	0.13
0.02	9.7	348	0.22	0.62	0.14
0.05	8.5	318	0.19	0.59	0.11
0.10	7.9	299	0.17	0.57	0.10
0.15	6.9	295	0.15	0.55	0.09
0.20	5.7	284	0.13	0.52	0.08

Table 3.3: Parameters obtained from the low temperature specific heat data of $\text{Lu}_2\text{Ir}_3(\text{Si}_{1-x}\text{Ge}_x)_5$.

The heat capacity data in the temperature range from 120 to 300 K for the compounds $\text{Lu}_2\text{Ir}_3(\text{Si}_{1-x}\text{Ge}_x)_5$ are shown in Figure 3.8 and Figure 3.9. The observed specific heat, C_P is a combination of the contribution from the lattice background and anomalous peaks. Clearly the anomaly, in the heat capacity found in each compound, denotes the CDW ordering of the compound. The peaks appear to be reduced in magnitude and

x	T_{CDW} (K)	ΔC_{CDW} (J/molK)	$\frac{\Delta C_{CDW}}{C_{CDW}}$ (%)	ΔS_{CDW} (J/molK)	ξ_0 (Å)
0.00	207	45	25	1.52	5.4
0.004	193	24	18	1.04	6.8
0.01	176	8.7	6.9	0.74	9.66
0.02	164	5.5	3.2	0.21	11.37
0.05	179	3.1	2.4	0.12	13.54
0.10	202	2.2	1.4	0.09	14.85
0.15	215	1.5	0.97	0.07	16.68
0.20	232	0.5	0.34	0.05	23.67

Table 3.4: Parameters obtained from the specific heat data of $\text{Lu}_2\text{Ir}_3(\text{Si}_{1-x}\text{Ge}_x)_5$.

broadened compared to the anomaly seen in the data for $\text{Lu}_2\text{Ir}_3\text{Si}_5$. It is noted that T_{CDW} measured from C_P measurements is consistent with the previously reported resistivity and dc susceptibility results. The background subtraction of specific heat has been done by fitting the lattice contribution of specific heat, for the data far away from the transition, to demonstrate the heat capacity jumps, ΔC_{CDW} for all the compounds. The entropy change ΔS_{CDW} across the CDW transition is estimated by integrating $\Delta C_{CDW}/T$ vs T curves depicted in Figure 3.10 along with the temperature dependence of ΔC_{CDW} across the CDW ordering for all the substituted alloys. The parameters obtained from heat capacity data such as specific heat jump ΔC_{CDW} , entropy change associated with the transition ΔS_{CDW} and an excess specific heat ratio $\Delta C_{CDW}/C_{CDW}$ are summarized in the Table 3.4. Here we observe that the amplitude of the specific heat at the CDW transition decreases with the increase in the Ge concentration. Such an effect can be related to the increase in the local defects or atomic disorder with the increase in the substitution concentration. This can be corroborated from the fact that the width of the CDW transition enhances with the substitution concentration.

The parent compound $\text{Lu}_2\text{Ir}_3\text{Si}_5$ (Figure 3.8) shows a massive specific heat jump of almost 45 J/mol K around 207 K within a very narrow temperature region $\Delta T_{CDW}/T_{CDW} \sim 1.5\%$ near its CDW transition, along with a huge entropy change that signifies it to be the first order transition, similar to that observed in $\text{R}_5\text{Ir}_4\text{Si}_{10}$ [79]. Furthermore, it is worthwhile to mention a pronounced thermal hysteresis in $\text{Lu}_2\text{Ir}_3\text{Si}_5$ between the warm up and cooling down scans in resistivity, magnetic susceptibility, heat capacity, thermal conductivity and

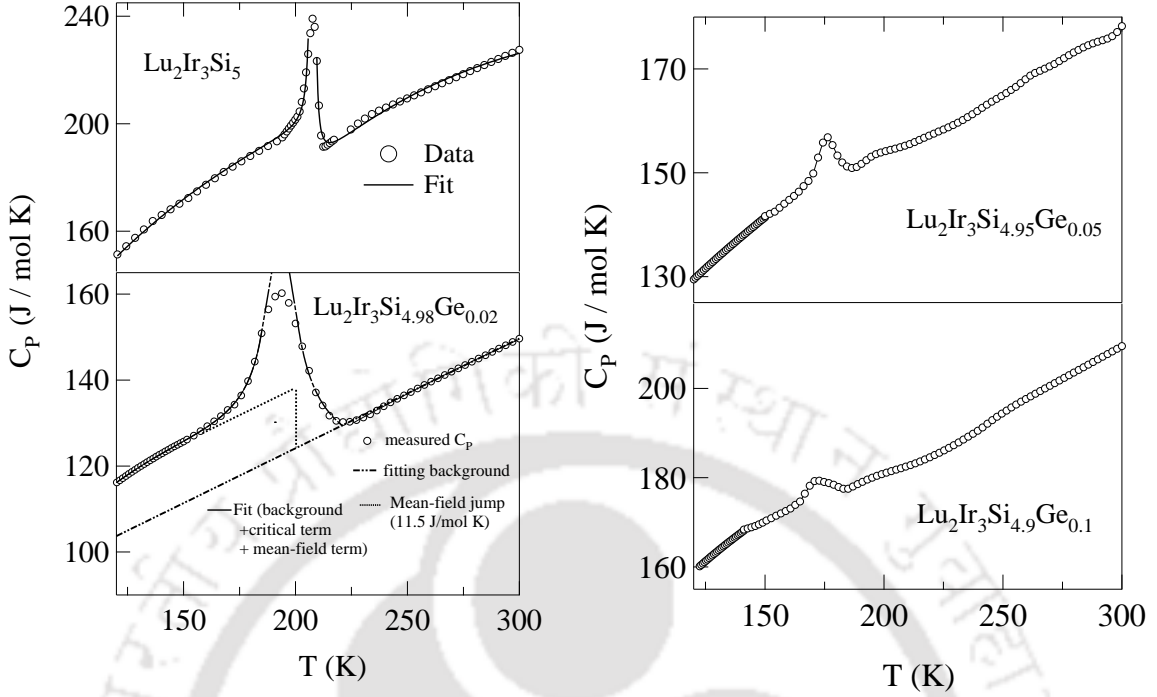


Figure 3.8: The temperature dependence of the specific heat for $\text{Lu}_2\text{Ir}_3(\text{Si}_{1-x}\text{Ge}_x)_5$ ($x = 0.00, 0.004, 0.01$ and 0.02). The main panels demonstrates the data from 120 to 300 K. The fit to model is shown in upper two panels by a continuous line. In second panel, the step change in specific heat is shown clearly.

Seebeck coefficient [19, 70], a characteristic feature expected in a first order transition. In this regard $\text{Lu}_2\text{Ir}_3\text{Si}_5$ has many interesting properties that deviate from the standard weakly coupled CDW behavior and shows signatures of a strongly coupled system.

The specific heat data of $\text{Lu}_2\text{Ir}_3(\text{Si}_{1-x}\text{Ge}_x)_5$ near the CDW transition is analyzed with a model of critical fluctuations in addition to the BCS mean field contributions which has been proposed by Kuo *et al.*, for the $\text{R}_5\text{Ir}_4\text{Si}_{10}$ system [80]. According to the proposed model, the specific heat C consists of three terms as in the following,

$$C = C_L + C_{MF} + C_{fl}, \quad (3.6)$$

where C_L is the lattice background, C_{MF} is the mean-field term below T_{CDW} , and C_{fl} is associated with the fluctuation contributions. At the temperatures under consideration i.e 150 to 300 K, the lattice term can be assumed to take the form as given by Einstein's

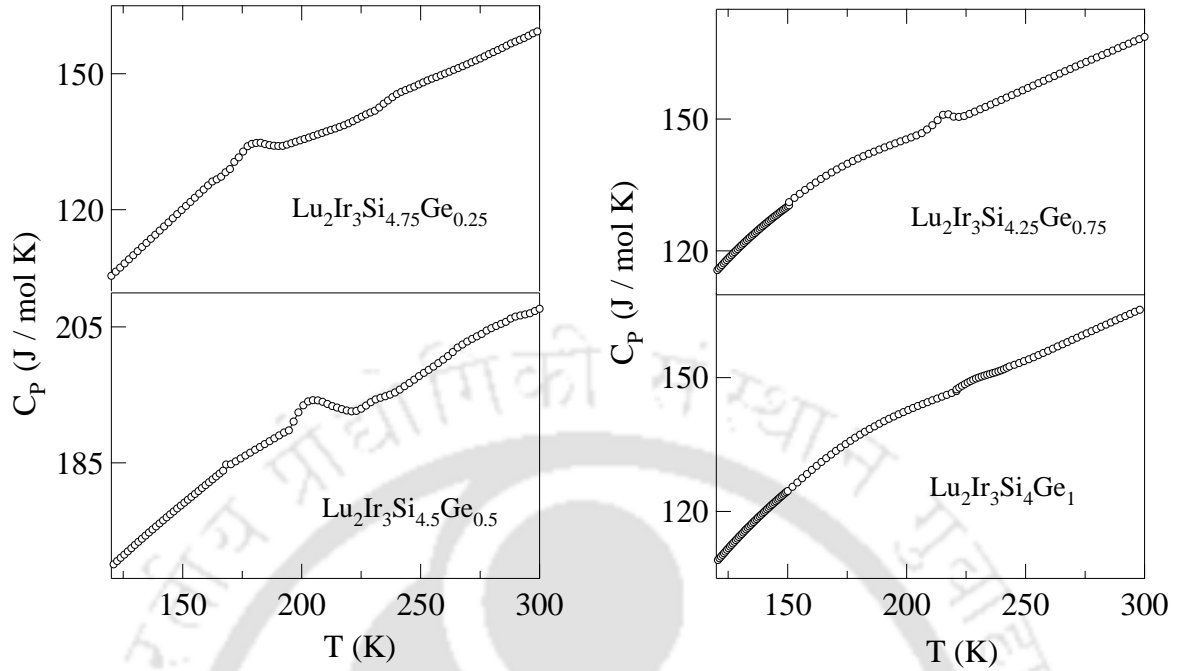


Figure 3.9: The temperature dependence of the specific heat for $\text{Lu}_2\text{Ir}_3(\text{Si}_{1-x}\text{Ge}_x)_5$ ($x = 0.05, 0.1, 0.15$ and 0.2) from 120 to 300 K. The peak is the signature of the CDW transition.

model,

$$C_L = a_1 \left(\frac{a_2}{T} \right)^{a_3} \frac{e^{a_1/T}}{(e^{a_1/T} - 1)^2} \quad (3.7)$$

The mean field term below T_{CDW} is represented by

$$C_{MF} = \gamma^* T_{CDW} (1 + \beta t) \quad (3.8)$$

where γ^* is the effective electronic specific heat coefficient and $t = (T_{CDW} - T)/T_{CDW}$ is the reduced temperature.

The critical fluctuation contribution to the heat capacity has been given by

$$C_{fl}^- = b^- |t|^{-\alpha^-}, \quad T < T_{CDW}$$

$$C_{fl}^+ = b^+ |t|^{-\alpha^+}, \quad T > T_{CDW}, \quad (3.9)$$

Thus, to fit the total heat capacity below and above T_{CDW} , the fitting functional term can be expressed as,

$$C^- = C_L + \gamma^* T_{CDW} (1 + \beta t) + b^- |t|^{-\alpha^-}, \quad T < T_{CDW},$$

$$C^+ = C_L + b^+ |t|^{-\alpha^+}, \quad T > T_{CDW}, \quad (3.10)$$

Here, $a_1, a_2, a_3, \gamma^*, \beta, b^-,$ and b^+ are the effective fitting parameters; α^+ and α^- are called the critical exponents. The range of temperature fluctuation is significant in our data which is about 5 K (ΔT_G). The fitting procedure proposed by Kuo *et.al.*, is as follows: First set the value of CDW transition temperature T_{CDW} , and then use the specific heat data above and away T_{CDW} to find the best fitting values of a_1, a_2 and a_3 in C_L . With the obtained C_L , the optimum values of γ^* and β can be found by fitting the curve for specific heat below and near, but not too close to T_{CDW} to the function of $C_L + C_{MF}$ afterwards determined the best fitting values of b^-, α^- and b^+, α^+ by adjusting the functions $(C_L + C_{MF} + C_{\beta})$ and $(C_L + C_{MF})$ for temperatures below and above T_{CDW} , respectively, to match the measured specific heat curve. Following the procedure, we have fitted the heat capacity data for the samples $\text{Lu}_2\text{Ir}_3(\text{Si}_{1-x}\text{Ge}_x)_5$ with $x = 0.00, 0.004, 0.01, 0.02, 0.05, 0.1, 0.15$ and 0.2 . The left two panels of Figure 3.8 demonstrate the fitted and the actual data of $\text{Lu}_2\text{Ir}_3\text{Si}_5$ and $\text{Lu}_2\text{Ir}_3\text{Si}_{4.98}\text{Ge}_{0.02}$, which show a satisfactory agreement. As we have illustrated by dashed line in $\text{Lu}_2\text{Ir}_3\text{Si}_{4.98}\text{Ge}_{0.02}$, Figure 3.8, the mean-field estimate is made by extrapolating the nearly linear specific heat curve for temperatures far from t in to phase transition temperature. There is clearly an excess of specific heat above this straight line approximation. This excess specific heat is due to fluctuation effects in the vicinity of CDW phase transition.

According to mean-field and asymptotic critical calculation, the values of α^+ and α^- is found to be equal if there should be symmetry in specific heat curve about T_{CDW} . For 3D fluctuation the value of $\alpha = 0.5$, which can be described by the Gaussian approximation, a lower-order extension of mean-field theory [81]. In this section, we analyze the critical behavior of these results and then compare with theoretical predications for the behaviour of CDW systems. The values of the extracted fitting parameters for all the samples are listed in Table 3.5, providing important information about the transitions. It can be seen that the critical exponents α^- and α^+ extracted from the fit for $\text{Lu}_2\text{Ir}_3\text{Si}_5$ are close to 2, much larger than the value $\alpha = 0.5$. The parent compound shows a higher power of

divergence in C_P near T_{CDW} which reflects the very narrow transition width [80]. Upon doping, the transition curve becomes broadened with lower power of divergence in C_P . In spite the specific heat data show disorder or inhomogeneity induced broadening for higher Ge concentration, the C_P is discontinuous at T_{CDW} , which are shown by the solid line in the second panel of Figure 3.8. It is also to be noted that the value of critical exponents reduce progressively until they reach a value of about 0.4 for the compound $\text{Lu}_2\text{Ir}_3\text{Si}_4\text{Ge}_1$.

We also obtained another important quantity γ^* from the fit where γ^*T_{CDW} represents the electronic specific heat jump of the mean-field term near the 3D ordering temperature. The predicted mean field value of the specific heat jump is $\Delta C_{CDW} = 12.8 \text{ J/mol K}$ for $\text{Lu}_2\text{Ir}_3\text{Si}_5$ which is much smaller than the observed value $\Delta C_{CDW} = 45 \text{ J/mol K}$. The value of electronic specific heat γ^* for $\text{Lu}_2\text{Ir}_3\text{Si}_5$ is about $6.2 \times 10^{-2} \text{ J/mol K}^2$ and the bare Sommerfeld's constant $\gamma = 7.5 \times 10^{-3}$. It gives a unit ratio of $\gamma^*/\gamma = 8.3$ which is about 5.7 times larger than the BCS weak-coupling limit value 1.43, indicating the strong coupling nature of the CDW transition. Such enhancements in the specific heat jump from their mean field value have been reported in other CDW systems [80, 82, 83].

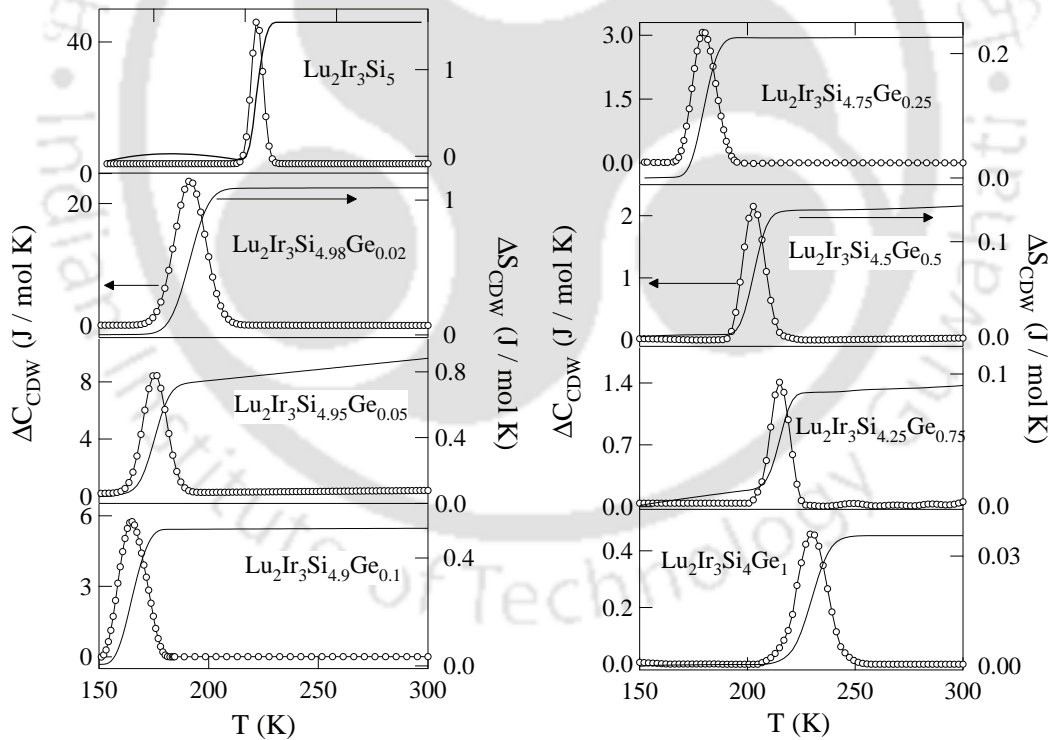


Figure 3.10: The temperature dependence of the ΔC_{CDW} and ΔS_{CDW} across CDW-ordering transitions for $\text{Lu}_2\text{Ir}_3(\text{Si}_{1-x}\text{Ge}_x)_5$ ($x = 0.00, 0.004, 0.01, 0.02, 0.05, 0.1, 0.15$ and 0.2).

The CDW coherence length, ξ_0 of a value about 5.4 \AA which can be deduced for

$\text{Lu}_2\text{Ir}_3\text{Si}_5$ by using the Ginzburg criteria $\Delta T_G = (T_{CDW}/32) (k_B/\pi\Delta C_{CDW}\xi_0^3)^2$. $\Delta T_G = 5$ K is the temperature region where the fluctuations are important. According to McMillan's model proposed for strong CDW systems, the deduced short coherence length is an indication of strong interchain coupling in $\text{Lu}_2\text{Ir}_3\text{Si}_5$. In addition, it was reported that a large number of soft phonon modes in the transition region contribute substantially to the heat capacity. The larger value of γ^*T_{CDW} corroborates the above inference by an assumption of the larger portion of Fermi surface nesting in the studied compound, as compared to other CDW compounds. It explains the origin of huge specific heat jumps displayed in the Si compound. Similar results have been reported for other CDW materials such as 4.5 Å for 2H-TaSe₂ [81], 4.6 Å for K_{0.3}MoO₃ [84] and 5 Å for Lu₅Ir₄Si₁₀ [80]. The values of γ^*/γ and γ^*T_{CDW} decrease and saturate close to the mean field value for Ge substituted alloys compared to the undoped Si compound. Moreover, the evolution of critical exponents also suggests that the CDW transition is non-mean-field-like in the pure compound $\text{Lu}_2\text{Ir}_3\text{Si}_5$, but changes to a mean-field-like transition, which may be induced by disorder effects.

Ge	Lattice term		Mean-field term			Fluctuation term			
	a_1 (J/mol K)	a_2 (K)	a_3	γ^* (J/mol K ²)	β	b^- (J/mol K)	α^-	b^+ (J/mol K)	α^+
0.00	173	167	1.45	0.062	6.01	0.009	1.8	0.003	1.72
0.02	127	139	1.71	0.029	4.05	0.54	1.13	1.57	1.06
0.05	129	134	1.56	0.021	6.57	0.21	0.93	1.06	0.92
0.1	131	105	1.67	0.009	7.3	0.20	0.81	0.56	0.75
0.25	133	128	1.75	0.018	4.07	1.18	0.37	1.18	0.36
0.5	122	88	1.65	0.023	0.55	1.46	0.40	3.76	0.37
0.75	121	119	1.72	0.028	1.8	0.75	0.38	0.69	0.44
1	64	46	1.56	0.029	1.48	0.60	0.42	0.08	0.37

Table 3.5: The fitting parameters extracted from the specific heat data of $\text{Lu}_2\text{Ir}_3(\text{Si}_{1-x}\text{Ge}_x)_5$ using the model of critical fluctuations and mean-field contributions.

3.3.2 $\text{Lu}_2(\text{Ir}_{1-x}\text{Rh}_x)_3\text{Si}_5$

3.3.2.1 X-ray diffraction studies

The powder x-ray diffraction data for all the doped samples confirmed the single phase with the $\text{U}_2\text{Co}_3\text{Si}_5$ type structure (*Ibam*). The Rietveld analysis of the observed

XRD pattern for all the compounds was done using the FULLPROF program and the estimated lattice parameters a , b and c are presented in the Table 3.6. The lattice parameters and the unit cell volume decreases with the increase of Rh concentration as shown in Figure 3.11. We have confirmed the stoichiometry of the compounds $\text{Lu}_2(\text{Ir}_{1-x}\text{Rh}_x)_3\text{Si}_5$ for all the values of x using the EPMA. Here also, we could notice the contrast difference in EPMA image, but the homogeneity in the ratio of the constituent elements for the samples is maintained at those different locations.

x	a (Å)	b (Å)	c (Å)	v (Å ³)	c/a
0.00	9.915	11.287	5.722	640.298	0.577
0.01	9.881	11.264	5.709	635.337	0.578
0.03	9.760	11.251	5.661	621.655	0.580
0.1	9.711	11.173	5.652	613.269	0.582
0.2	9.666	11.171	5.645	609.547	0.584
0.3	9.561	11.161	5.622	599.932	0.588

Table 3.6: Lattice parameters of $\text{Lu}_2(\text{Ir}_{1-x}\text{Rh}_x)_3\text{Si}_5$.

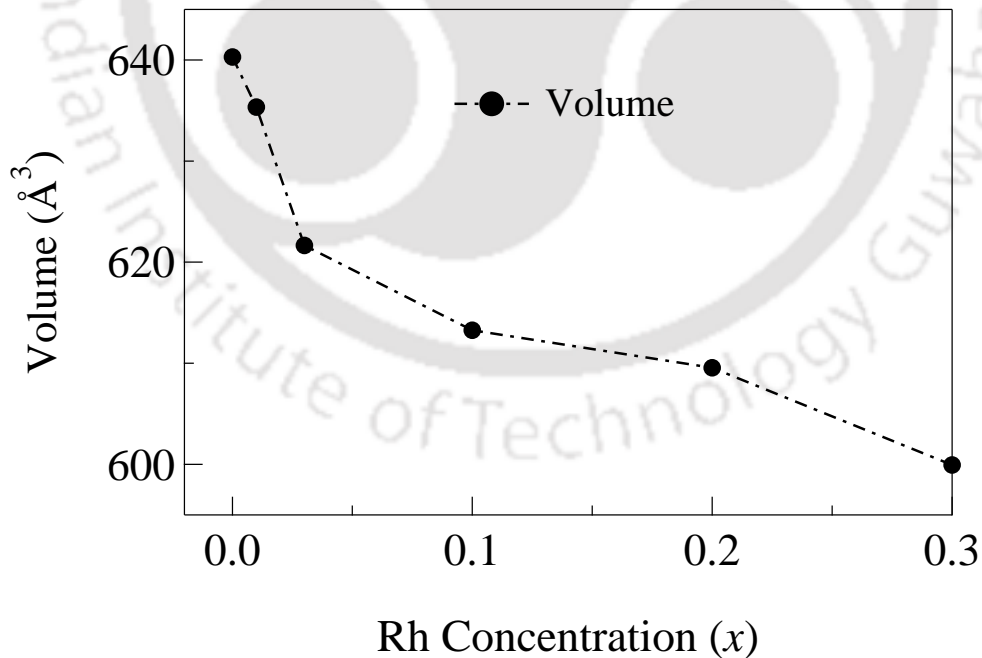


Figure 3.11: Rh concentration (x) dependence of the volume for $\text{Lu}_2(\text{Ir}_{1-x}\text{Rh}_x)_3\text{Si}_5$ for $x = 0.00, 0.01, 0.03, 0.1, 0.2$ and 0.3 .

3.3.2.2 Magnetic susceptibility studies

Figure 3.12 depicts dc magnetic susceptibility of $\text{Lu}_2(\text{Ir}_{1-x}\text{Rh}_x)_3\text{Si}_5$ for various Rh concentrations ($x = 0.00 - 0.3$) as a function of temperature. The left panels display low

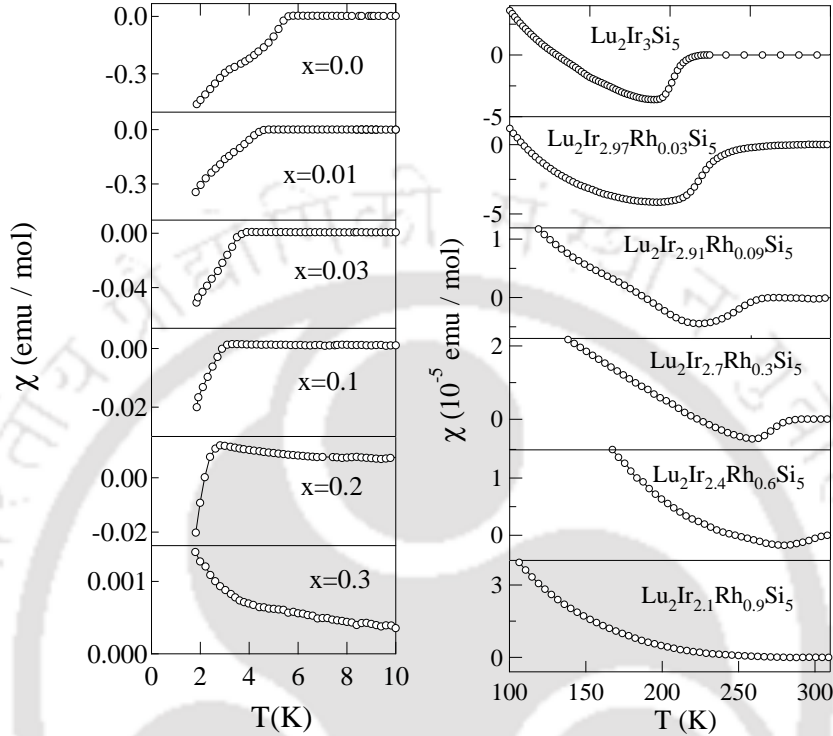


Figure 3.12: The temperature dependence of the dc susceptibility for the samples of $\text{Lu}_2(\text{Ir}_{1-x}\text{Rh}_x)_3\text{Si}_5$ ($x = 0.00, 0.01, 0.03, 0.1, 0.2$ and 0.3). The left panel shows the dc susceptibility data from 2 to 10 K and the right panels show the data from 100 to 300 K.

temperature susceptibility data in the field of 10 Oe, exhibiting the diamagnetism due to the superconducting transition for different compositions, characteristics of a superconductivity similar to $\text{Lu}_2\text{Ir}_3(\text{Si}_{1-x}\text{Ge}_x)_5$. The signature of the diamagnetic drop across the CDW transition as the sample is cooled to the CDW state is shown in the right panels of Figure 3.12 under an applied field of 5 T. This feature is due to the appearance of the partial gap at the Fermi surface and hence reduces electronic density of states. As can be seen from the figure, the CDW transition temperature shifts towards higher temperatures, further the CDW transition also begins to smear out and broadens considerably as we increase the Rh concentration in the alloy. For 30 % Rh concentration and above ($x > 0.3$, not shown here), the CDW is not noticed and most probably not detected by these global measurements. The value of T_{CDW} is determined from the peaks observed in the derivative plots ($d\chi/dT$ vs T).

Furthermore, it is interesting to note that the systematic decrease in the superconducting transition temperature T_{SC} upon Rh doping in the alloy system, as can be seen in the left-panels of Figure 3.12, and it goes below 1.8 K for $x = 0.3$. This is in the opposite sense to that of T_{CDW} . We could conclude that both CDW and SC are not noticeable for $x = 30\%$ and above. Thus, it has been shown that the study of $\text{Lu}_2(\text{Ir}_{1-x}\text{Rh}_x)_3\text{Si}_5$ provides a very convincing evidence that the CDW and the SC are competing for the same Fermi surface.

3.3.2.3 Resistivity studies

The normalized electrical resistivity *vs* temperature of $\text{Lu}_2(\text{Ir}_{1-x}\text{Rh}_x)_3\text{Si}_5$ for $x = 0.00 - 0.3$ are presented in Figure 3.13. The superconducting transition T_{SC} can clearly be observed by a sharp drop in the low temperature resistivity data, shown in the left panel of the figure. But the transition is not complete even down to 1.8 K, a result that may be related to the nonuniformity of the EPMA image. The right panel displays an abrupt increase in resistivity at the higher temperature region, which represents the onset of the CDW state. This presence of the metal-insulator transition occurs as a result of the partial gap at the Fermi level associated with the CDW transition. The onset and development of CDW instabilities in $\text{Lu}_2(\text{Ir}_{1-x}\text{Rh}_x)_3\text{Si}_5$ are very well tracked by resistivity measurements. These data show that both CDW and SC are present in $\text{Lu}_2(\text{Ir}_{1-x}\text{Rh}_x)_3\text{Si}_5$ at least up to 30% of Rh substitution which corroborates the susceptibility data and hence suggest that there is a competition between CDW and SC in these compounds..

x	T_{CDW} (K)	$\frac{\Delta\rho}{\rho(300K)}$ (%)	$\frac{\Delta T_{CDW}}{T_{CDW}}$ (%)	T_C (K)
0.00	202	22	14	5.5
0.01	220	13	17	4.6
0.03	233	24	15	3.8
0.1	262	12	19	3.1
0.2	283	4	16	2.5
0.3	no CDW	-	-	no SC

Table 3.7: CDW transition parameters obtained from the temperature dependence of the resistivity data of $\text{Lu}_2(\text{Ir}_{1-x}\text{Rh}_x)_3\text{Si}_5$.

Thus, the SC and CDW compete for the same density of states at the Fermi surface and in turn they suppress each other. The value of the T_{CDW} has been determined from the peak position in the derivative plots of the resistivity data for various values of x . The resistivity enhancement $\Delta\rho/\rho$, sharpness of the transition $\Delta T_{CDW}/T_{CDW}$, T_{SC} and T_{CDW} are listed in Table 3.7. From the table, one can notice that as the CDW transition shifts to higher temperatures from 202 to 283 K the SC decreases to lower temperatures (5.5 to 2.5 K), as x increases from 0 to 0.2. The sharpness of the the SC transition gets smeared out at higher Rh concentration. These observations indicate that the increase in T_{CDW} along with the suppression of T_{SC} with Rh concentration may be due to the effect of charge-carrier densities. The above inference corroborates the dc susceptibility results. We will return to this point later in the discussion part.

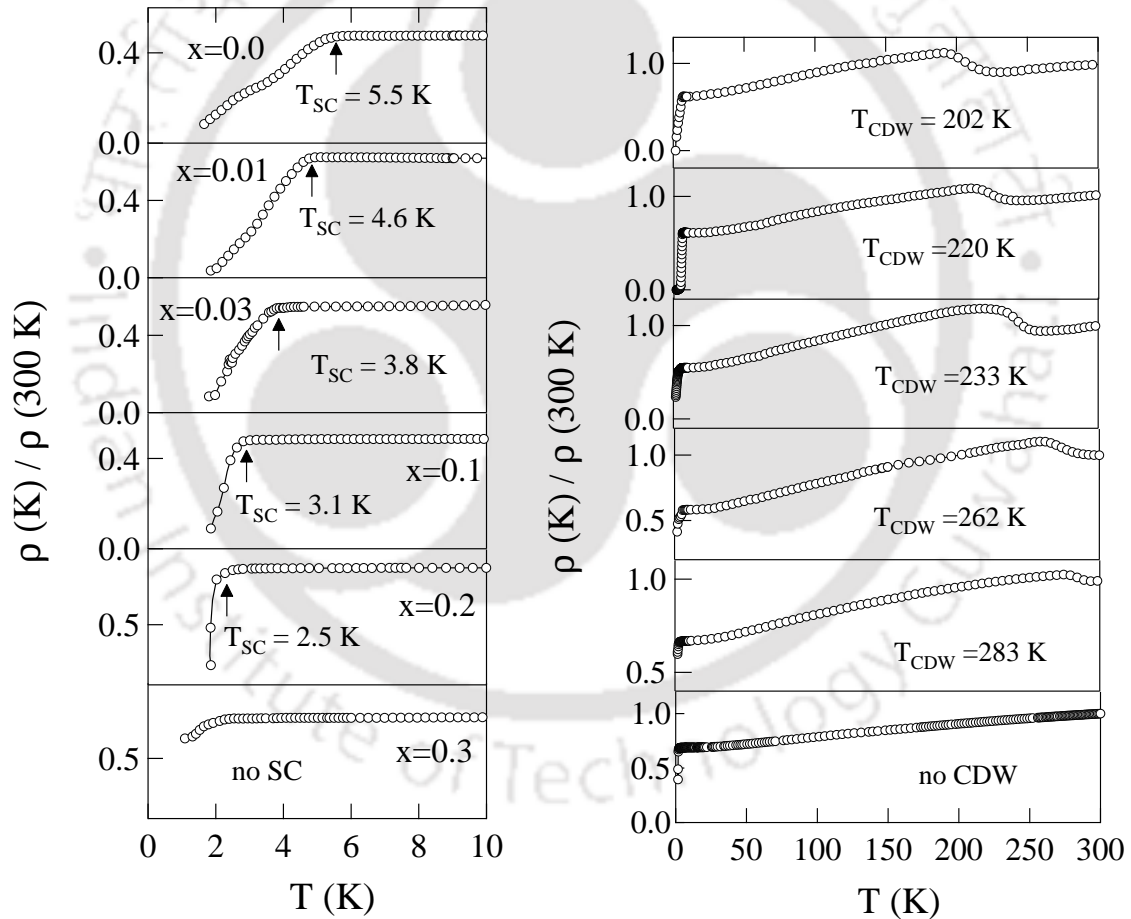


Figure 3.13: The temperature dependence of the electrical resistivity for $\text{Lu}_2(\text{Ir}_{1-x}\text{Rh}_x)_3\text{Si}_5$ ($x = 0.00, 0.01, 0.03, 0.1, 0.2$ and 0.3). The left panel shows the resistivity data between 1.8 to 10 K indicating the SC transition. The right panel shows the data from 1.8 K till 300 K highlighting the CDW transition.

3.3.2.4 Heat-capacity studies

The heat capacity data for $\text{Lu}_2(\text{Ir}_{1-x}\text{Rh}_x)_3\text{Si}_5$ are fitted above the superconducting transition by using Equation 3.1. The enhanced density of states $N^*(E_F)$ and Debye temperature θ_D can be calculated using the Equation 3.2 and Equation 3.3, respectively. Similarly we estimated the value of the electron-phonon coupling parameter and the bare density of states from the Equation 3.4 and Equation 3.5 respectively. The parameters obtained from the fit are listed in Table 3.8. From the table, it is clear that the suppression of T_{SC} is mainly due to the decrease in the electron phonon interaction. Further there is a significant reduction in the density of states at the Fermi levels, $N^*(E_F)$ which may have partially arisen due to atomic disorder.

Figure 3.14 illustrates the heat capacity data for $\text{Lu}_2(\text{Ir}_{1-x}\text{Rh}_x)_3\text{Si}_5$ $x = 0.00, 0.01, 0.03, 0.1, 0.2$ and 0.3 in temperature range from 150 to 320 K highlights CDW ordering. We note that T_{CDW} determined from C_P matches with that of dc susceptibility and resistivity results. Figure 3.15 depicts the temperature dependence of entropy change ΔS_{CDW} and ΔC_{CDW} across the CDW ordering for all the substituted alloys. The values of specific heat jump, ΔC_{CDW} , entropy change, ΔS_{CDW} associated with the CDW transition and $\Delta C_{CDW}/C_{CDW}$ which illustrate the characteristics of specific heat anomaly for these alloys are listed in Table 3.9. It is clearly seen that the excess specific heat $\Delta C_{CDW}/C_{CDW}$ is suppressed by the Rh substitution. The data near the CDW transition were analyzed via a least-square-fitting procedure to a model of critical fluctuations in addition to the BCS mean field contributions, described in the previous section. The solid line in Figure 3.14 shows a fit to Equation 3.10.

x	T_{CDW} (K)	ΔC_{CDW} (J/mol K)	$\frac{\Delta C_{CDW}}{C_{CDW}}$ (%)	ΔS_{CDW} (J/mol K)	ξ_0 (Å)
0.00	207	45	25	1.52	5.4
0.01	228	9.43	7.9	1.06	9.01
0.03	230	6.7	5.2	0.6	10
0.1	267	10	5.7	0.49	8.61
0.2	284	4.4	2.7	0.35	11.16
0.3	-	-	-	-	-

Table 3.9: Parameters obtained from the high temperature specific heat data of $\text{Lu}_2(\text{Ir}_{1-x}\text{Rh}_x)_3\text{Si}_5$.

x	γ (J/mol K^2) $\times 10^{-3}$	Θ_D	$N^*(E_F)$ (states/eV)	λ_{ep}	$N(E_F)$ (states/eV)
0.00	7.5	376	0.17	0.55	0.11
0.01	6.3	310	0.14	0.54	0.084
0.03	5.7	309	0.13	0.52	0.079
0.1	4.6	297	0.10	0.5	0.06
0.2	3.6	309	0.09	0.46	0.054
0.3	-	-	-	-	-

Table 3.8: Parameters obtained from the low temperature specific heat data of $\text{Lu}_2(\text{Ir}_{1-x}\text{Rh}_x)_3\text{Si}_5$.

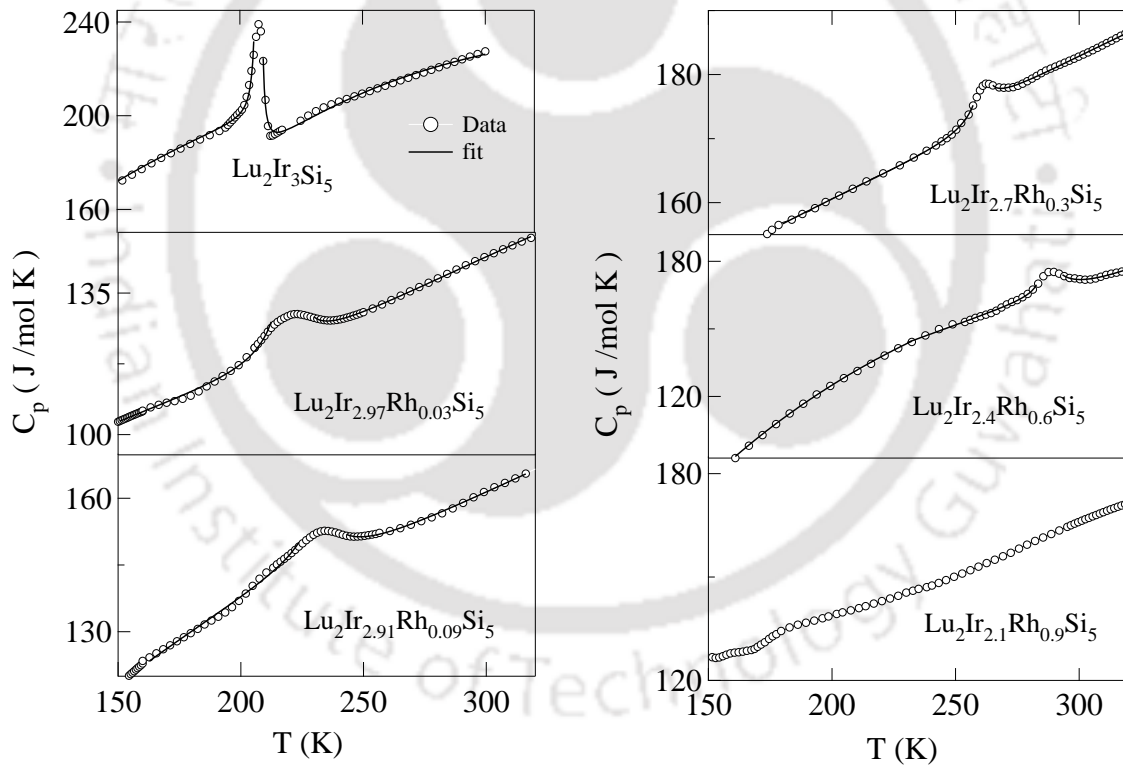


Figure 3.14: Plot of specific heat versus temperature for $\text{Lu}_2(\text{Ir}_{1-x}\text{Rh}_x)_3\text{Si}_5$ ($x = 0.00, 0.01, 0.03, 0.1, 0.2$ and 0.3). The main panels demonstrate the data from 150 to 300 K. The solid line is the fit to the critical fluctuation model (see text).

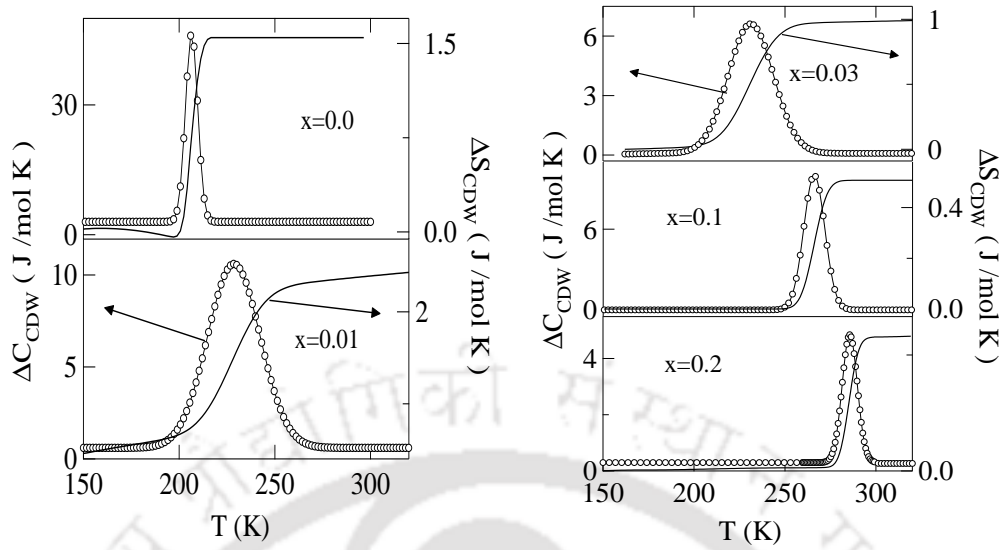


Figure 3.15: Plot of ΔC_{CDW} and ΔS_{CDW} versus temperature across CDW-ordering transitions for $\text{Lu}_2(\text{Ir}_{1-x}\text{Rh}_x)_3\text{Si}_5$ $x = 0.00, 0.01, 0.03, 0.1, \text{ and } 0.2$.

Rh	Lattice term			Mean-field term		Fluctuation term			
	a_1 (J/mol K)	a_2 (K)	a_3	γ^* (J/mol K ²)	β	b^- (J/mol K)	α^-	b^+ (J/mol K)	α^+
0.00	173	167	1.45	0.062	6.01	0.009	1.8	0.003	1.72
0.03	93	113	1.5	0.073	4.9	0.64	0.75	0.82	0.71
0.09	92	108	1.5	0.082	2.4	0.5	0.48	3.5	0.50
0.3	93	80	1.6	0.086	0.86	0.41	0.54	0.34	0.54
0.6	104	139	1.45	0.095	1.14	0.23	0.44	5.3	0.43
0.9	-	-	-	-	-	-	-	-	-

Table 3.10: The fitting parameters extracted from the specific heat data of $\text{Lu}_2(\text{Ir}_{1-x}\text{Rh}_x)_3\text{Si}_5$ using the model of critical fluctuations and mean-field contributions.

The fitting parameters for $\text{Lu}_2(\text{Ir}_{1-x}\text{Rh}_x)_3\text{Si}_5$, using this model are listed in Table 3.10. It is worthwhile to mention that the critical exponents α^+ and α^- extracted from the best fit for these materials reduce progressively from 1.8 (for the undoped compound $\text{Lu}_2\text{Ir}_3\text{Si}_5$) to the value of about 0.4 (the mean field value) as depicted in $\text{Lu}_2\text{Ir}_3(\text{Si}_{1-x}\text{Ge}_x)_5$. The value of the γ^* increases slightly with Rh concentration in the $\text{Lu}_2(\text{Ir}_{1-x}\text{Rh}_x)_3\text{Si}_5$ series in contrast to that of $\text{Lu}_2\text{Ir}_3(\text{Si}_{1-x}\text{Ge}_x)_5$. Besides, coherence lengths, ξ_0 (see Table 3.9) deduced for these materials have relatively large values compared to that of the parent

compound. In this respect, it is important to note that both atomic disorder and chemical pressure play a very crucial role.

3.3.3 $(\text{Lu}_{1-x}\text{Sc}_x)_2\text{Ir}_3\text{Si}_5$

3.3.3.1 X-ray diffraction studies

The powder x-ray diffraction pattern confirms the expected orthorhombic $\text{U}_2\text{Co}_3\text{Si}_5$ type structure without the presence of any of the impurity phase. We have analyzed the data via the Reitveld fitting using the FULLPROF program. The starting parameters for the fitting are taken from the parent $\text{Lu}_2\text{Ir}_3\text{Si}_5$. The estimated lattice constants a , b

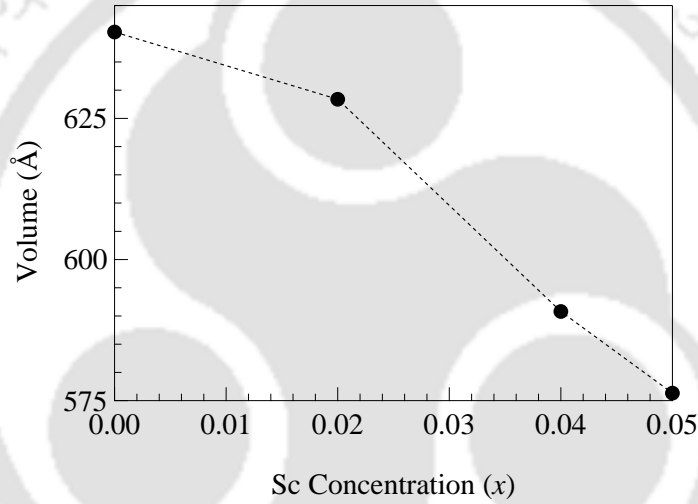


Figure 3.16: Plot of Sc (x) concentration versus volume for the pseudoternary system $(\text{Lu}_{1-x}\text{Sc}_x)_2\text{Ir}_3\text{Si}_5$ $x = 0.00, 0.02, 0.04$ and 0.05 .

x	a (Å)	b (Å)	c (Å)	v (Å ³)	c/a
0.00	9.915	11.287	5.722	640.298	0.577
0.02	9.898	11.167	5.684	628.385	0.574
0.04	9.644	10.831	5.656	590.793	0.586
0.05	9.601	10.801	5.616	582.341	0.585

Table 3.11: Lattice parameters of $(\text{Lu}_{1-x}\text{Sc}_x)_2\text{Ir}_3\text{Si}_5$

and c from the best fit of the data for $(\text{Lu}_{1-x}\text{Sc}_x)_2\text{Ir}_3\text{Si}_5$ ($x=0.00, 0.02, 0.04$ and 0.05) are summarized in the Table 3.11 and plotted in Figure 3.16. It is clear that the unit cell volume and lattice constants decrease progressively as Sc concentration increases in the alloy. Since Sc has a smaller metallic radius, it contracts the lattice chemically, resulting in a non-negligible size effect in the alloying process. We analyzed the homogeneity and purity of the sample using the EDAX and found a qualitative consistency between the taken stoichiometric concentration and the analyzed one.

3.3.3.2 Magnetic susceptibility studies

Figure 3.17 shows the temperature dependence the dc susceptibility for $(\text{Lu}_{1-x}\text{Sc}_x)_2\text{Ir}_3\text{Si}_5$ ($x=0.02, 0.04$ and 0.05). The left panel shows χ vs T in the temperature range from 1.8 to 10 K under a magnetic field of 10 Oe in the ZFC state which clearly displays diamagnetic signals, indicating the superconducting transition. The superconducting transition

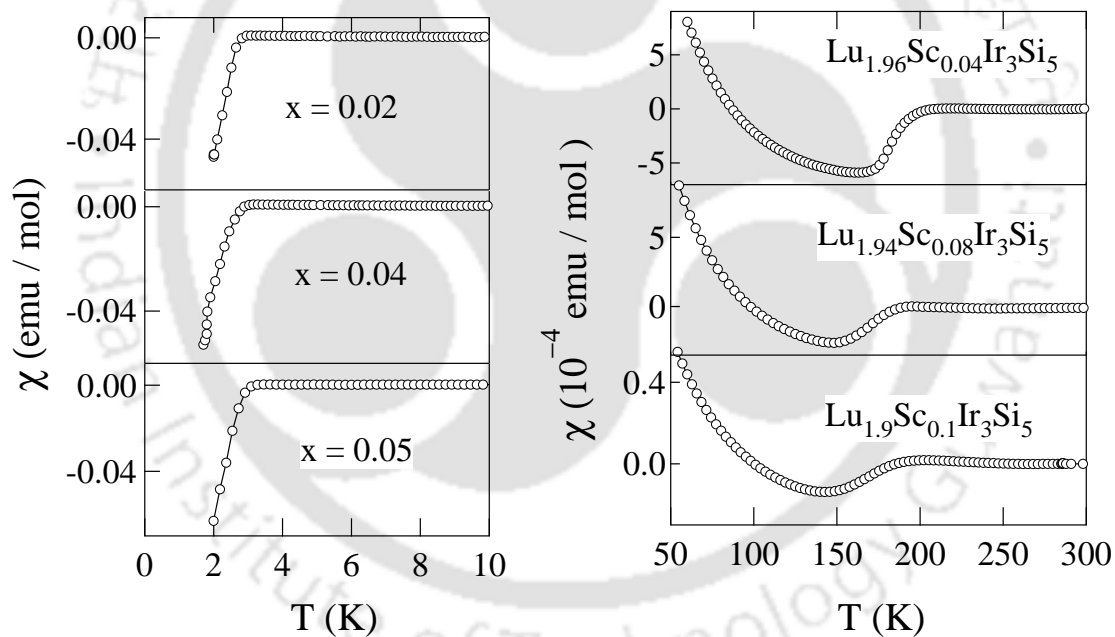


Figure 3.17: Plot of the temperature dependence of the dc susceptibility of $(\text{Lu}_{1-x}\text{Sc}_x)_2\text{Ir}_3\text{Si}_5$ ($x = 0.02, 0.04$ and 0.05). The left panel demonstrates dc susceptibility data from 2 to 10 K and the right panel show the data from 50 K till 300 K.

temperature in all the Sc substituted alloys are observed to occur around 3.5 K. This is close to the value of T_{SC} reported by Singh *et. al.*, in the parent compound, $\text{Lu}_2\text{Ir}_3\text{Si}_5$ [19]. The CDW transition is observed in the right panel of the Figure 3.17 which is a plot of

the dc susceptibility in the temperature range between 50 to 300 K at an applied field of 5 T.

The data exhibit a diamagnetic drop below T_{CDW} , thereby signifying the opening of a gap at the Fermi surface. The rise in χ at low temperatures is due to the influence of magnetic impurities at the ppm (parts per million) level in Lu. As we can see from the graph, T_{CDW} decreases with the increase in Sc concentration. For the sample with $x = 0.02$, the CDW anomaly is almost identical to that of $x = 0$. With the further increase in x , the CDW transition widens. However, the superconducting transition does not change in a complementary manner. The onset is at 3.2 K for all the Sc doped alloys (till 5 % of Sc) and is not perturbed even by substitutional disorder. It is worthwhile to note that the substitution of Sc in the alloy suppresses the CDW transition without disturbing superconducting ordering till 5 % of the Sc concentration. We avoided reporting of the compounds with large amount Sc concentration as they do not preserve the $\text{Lu}_2\text{Ir}_3\text{Si}_5$ crystal structure.

3.3.3.3 Resistivity studies

Figure 3.18 shows the normalized electrical resistivity as a function of temperature for the pseudoternary systems $(\text{Lu}_{1-x}\text{Sc}_x)_2\text{Ir}_3\text{Si}_5$ for $x = 0.02, 0.04$ and 0.05 . Superconducting transitions are highlighted in the left panel of the figure. Again, the resistivity drop at low temperature is not complete down to 1.8 K, like all other pseudo ternary compounds of $\text{Lu}_2\text{Ir}_3\text{Si}_5$. The sharp step like anomaly in the resistivity measurement at high temperature reveals the CDW transition (right panel of Figure 3.18).

x	T_{CDW} (K)	$\frac{(\Delta\rho)}{\rho(300K)}$ (%)	$\frac{\Delta T_{CDW}}{T_{CDW}}$ (%)	T_C (K)
0.02	182	24	10	2.8
0.04	174	20	10	3.1
0.05	163	19	9.8	3.2

Table 3.12: Parameters obtained from the temperature dependence of the resistivity of $(\text{Lu}_{1-x}\text{Sc}_x)_2\text{Ir}_3\text{Si}_5$ near the CDW region.

With the increase of the Sc concentration in $(\text{Lu}_{1-x}\text{Sc}_x)_2\text{Ir}_3\text{Si}_5$, T_{CDW} decreases,

whereas T_{SC} remains unchanged at 3.2 K for all compounds. The Sc concentration dependence of the CDW temperature T_{CDW} and the superconducting transition T_{SC} [derived from the resistivity derivative plot ($d\rho/dT$)], the amplitude of the resistivity anomaly ($\Delta\rho/\rho$) and sharpness of the transition ($\Delta T_{CDW}/T_{CDW}$) are listed in Table 3.12. It can be conjectured that the impurities lower the T_{CDW} , smear out the CDW transition, but do not affect the T_{SC} . These results are consistent with the susceptibility data and we could conclude that the substitution of Sc not only causes chemical pressure, but induces an atomic disorder.

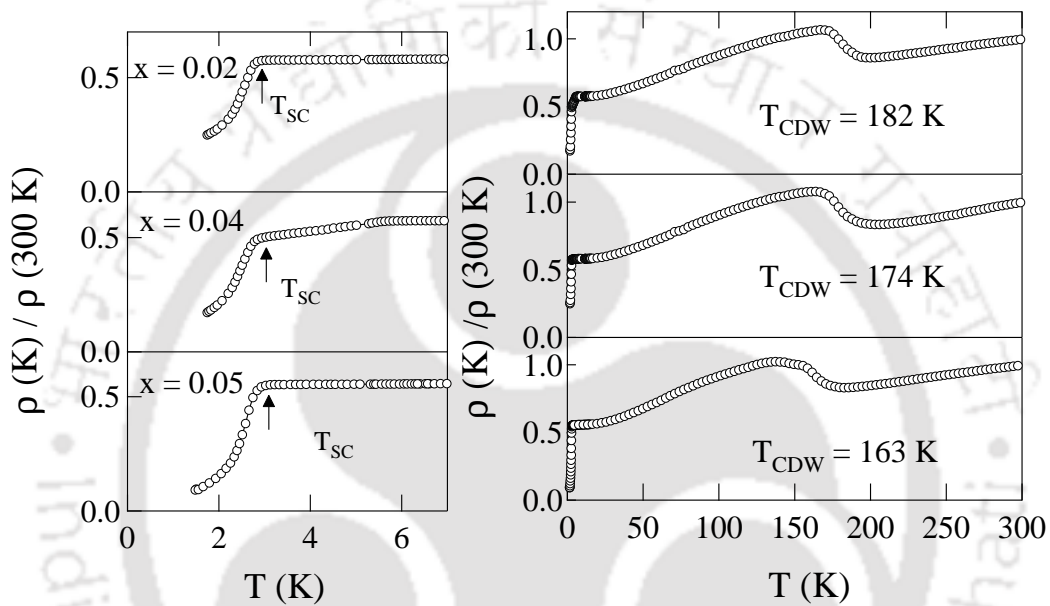


Figure 3.18: The temperature dependence of the electrical resistivity for $(\text{Lu}_{1-x}\text{Sc}_x)_2\text{Ir}_3\text{Si}_5$ ($x = 0.02, 0.04$ and 0.05). The left panel shows the resistivity data between 1.8 to 10 K indicating the SC transition. The right panel shows the data from 1.8 K till 300 K highlighting the CDW transition.

3.3.3.4 Heat capacity studies

The temperature dependence of the heat capacity data for the substituted alloy $(\text{Lu}_{1-x}\text{Sc}_x)_2\text{Ir}_3\text{Si}_5$ ($x = 0.02, 0.04$ and 0.05) are presented in Figure 3.19(a). We note that the T_{CDW} observed in this measurement is consistent with the previously reported value obtained from χ and ρ results. The specific heat parameters for the CDW transition such as the heat capacity jump, ΔC_{CDW} , the entropy change, ΔS_{CDW} and the excess specific heat jump, $\Delta C_{CDW}/C_{CDW}$ is summarized in Table 3.13. The corresponding plots are displayed in Figure 3.19(b).

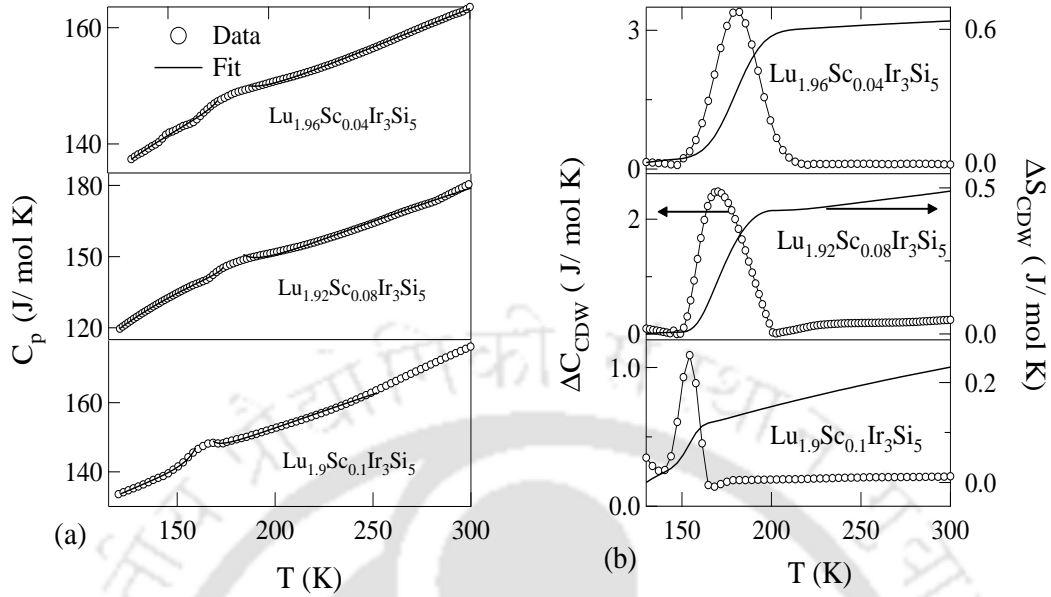


Figure 3.19: (a) The temperature dependence of the specific heat for $(\text{Lu}_{1-x}\text{Sc}_x)_2\text{Ir}_3\text{Si}_5$ ($x = 0.02, 0.04$ and 0.05). The main panels demonstrate the data from 120 to 300 K. The solid line is the fit to the critical fluctuation model (see text). (b) Plot of ΔC_{CDW} and ΔS_{CDW} versus temperature across CDW-ordering transitions for $(\text{Lu}_{1-x}\text{Sc}_x)_2\text{Ir}_3\text{Si}_5$ ($x = 0.02, 0.04$ and 0.05).

x	T_{CDW} (K)	ΔC_{CDW} (J/mol K)	$\frac{\Delta C_{CDW}}{C_{CDW}}$ (%)	ΔS_{CDW} (J/mol K)
0.02	182	3.4	2.3	0.6
0.04	174	2.3	1.6	0.42
0.05	163	0.9	0.63	0.12

Table 3.13: Parameters obtained from the specific heat data of $(\text{Lu}_{1-x}\text{Sc}_x)_2\text{Ir}_3\text{Si}_5$ near the CDW region.

It is very clear that excess specific heat $\Delta C_{CDW}/C_{CDW}$ at T_{CDW} is suppressed and the transition width is broadened by the Sc substitution, just as one would anticipate in this system. To further explore the CDW transition in $(\text{Lu}_{1-x}\text{Sc}_x)_2\text{Ir}_3\text{Si}_5$, the specific heat data between the range over 120 to 300 K are analyzed in accordance with the critical-

fluctuation model proposed by Kuo *et al.*, (see above Sec. 3.3.1.4). The solid line in Figure 3.19(a) is a fit to this model. The extracted fitting parameters for each compound are given in Table 3.14. It turns out that the critical exponents α^+ and α^- are close to 0.5 which indicates that a BCS mean field like transition occurs as the system is doped. We observed this trend for all other pseudo ternary compounds presented in the above sections. This indicates that the chemical pressure relates to the changes in the electronic configuration.

Sc	Lattice term			Mean-field term		Fluctuation term			
	a_1 (J/molK)	a_2 (K)	a_3	γ^* (J/molK ²)	β	b^- (J/molK)	α^-	b^+ (J/molK)	α^+
0.02	112	103	1.6	0.042	2.7	0.54	0.51	1.17	0.48
0.04	165	180	1.8	0.023	0.5	0.39	0.45	5.01	0.44
0.05	117	101	1.8	0.009	1.23	1.42	0.47	1.17	0.49

Table 3.14: The fitting parameters extracted from the specific heat data of $(\text{Lu}_{1-x}\text{Sc}_x)_2\text{Ir}_3\text{Si}_5$ using a model of critical fluctuations and mean-field contributions near CDW region.

3.4 Discussion

In this section we will discuss the interplay between superconductivity and charge density wave ordering exhibited in substituted compounds of $\text{Lu}_2\text{Ir}_3\text{Si}_5$. As a part of that the temperature-concentration (T - x) phase diagram has been constructed by combining the results derived from transport, magnetic and thermal measurements for all the samples in the alloy system, displayed in Figure 3.20, Figure 3.21 and Figure 3.22.

With the increase of Ge concentration, T_{CDW} shows a non-monotonic behavior, in contrast to the $\text{Lu}_5\text{Ir}_4(\text{Si}_{1-x}\text{Ge}_x)_{10}$ system where it behaves in a quasi-linear manner. In our study, we find that Ge substitution lowers the T_{CDW} , broadens and smears the CDW transition, while increasing the T_{SC} superconducting transition for low Ge impurity concentration ($x \leq 0.02$), as one would expect in this system. However, for higher Ge concentration, we could observe that the T_{SC} reduces along with the enhancement of T_{CDW} until $x=0.2$. This strongly indicates that the SC in the system competes with the CDW ordering. We determine the initial concentration dependence (for small x) of T_{CDW} and T_{SC} to be $(dT_{CDW}/dx)=23.72 (\pm 0.7)$ K/at.% and $(dT_{SC}/dx)=1.85(\pm 0.07)$ K/at.%.

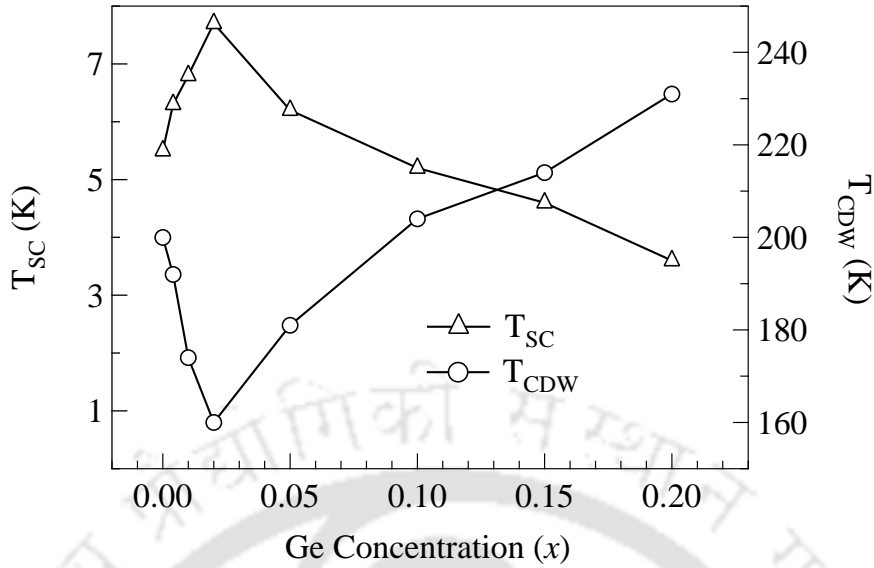


Figure 3.20: Plot of T_{CDW} and T_{SC} vs Ge concentration (x) for $\text{Lu}_2\text{Ir}_3(\text{Si}_{1-x}\text{Ge}_x)_5$ ($x = 0.00, 0.004, 0.01, 0.02, 0.05, 0.1, 0.15$ and 0.2).

Also, we note that the CDW system is suppressed even though there is an expansion of the lattice volume. In addition, the suppression of the T_{SC} and the enhancement of the T_{CDW} in certain compounds are related to the increase in density of states in its narrow d -band, for which the resistive anomaly due to the CDW transition shows a sudden increase upon doping (Table. II). The same phenomena may be responsible in our case, but it is a definite example of the system being beyond mean field theory. A definite conclusion for such a scenario needs further experimental support, such as the optical spectroscopy study to give a rigorous explanation about this unusual non-monotonic behavior seen in the temperature-concentration phase diagram of $\text{Lu}_2\text{Ir}_3(\text{Si}_{1-x}\text{Ge}_x)_5$. From this observation, one would conclude that the effects of ionic size plays an important role for the CDW transition in this class of materials.

More interestingly, we monitored that both CDW and SC are still present until 20 % of the Ge substitution in the alloy system, a robust behavior of CDW and superconductivity in these compounds. This is seemingly contradictory to the case of $\text{Lu}_5\text{Ir}_4(\text{Si}_{1-x}\text{Ge}_x)_{10}$, for which the CDW anomaly completely disappears at $x = 10$ % and in fact attains a maximum value of $T_{SC} = 6.6$ K for a 20 % Ge substitution [18]. Afterwards the T_{SC} reduces until it reaches a value of 2.4 K for the pure Ge sample. But in the 2-3-5 system, a high pressure study on this alloy is needed to find the complete suppression of CDW and SC ordering.

It will be interesting to understand the electronic density of states near the Fermi level in $\text{Lu}_2\text{Ir}_3\text{Si}_5$ by Rh impurity doping on Ir site, $\text{Lu}_2(\text{Ir}_{1-x}\text{Rh}_x)_3\text{Si}_5$. Figure 3.21 depicts the temperature-concentration phase diagram of $\text{Lu}_2(\text{Ir}_{1-x}\text{Rh}_x)_3\text{Si}_5$. It shows that T_{CDW}

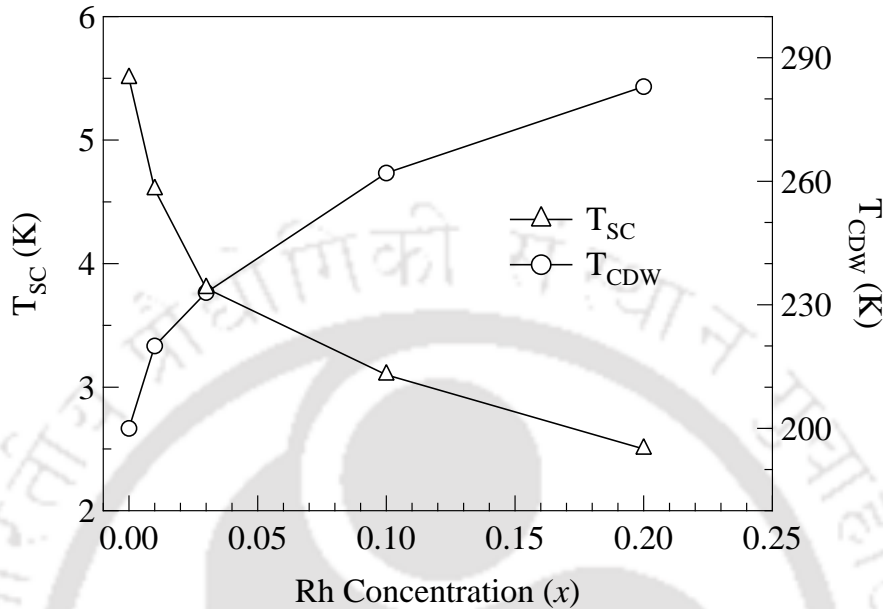


Figure 3.21: Plot of T_{CDW} and T_{SC} vs Rh concentration (x) for $\text{Lu}_2(\text{Ir}_{1-x}\text{Rh}_x)_3\text{Si}_5$ with $x = 0.00, 0.01, 0.03, 0.1, 0.2$ and 0.3 .

enhances quasi-linearly upon the increase of Rh concentration in $\text{Lu}_2(\text{Ir}_{1-x}\text{Rh}_x)_3\text{Si}_5$ while the T_{SC} is suppressed. The variation of T_{SC} and T_{CDW} with doping concentration is gradual in contrast to $\text{Lu}_5(\text{Ir}_{1-x}\text{Rh}_x)_4\text{Si}_{10}$ systems previously investigated [9]. The calculated initial concentration dependence (for small x) of T_{CDW} and T_{SC} for this system to be $(dT_{CDW}/dx)=19.73 (\pm 0.5)$ K/at.% and $(dT_{SC}/dx)=-0.88(\pm 0.09)$ K/at.%. We attribute this behavior to pressure broadening of the d conduction band in the presence of strong Coulomb repulsion. The increase of Rh concentration changes the electron density at the Fermi surface. This fall in the density of states and impairment of the Fermi-surface nesting account for the formation of negative chemical pressure. It therefore stabilized the CDW formation in $\text{Lu}_2(\text{Ir}_{1-x}\text{Rh}_x)_3\text{Si}_5$ by the increase in d -bandwidth under chemical pressure. A similar situation exists for the quasi one-dimensional charge transfer salt TTF-TCNQ [86] and in VSe_2 [87]. We also noted that both SC and CDW ordering are not noticeable at and above $x = 30\%$ of Rh concentration. This results suggest that the SC and CDW are strongly correlated and mutually incompatible to suppress each other in this $\text{Lu}_2\text{Ir}_3\text{Si}_5$ system .

At present, we use a quite distinct method to study the interplay between super-

conductivity and CDW in $\text{Lu}_2\text{Ir}_3\text{Si}_5$ by doping with Sc impurities on Lu sites. The presence of an impurity in a CDW material may lead to a change of the CDW transition temperature and also lead to the possible smearing of the CDW transition itself (see Table 11). Figure 3.22 depicts the temperature-concentration phase diagram of

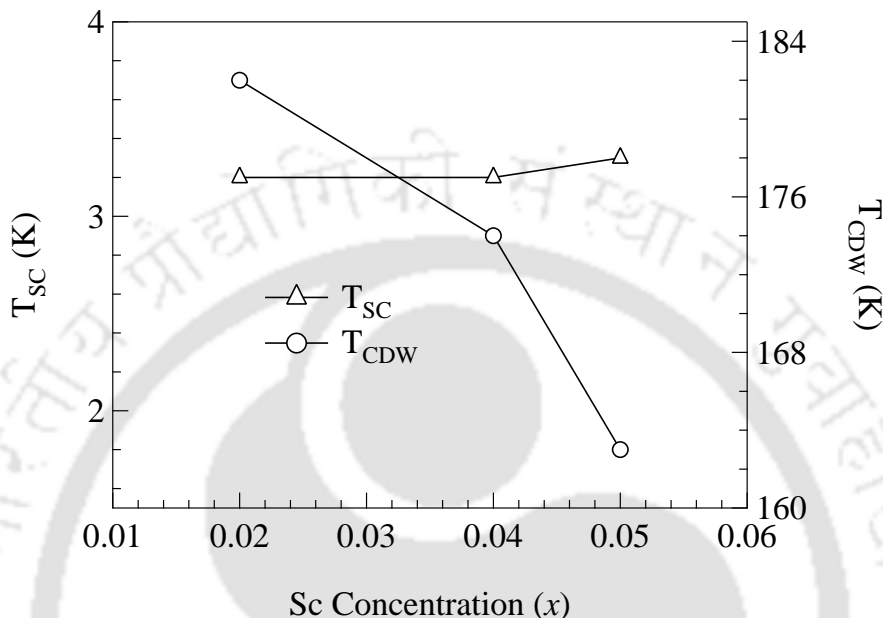


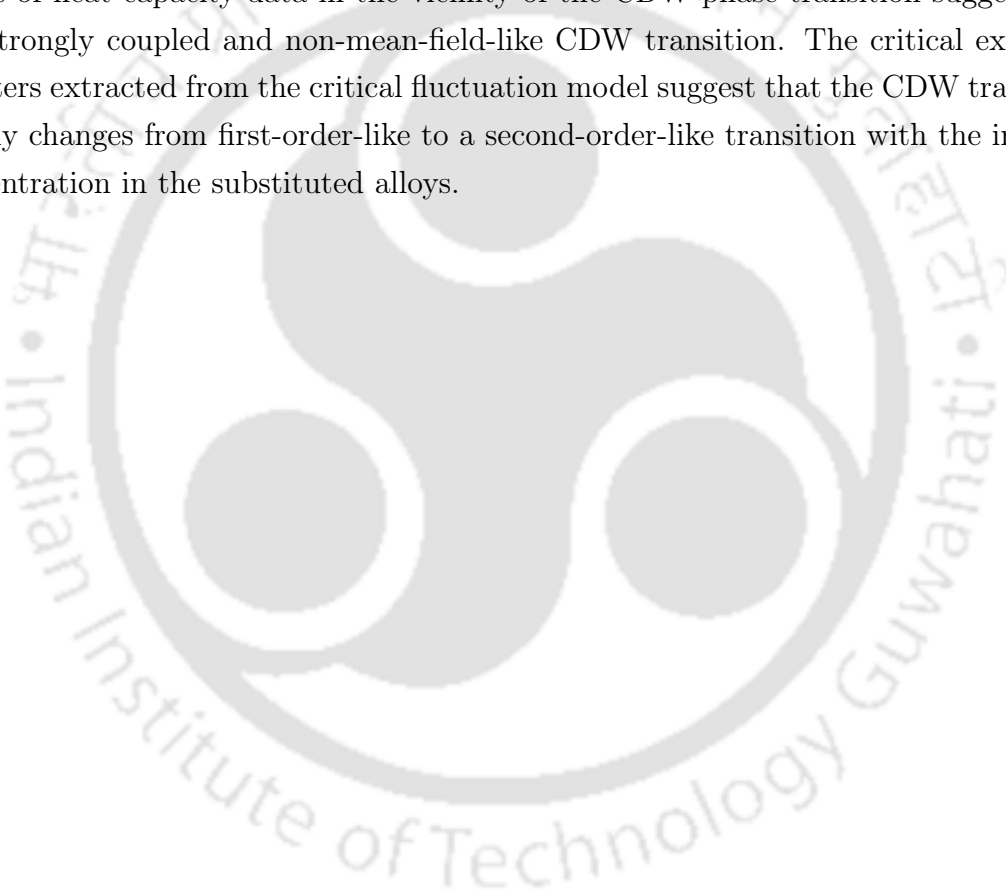
Figure 3.22: Plot of T_{CDW} and T_{SC} vs Sc concentration (x) for $(\text{Lu}_{1-x}\text{Sc}_x)_2\text{Ir}_3\text{Si}_5$ with $x = 0.02, 0.04$ and 0.05 .

$(\text{Lu}_{1-x}\text{Sc}_x)_2\text{Ir}_3\text{Si}_5$. We determined the initial concentration dependence (for small x) of T_{CDW} to be $(dT_{CDW}/dx) = -4.07 (\pm 0.2)$ K/at.%. It may be noted that the Sc substitution does not disturb the superconducting transition temperature while reducing CDW ordering till 5% of Sc concentration, the maximum attainable Sc ratio to substitute at Lu sites without affecting the parent $\text{Lu}_2\text{Ir}_3\text{Si}_5$ crystal structure. But in $(\text{Lu}_{1-x}\text{Sc}_x)_5\text{Ir}_4\text{Si}_{10}$, the T_{SC} is strongly enhanced at a very low Sc concentration in contrast to our data. Hence, our results suggest that the suppression of CDW does not take place due to the reduction of the electron in the density of states at the Fermi level, but due to the difference in the atomic weights of Sc and Lu. It does not hinder the transfer of electrons of the Fermi surface from the CDW site to the SC site. These finding suggests that the Lu site is possibly related to the origin of CDW ordering in $\text{Lu}_2\text{Ir}_3\text{Si}_5$ system.

In all of the above the temperature-concentration phase diagram, we noticed that the disorder plays a little role in the suppression/enhancement of CDW and SC.

3.5 Summary

In conclusion, the interplay and competition between the CDW and superconductivity in pseudoternary systems of $(\text{Lu}_{1-x}\text{Sc}_x)_2\text{Ir}_3\text{Si}_5$, $\text{Lu}_2(\text{Ir}_{1-x}\text{Rh}_x)_3\text{Si}_5$ and $\text{Lu}_2\text{Ir}_3(\text{Si}_{1-x}\text{Ge}_x)_5$ are studied in detail via electrical, magnetic and thermal properties. Our experiments reveals that the CDW formation in these compounds is sensitive to atomic disorder. The superconducting transition is not complete down to zero until 1.8 K for all the substituted alloys in the system. In this context, we would like to mention that preliminary measurements on single crystal $\text{Lu}_2\text{Ir}_3\text{Si}_5$ do not show a sharp drop of resistance to zero in the superconducting state. We find that there is a correlation between T_{SC} and T_{CDW} . Analysis of heat capacity data in the vicinity of the CDW phase transition suggest that it is a strongly coupled and non-mean-field-like CDW transition. The critical exponent parameters extracted from the critical fluctuation model suggest that the CDW transition gradually changes from first-order-like to a second-order-like transition with the increase of concentration in the substituted alloys.





Chapter 4

Interplay of charge density wave and superconductivity in $\text{Lu}_2\text{Ir}_3\text{Si}_5$ single crystal

4.1 Introduction

In this chapter, we have studied the phenomena of charge density wave and superconductivity and their interplay or competition on $\text{Lu}_2\text{Ir}_3\text{Si}_5$ single crystal. The polycrystalline sample $\text{Lu}_2\text{Ir}_3\text{Si}_5$ exhibits superconductivity at around 3.5 K and a strongly coupled CDW transition between 150 and 200 K [19]. The experimentally observed peculiarities of the transport properties of the $\text{Lu}_2\text{Ir}_3\text{Si}_5$ are in strong contrast to earlier reported CDW systems $\text{R}_5\text{Ir}_4\text{Si}_{10}$ [9, 88]. It has also been revealed that $\text{Lu}_2\text{Ir}_3\text{Si}_5$ shows electronically phase separated CDW, with the coexistence of CDW domains and patches of normal phase domains [71], which is quite unexpected compared to the other reported CDW systems. However, all of these studies were done on polycrystalline samples, and thus contain no information on the anisotropy which is expected for a CDW compound. In order to elucidate the properties of $\text{Lu}_2\text{Ir}_3\text{Si}_5$ and to demonstrate the existence of the CDW, we have undertaken thermodynamic, transport and magnetic measurements on $\text{Lu}_2\text{Ir}_3\text{Si}_5$ single crystals.

4.2 Experiment

Single-crystalline samples have been grown in a tetra-arc furnace using a modified Czochralski technique. The purity of the elements were Lu: 99.999%; Ir: 99.99%; Si:

99.999%. The stoichiometric ratio of elements were taken separately to make 12 g (polycrystal) melt in a tetra-arc furnace. A thin tungsten seed rod was immersed into the melt and pulled at a speed of 11 mm/h in a pure and dry argon atmosphere. After confirming the phase homogeneity of the grown crystal by using powder x-ray diffraction, we have used the first grown crystal rod as a seed in order to synthesize good quality single crystals of $\text{Lu}_2\text{Ir}_3\text{Si}_5$. The as-grown ingot produced were approximately 2-3 mm in diameter and 6 cm in length. The magnetic measurements were performed in a commercial superconducting quantum interference device (SQUID) magnetometer (MPMS5, Quantum Design, USA). The temperature dependence of electrical resistivity was measured using a home built electrical resistivity set up with the standard dc four probe technique. The heat-capacity measurement was performed using a commercial DSC system to observe the CDW transition.

4.3 Result & Discussion

4.3.1 X-ray studies

$\text{Lu}_2\text{Ir}_3\text{Si}_5$ is found in orthorhombic, $\text{U}_2\text{Co}_3\text{Si}_5$ type crystal structure with space group *Ibam*. The samples have been analyzed by EDAX to prove its 2-3-5 stoichiometry. The single crystallinity has been verified by x-ray Laue diffraction. The as-grown single crystal and observed and simulated Laue pattern of an oriented crystal are shown in Figure 4.1. The single crystals were oriented along three principle crystallographic directions using back-reflection Laue diffraction method and cut to the required sizes by spark erosion.

Atom	Ion	Wyck	x	y	z
Lu	76	8h	0.267	0.142	0.000
Ir	26	4a	0.000	0.000	0.250
Ir	26	8j	0.115	0.371	0.000
Si	14	4b	0.500	0.000	0.250
Si	14	8g	0.000	0.234	0.250
Si	14	8j	0.337	0.395	0.000

Table 4.1: Refined crystallographic parameters for $\text{Lu}_2\text{Ir}_3\text{Si}_5$ using room temperature powder x-ray diffraction data.

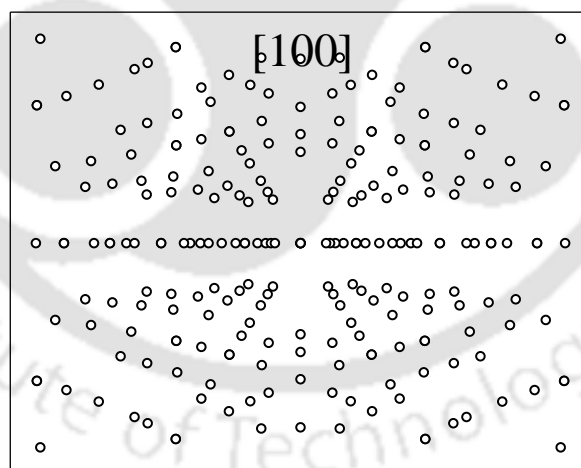
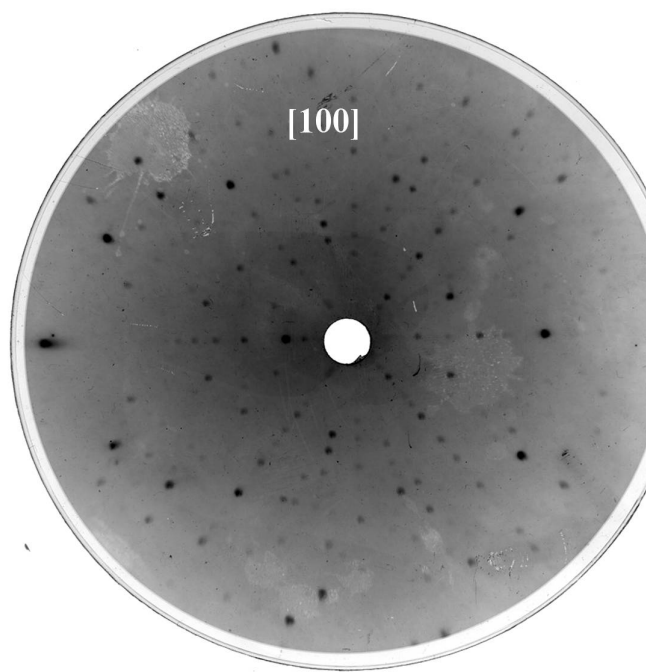
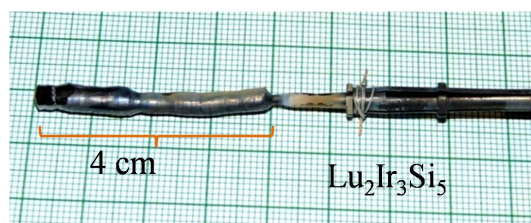


Figure 4.1: The as grown crystal and observed and simulated Laue pattern of $\text{Lu}_2\text{Ir}_3\text{Si}_5$ along the $[100]$ axis.

In order to confirm the phase homogeneity of the compounds with proper crystallographic

and lattice parameters, a Rietveld analysis of the observed x-ray pattern was done using the FULLPROF program as shown Figure 4.2. The lattice parameters obtained from the Rietveld analysis for $\text{Lu}_2\text{Ir}_3\text{Si}_5$ are $a = 9.923 \text{ \AA}$, $b = 11.311 \text{ \AA}$ and $c = 5.732 \text{ \AA}$. The lattice parameters are in close agreement with the previously reported polycrystalline data [19]. The refined crystallographic parameters are presented in Table 4.1.

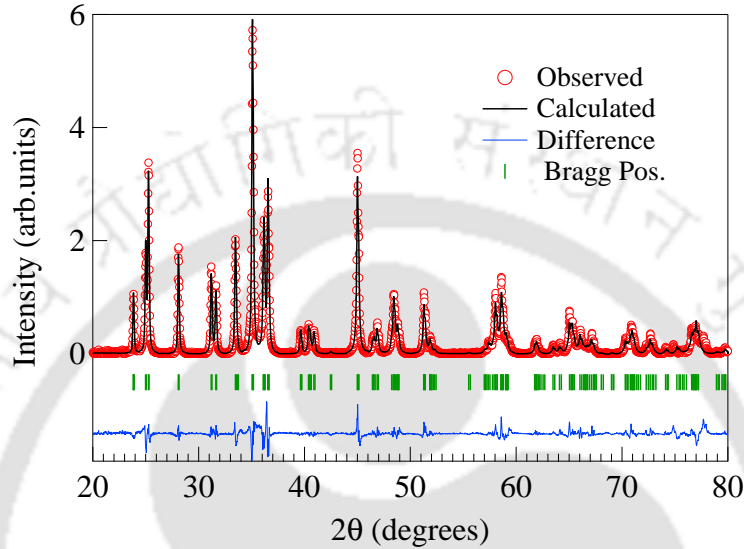


Figure 4.2: Powder x-ray diffraction data of $\text{Lu}_2\text{Ir}_3\text{Si}_5$. The solid line is the simulated data using FULLPROF (Rietveld Program).

4.3.2 Electrical resistivity

Figure 4.3 depicts temperature dependent resistivity $\rho(T)$ of $\text{Lu}_2\text{Ir}_3\text{Si}_5$ along a , b and c axes. The resistivity data recorded while warming (from 2 to 300 K) and cooling (between 130 and 300 K) the sample at the rate of 1 K/min. The main panel shows upturn of the resistivity at the high temperature which is ascribed to the CDW or structural transition. The inset of all the main panels demonstrate the onset of superconducting transition at low temperature. The SC transition in this system is much broader. Also, the resistivity drop is not complete down to 2 K, as seen in the polycrystalline samples, as in Figure 4.3(b). A sharp upward jump in resistivity data at high temperature is similar to the one usually observed in charge-or-spin-density wave (CDW/SDW) transition which is due to opening up of a gap in the electronic density of states at the Fermi surface. After reaching a maximum, the resistivity shows metallic behaviour down to the lowest temperatures before undergoing to the superconducting transition. Besides, we encounter

the onset/upturn of the transition for both warming and cooling at different temperature regimes.

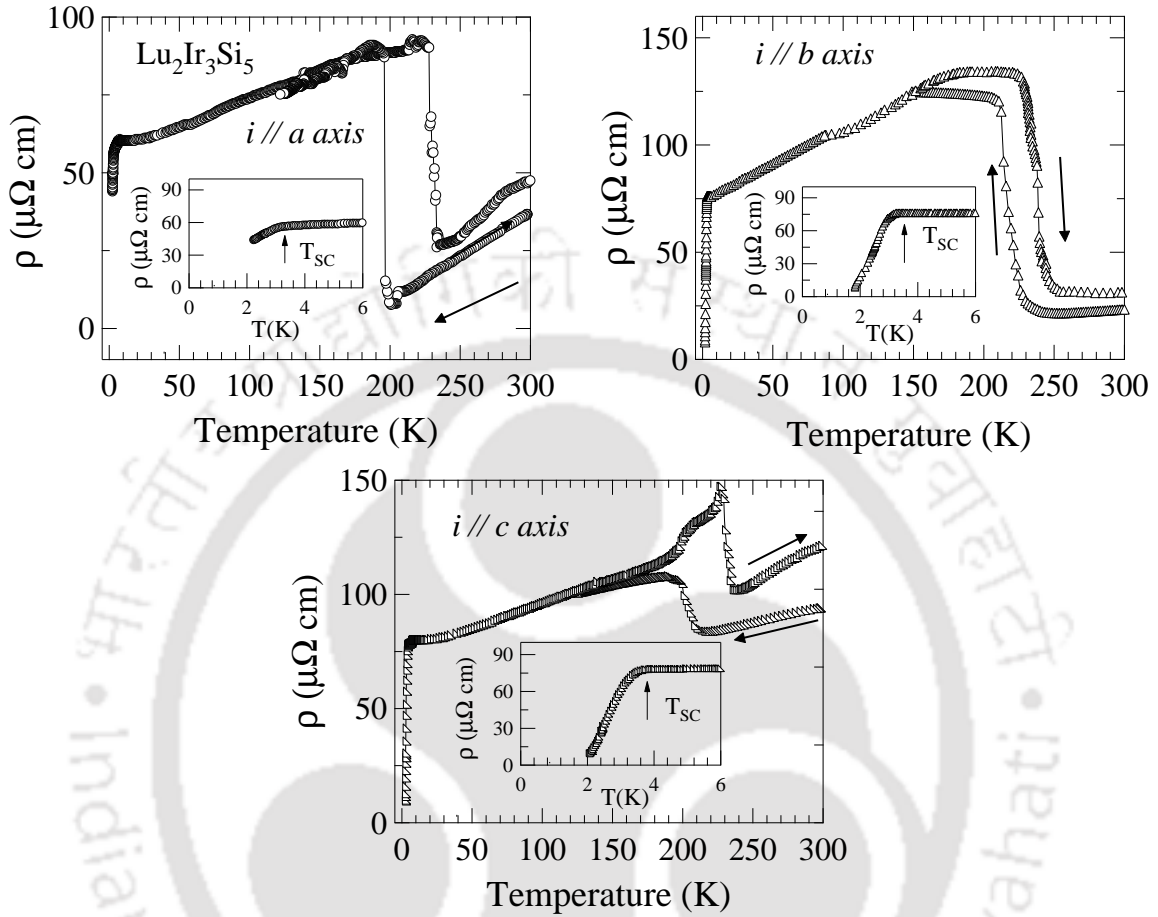


Figure 4.3: The temperature dependence of the electrical resistivity $\rho(T)$ of $\text{Lu}_2\text{Ir}_3\text{Si}_5$. Main panels demonstrate the CDW transition at high temperatures, along the three principle axes, for both the cooling (shown by \leftarrow) and warming (shown by \rightarrow) of the sample. Inset shows the low temperature resistivity data between 2 and 6 K to look at the SC transition along a , b and c axes.

Hence it is worthwhile to mention about a pronounced thermal hysteresis between up and down scans, which demonstrates a first-order transition for the system. The transition temperatures of SC and CDW (T_{SC} and T_{CDW}) have been determined from the peak position in the derivative plots of $d\rho/dT$ vs T . The resistivity values at 300 K, amplitude of the resistive anomaly, transition widths for temperature and resistivity and hysteresis widths of the curves while warming and cooling along three different principle axes are listed in Table 4.2 along with T_{SC} and T_{CDW} . Obvious anisotropy was observed

axes	T_{CDW} (K)	ΔT_{CDW} (K)	$\Delta\rho_{CDW}$ ($\mu\Omega cm$)	$\rho(300K)$ ($\mu\Omega cm$)	<i>Hysteresis</i> <i>width</i> ($\mu\Omega cm$)	T_{SC} (K)
<i>a</i>	231	6	62	46	37	3.2
<i>b</i>	232	10	97	31	18	3.2
<i>c</i>	230	8	47	120	43	3.8

Table 4.2: CDW transition parameters obtained from the temperature dependence of the resistivity of Lu₂Ir₃Si₅.

between *c* and *a*, *b* axes. By comparing the parameters obtained from resistivity studies (considering warming data) along all the three axes, one can found that *c* axis shows a huge thermal hysteresis of almost 43 K. The magnitude of the resistivity anisotropy along three different directions is also to be noted, which suggests about the influence of charge carriers.

4.3.3 Magnetic susceptibility

The temperature dependence of magnetic susceptibilities for Lu₂Ir₃Si₅ with applied magnetic field of $H = 5T$ and $H = 10$ Oe along *a*, *b* and *c* axes are shown in Figure 4.4. In Figure 4.4(a), (b) and (c), the large diamagnetic drops of magnetic susceptibility appeared at high temperature, signifying a CDW transition which driven by the onset electron-phonon coupling. It is interesting to note that there is a huge diamagnetic drop in the susceptibility data across the transition as we cool down from 300 K. The peak in $d\chi/dT$ vs T has been termed as T_{CDW} . The transition temperatures for both cooling and warming curve occur at different temperatures (see in Figure 4.4). Further, the hysteresis in the susceptibility data is registered for all the three axes. This comes about due to the reduction in the density of states at the Fermi surface because of opening up of a gap at the Fermi surface accompanying the CDW ordering.

Figure 4.4(d) demonstrated FC (field cooled) and ZFC (zero field cooled) data at the onset of the diamagnetic signal. The superconducting transition is clearly seen with an abrupt diamagnetic drop below 3 K. However, the transition is not complete, as reported in polycrystalline sample. The diamagnetic drop is very weak along the *a* axis compared to the *b* and *c* axes. Here also, similar to the resistivity data, the onset SC transition is

seen. We have determined the SC transition temperature, T_{SC} via the peak in $d\chi/dT$ vs T plot. The characterized T_{CDW} (from warming curve), T_{SC} (from ZFC data), the diamagnetic drop in the susceptibility with jump size $\Delta\chi_{CDW}$ and hysteresis width are listed in Table 4.3. These results are consistent with the resistivity data.

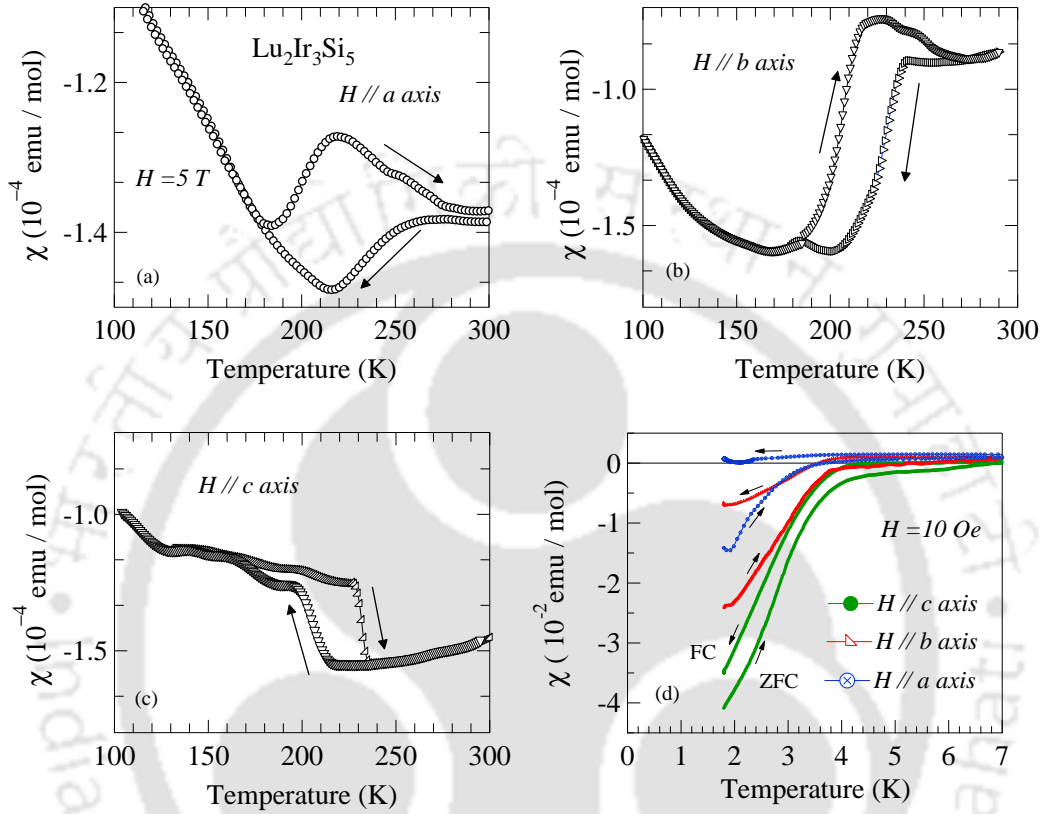


Figure 4.4: The temperature dependence of the dc susceptibility $\rho(T)$ of $\text{Lu}_2\text{Ir}_3\text{Si}_5$. (a), (b) and (c) demonstrate CDW transition at high temperatures along three principle axes (a , b and c) for both the cooling (shown by \leftarrow) and warming (shown by \rightarrow) of the sample. (d) The low temperature susceptibility data between 2 and 6 K to look at SC transition along a , b and c axes.

4.3.3.1 Superconducting state: Lower ($H_{C_1}(T)$) & Upper critical ($H_{C_2}(T)$) magnetic fields

The superconducting state parameters such as, the lower critical magnetic field $H_{C_1}(T)$ and the upper critical magnetic field $H_{C_2}(T)$ were estimated from the isothermal magnetization data, taken in a temperature interval from 1.8 to 5 K. The value of $H_{C_1}(T)$ was estimated as the limiting values where the magnetization deviates from the linear M vs

axes	T_{CDW} (K)	$\Delta\chi_{CDW}$ (emu/mol)	Hysteresis width (emu/mol)	T_{SC} (K)
<i>a</i>	229	2.1×10^{-5}	29	2.6
<i>b</i>	231	7.1×10^{-5}	18	2.7
<i>c</i>	232	3×10^{-5}	33	2.8

Table 4.3: CDW transition parameters obtained from the temperature dependence of the dc susceptibility of Lu₂Ir₃Si₅.

H dependence. The limiting field marks the entry of vortices into the superconductor. The H_{C_2} value obtained from the limiting field (setting of the diamagnetism) where deviation from the (paramagnetic) linear M vs H occurs near the normal-superconducting phase boundary. The temperature dependence of $H_{C_1}(T)$ and $H_{C_2}(T)$ for Lu₂Ir₃Si₅ along all the three axes are shown in Figure 4.5(a) and (b) respectively. One can found that $H_{C_1}(T)$ and $H_{C_2}(T)$ along the c -axis is larger than other two axes.

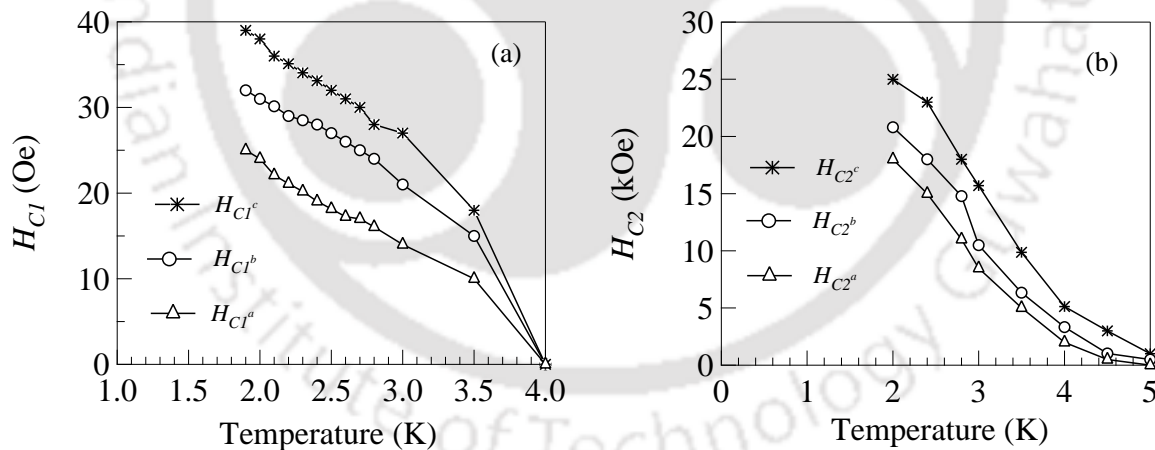


Figure 4.5: (a) The lower critical field $H_{C_1}(T)$ and (b) the upper critical field $H_{C_2}(T)$ vs temperature extracted from M vs H measurement for Lu₂Ir₃Si₅.

H_{C_2} at $T=0$ K can be figured out from the equation [89],

$$H_{C_2}(0) = 0.69T_C [-dH_{C_2}/dT]_{T=T_C} \quad (4.1)$$

By using the slope of H_{C_2} , we estimated $H_{C_2}^i(0)$ in $\text{Lu}_2\text{Ir}_3\text{Si}_5$ where $i = a, b, c$. Coherence length for three directions at $T=0$ K calculated by the standard formula $H_{C_2}^i(0) = \Phi_0 / (2\pi\xi_j\xi_k)$, where Φ_0 is the flux quantum. The lower critical field at zero temperature $H_{C_1}(0)$ evaluated from our $H_{C_1}(T)$ data which seem to fit to the relation $H_{C_1}(T) = H_{C_1}(0) [1 - (T/T_C)^2]$ over a wide temperature range. The penetration depth λ , calculated from H_{C_1} with the well known equation $H_{C_1}(T) = \frac{\Phi_0}{4\pi\lambda^2} \ln(\kappa)$ [34], where $\kappa = \lambda/\xi$ is the Ginzburg-Landau parameter, and ξ is the coherence length. Table 4.4 listed the value of the superconducting parameters calculated from the relation obtained from the anisotropic Ginzburg-Landau theory. It reveals that $\text{Lu}_2\text{Ir}_3\text{Si}_5$ is a hard Type-II superconductor with a large κ value. The anisotropy in the computed superconducting parameters can be approximately estimated from the anisotropic GL theory with an anisotropy parameter γ denoting the ratio $H_{C_1}^c/H_{C_1}^a$ and $H_{C_2}^c/H_{C_2}^a$, which come about 1.6 and 1.8 respectively. The low value anisotropy suggests of a strong coupling between the planes, unlike that of chalcogenides such as, 2H-NbSe_2 .

	H_{C_1} (mT)	H_{C_2} (T)	λ (Å)	ξ (Å)	κ
$H a$	1.6	1.2	3888	108	36
$H b$	2.2	1.7	5217	141	37
$H c$	2.5	2.2	7080	177	40

Table 4.4: Different superconducting parameters of $\text{Lu}_2\text{Ir}_3\text{Si}_5$ are noted.

4.3.4 Heat capacity

Figure 4.6 depicts the temperature dependence of specific heat capacity data in the temperature range between 150 and 300 K. The large peaks in cooling and warming curves denote the transition of the compound into a CDW state. The anomalies are seen together with the resistivity and susceptibility measurements at around the same temperature. The transition width, ΔT_{CDW} has determined by taking the temperature width of half-peak height. It gives a value of about 4.6 K, and that is much sharper than the previously reported value for a polycrystalline sample. The specific heat jump, ΔC_P can be estimated near the transition, after the background subtraction which has been done by fitting lattice contribution for the data far away from the transition. The entropy

change, ΔS is then obtained by integrating the curve under $\Delta C_{CDW}/T$ as a function of T . The values of ΔC_P and ΔS for both warming and cooling curves are given in Table 4.5. For comparison, it includes Lu₂Ir₃Si₅ polycrystal result, along with other two

	T_{CDW} (K)	$\Delta T_{CDW}/T_{CDW}$ (%)	ΔC_P (J/ mol K)	ΔS (R)	$\Delta C_P/C_P$ (%)
warming data	240	1.9	55	0.35	96
cooling data	190	1.6	57	0.33	92
Lu ₂ Ir ₃ Si ₅ *	210	14	45	0.19	25
K _{0.3} MoO ₃	180	11	8	0.18	6
NbSe ₃	$T_{CDW}^1=58$ K	1.7	1.24	0.005	1.5
	$T_{CDW}^2=145$ K	4.8	9.14	0.01	2.5

* Polycrystal

Table 4.5: Summary of specific heat anomalies of Lu₂Ir₃Si₅ compared to the well-studied CDW systems K_{0.3}MoO₃ and NbSe₃.

well studied CDW systems such as K_{0.3}MoO₃ [90, 82, 83] and NbSe₃[91]. It is noted that the specific heat anomaly and the entropy change for Lu₂Ir₃Si₅ single crystal are much larger and sharper than that of other CDW systems. Moreover, polycrystalline Lu₂Ir₃Si₅ samples are somewhat smaller than those obtained from single crystal. Importantly, it should be appraised here that the single crystals have a better sample quality than that of the polycrystalline samples. Also, the presence of a sharp peak anomaly gives a clear evidence of a high electron density and a large amplitude of the periodic lattice distortion accompanying the CDW. Compared with the 2H-TaSe₂ and 2H-TaS₂ reports [81], this large phonon specific heat anomaly may be due to the presence of an incommensurate CDW phase.

The CDW transition in Lu₂Ir₃Si₅ (Figure 4.6) displays spike shaped large specific heat jump around 233 K within a very narrow temperature region ($\Delta T_{CDW}/T_{CDW} \sim 1.9\%$). Furthermore, the pronounced thermal hysteresis in Lu₂Ir₃Si₅ between up and down scans in resistivity, magnetic susceptibility and specific heat capacity data explored the existence of a first order transition as observed in the polycrystalline sample. Hence, the heat capacity data in the vicinity of CDW transition is analyzed with a model of critical fluctuation proposed by Kuo *et al.* The utility of the model was emphasized in chapter 3 (Sec. 3.3.1.4).

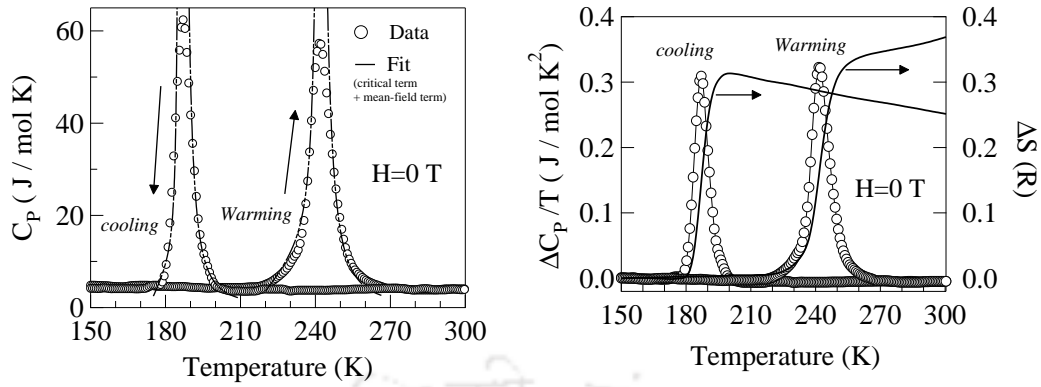


Figure 4.6: The temperature dependence of specific heat measurements (DSC data) on both warming and cooling of $\text{Lu}_2\text{Ir}_3\text{Si}_5$ after subtracting the smooth background. (a) The agreement between data points (open circles) and fit (solid line) to the model of critical fluctuation plus a mean-field contribution in the vicinity of CDW transition. (b) The plot of $\Delta C_P/T$ vs T (left axis) and the entropy change ΔS (right axis) associated with the transition.

	Mean-field term		Fluctuation term				T_{CDW} (K)
	γ^* (J/mol K ²)	β	b^- (J/mol K)	α^-	b^+ (J/mol K)	α^+	
Warming data	6.7×10^{-2}	-9	1.2×10^{-2}	2	4.5×10^{-2}	1.9	233
Cooling data	7.1×10^{-2}	-15	3.2×10^{-3}	2	5.1×10^{-2}	1.8	186

Table 4.6: The fitting parameters extracted from the specific heat data of $\text{Lu}_2\text{Ir}_3\text{Si}_5$ to a model of critical fluctuations in addition to mean-field contributions.

The values of the extracted fitting parameters for all the samples are listed in Table 4.6, providing important information about the transitions. It can be seen that the critical exponents, α^- and α^+ extracted from the fit for $\text{Lu}_2\text{Ir}_3\text{Si}_5$ are close to 2, much larger than the value $\alpha = 0.5$, appropriate for a mean-field-like transition. The compound shows a divergence with a larger exponent in C_P near T_{CDW} reflects the very narrow transition width [80]. We also obtained another important quantity γ^* from the fit where γ^*T_{CDW} represents the electronic specific heat jump of the mean-field term near the 3D ordering temperature. It yields the mean field value of specific heat jump, $\Delta C_{CDW} = 15.61 \text{ J/mol K}$ for $\text{Lu}_2\text{Ir}_3\text{Si}_5$, which is much smaller than the observed value

$\Delta C_{CDW} = 55 \text{ J/mol K}$. The value of the electronic specific heat γ^* for $\text{Lu}_2\text{Ir}_3\text{Si}_5$ is about $6.7 \times 10^{-2} \text{ J/mol K}^2$ and the bare Sommerfeld's constant $\gamma = 7.5 \times 10^{-3}$. It yields a ratio of $\gamma^*/\gamma = 8.9$, which is about 6.2 times larger than the BCS weak-coupling limit value 1.43, thereby indicating a strong coupling scheme nature of the CDW transition. Such enhancements in the specific heat jump from their mean field value have been reported in other CDW systems [80, 83, 82]. The observations made above are consistent with our earlier reported polycrystalline $\text{Lu}_2\text{Ir}_3\text{Si}_5$ samples.

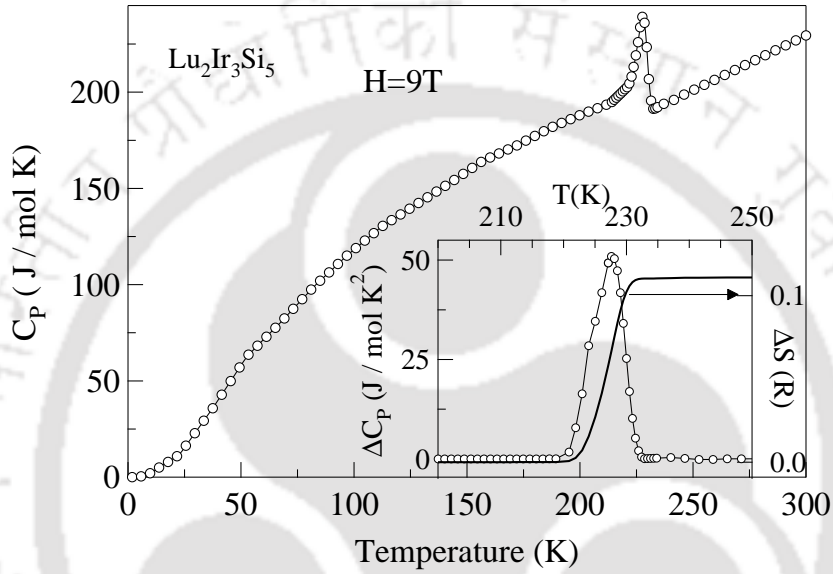


Figure 4.7: The specific heat capacities of $\text{Lu}_2\text{Ir}_3\text{Si}_5$ in the field of 9 T while warming. Inset shows the specific heat on an enlarged temperature scale (left axis) and the calculated entropy change around 230 K (right axis).

The coherence length ξ_0 calculated for $\text{Lu}_2\text{Ir}_3\text{Si}_5$, from the Ginzburg criteria,

$$\Delta T_G = (T_{CDW}/32) (k_B/\pi \Delta C_{CDW} \xi_0^3)^2 \quad (4.2)$$

gives the value of about 5.6 \AA close to polycrystalline result (5.4 \AA). According to McMillan's model proposed for strong CDW systems, the deduced short coherence length is an indication of strong interchain coupling in $\text{Lu}_2\text{Ir}_3\text{Si}_5$. In addition, it was reported that a large number of soft phonon modes in the transition region contribute substantially to the heat capacity. Further, the larger value of $\gamma^* T_{CDW}$ corroborates the above inference via an assumption that the larger portion of Fermi surface nesting occurs in the studied compound, as compared to other CDW compounds. It would explain the origin of huge

specific heat jumps displayed in Si compound.

Figure 4.7 demonstrates the heat capacities of $\text{Lu}_2\text{Ir}_3\text{Si}_5$ in the field of 9 T performed using PPMS. It found that the transition does not change with applied magnetic field upto 9 T, as the sample contains no magnetic atoms. The entropy involved here is substantial ($0.16(\text{R})$) and the heat capacity jump, ΔC_P is 45 J/mol K.

4.4 Summary

We have investigated the single crystal of $\text{Lu}_2\text{Ir}_3\text{Si}_5$ using magnetic susceptibility, electrical resistivity, x-ray diffraction and heat capacity measurements. We find that the compound adopts orthorhombic $\text{U}_2\text{Co}_3\text{Si}_5$ type crystal structure. The as-grown high quality of the single crystal $\text{Lu}_2\text{Ir}_3\text{Si}_5$ registered a superconducting transition at 3.5 K and it is also showed that a strongly coupled charge density wave transition occurs below 235 K with a huge thermal hysteresis in all the measurements. The first order nature of CDW transition is ascertained by a very narrow and huge cusp (55 J/mol K) in the specific heat. By using critical fluctuation model, the quantitative analysis for the specific heat data in CDW transition yields a critical exponent, $\alpha \sim 2$ which is much larger than the predicted mean field value $\alpha = 0.5$. We obtain a ratio of $\gamma^*/\gamma = 8.9$, which is about 6.2 times larger than the BCS weak-coupling limit value 1.43, indicating strong coupling nature of the CDW transition. In addition, the superconducting parameters are deduced from the anisotropic Ginzburg-Landau theory. It reveals that $\text{Lu}_2\text{Ir}_3\text{Si}_5$ is a hard type-II superconductor with a large κ value. The anisotropy parameter ($H_{C_2}^c/H_{C_2}^a$) has a value of about 1.8, which suggests of a low anisotropy and hence a stronger coupling between the planes unlike that of chalcogenides such as, 2H-NbSe₂ [92].



Chapter 5

Magnetic ordering and crystal field effects in the $R_2Ir_3Sn_5$ (R=La-Nd, Gd-Tm) system

5.1 Introduction

In the field of strongly correlated electron systems, the rare earth intermetallics have been at the centre stage of active research. In this context, the ternary rare earth transition metal silicides and germanides with the general formula $R_2T_3X_5$, (R = rare-earth elements; T = transition metal and X = *s-p* metal), have drawn recent attention with respect to its crystallographic, magnetic and electrical properties [1, 2, 3]. In the early 1980's, considerable investigation has been carried in the Fe family of silicides $R_2Fe_3Si_5$ [4, 93] with a wide variety of properties such as coexistence of superconductivity and magnetism, reentrant superconductivity ($Tm_2Fe_3Si_5$) [76], disorder sensitive superconductor ($Lu_2Fe_3Si_5$) [94] and superconductivity below commensurate and incommensurate antiferromagnetic transitions ($Er_2Fe_3Si_5$) [95] etc. It is also to be noted that there are large number of compounds in the 2-3-5 system with similar crystal structure having remarkable ground state properties. For example, $Yb_2Pt_3Sn_5$ (heavy fermion with mixed valence behavior) [96], $Ce_2(Ir, Rh)_3(Sn, Ge)_5$ (moderate heavy fermion and kondo lattice system with antiferromagnetic ordering) [98, 97] and $Pr_2Rh_3Ge_5$ (recently reported heavy fermion behavior due to crystal field excitation) [99] are only a few of them. However, until today comprehensive studies of $R_2(Ir, Rh, Ni)_3(Si, Ge, Sn)_5$ have not been pursued [8, 100, 101, 102]. Hence, we have taken the opportunity to study $R_2Ir_3Sn_5$ series. Since Ir and Sn atoms do not carry any magnetic moment, the magnetic properties of these

compounds are governed by conduction-electron mediated exchange interactions on the rare-earth moments, and by the effect of crystalline electric field (CEF) acting on the $4f$ electrons. Hence, it will be of interest to study magnetism and influence of CEF on magnetic ordering in $R_2Ir_3Sn_5$ family.

With this in view, as a part of our continuing effort to investigate the 2-3-5 system, we present in this chapter a detailed electrical resistivity, magnetic susceptibility and low temperature heat capacity results for polycrystalline samples of the series of compounds $R_2Ir_3Sn_5$ (R = La, Ce - Nd, Gd - Tm) compounds. To the best of our knowledge, for the first time the synthesis and magnetic properties of $R_2Ir_3Sn_5$ series.

5.2 Experiment

The polycrystalline samples of $R_2Ir_3Sn_5$ (R = La, Ce - Nd, Gd - Tm) were prepared by usual arc melting method. The stoichiometric proportions of each constituent element was taken separately and then melted together by using arc furnace on a water cooled copper hearth under Ti gettered in an atmosphere of continuously flowing argon gas. The purity of rare-earth metals was 99.9% whereas the purity of Ir and Sn were 99.999%. The resulting alloy buttons were turned over and remelted several times to promote homogeneity. The as cast compounds were wrapped in the tantalum foil, sealed in a quartz tube under vacuum and annealed at 900°C for 8 days. The small pieces of annealed $R_2Ir_3Sn_5$ (R = La, Ce - Nd, Gd - Tm) samples were used for room temperature powder x-ray diffraction (XRD) with $\text{Cu K}\alpha$ radiation by using PANalytical commercial x-ray diffractometer. The XRD pattern of the samples confirmed the structure and the absence of any impurity phases. The compounds $R_2Ir_3Sn_5$ with R = Ce - Nd, Gd - Tm were found to adopt the orthorhombic ($Cmc2_1$) $Y_2Rh_3Sn_5$ [103] structure, however, $La_2Ir_3Sn_5$, crystallizes in an orthorhombic $U_2Co_3Si_5$ ($Ibam$) type structure. The initial structural model for $R_2Ir_3Sn_5$ were generated from the atomic positions reported for isostructural and parent compound $Y_2Rh_3Sn_5$ by Meot-Meyer *et al.* and later, it was used in subsequent refinement procedure. The lattice constants a , b , and c in series $R_2Ir_3Sn_5$ were estimated from Reitveld fit to their x-ray diffraction patterns using FULLPROF program [78]. The lattice parameters obtained from this analysis are listed in Table 5.1, where we notice that lattice volume decreases from lighter to heavier rare earth elements. The unit cell of orthorhombic $R_2Ir_3Sn_5(Cmc2_1)$ structure is shown in Figure 5.1. It is evident from Figure 5.1, that $R_2Ir_3Sn_5$ possesses three-dimensional structure, being build up of two-dimensional Ir-Sn rings, which when stacked in the a -direction encapsulated R

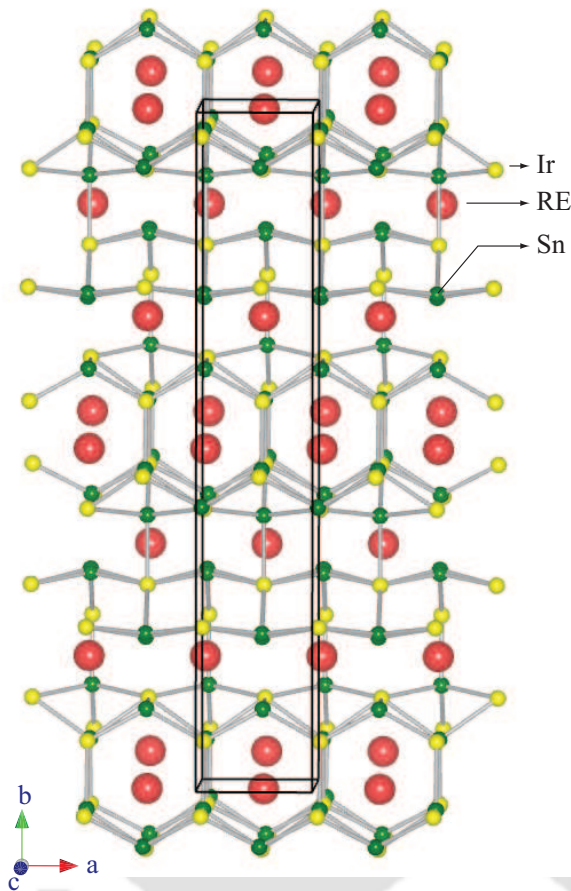


Figure 5.1: Crystal structure of the unit cell of the series $R_2Ir_3Sn_5$ (Ce: medium isolated red spheres, Ir : small yellow spheres and Sn: small green spheres).

atoms in three-dimensional channels. In $R_2Ir_3Sn_5$, R atoms reside in distorted pentagonal ([100] direction) and hexagonal ([001] direction) channels created by the Ir and Sn atoms. The local coordination environments for the Ir atoms can be described as distorted monocapped trigonal prisms. The Ir-Sn and Sn-Sn distances are considerably longer than the sum of the covalent radii of Ir and Sn. The unit cell for $La_2Ir_3Sn_5$ has a single La site, two Ir site and three Sn site whereas $R_2Ir_3Sn_5$ forms non-centrosymmetric ($Cmc2_1$) structure which results in two R sites, three Ir sites and five Sn sites, all on 4a Wyckoff positions. Hence the hybridization between d - and f - orbitals are different for these two crystal structures, it has to be taken into account in further analysis of magnetization measurements.

The electrical resistivity in the temperature range from 1.8 to 300 K was measured using a home built electrical resistivity set up with the standard dc four probe technique. The temperature dependence of dc magnetic susceptibility (χ) was measured using a com-

Sample	a (Å)	b (Å)	c (Å)	v (Å ³)
La ₂ Ir ₃ Sn ₅	10.781	12.958	6.327	884.356
Ce ₂ Ir ₃ Sn ₅	4.471	26.443	7.261	858.499
Pr ₂ Ir ₃ Sn ₅	4.468	26.474	7.254	858.045
Nd ₂ Ir ₃ Sn ₅	4.457	26.444	7.246	854.021
Gd ₂ Ir ₃ Sn ₅	4.408	26.304	7.211	836.101
Tb ₂ Ir ₃ Sn ₅	4.400	26.241	7.200	831.314
Dy ₂ Ir ₃ Sn ₅	4.395	26.256	7.195	830.267
Ho ₂ Ir ₃ Sn ₅	4.378	26.346	7.185	828.737
Er ₂ Ir ₃ Sn ₅	4.370	26.277	4.178	824.253
Tm ₂ Ir ₃ Sn ₅	4.366	26.295	7.173	823.488

Table 5.1: Lattice parameters of $R_2Ir_3Sn_5$

mercial superconducting quantum interference device (SQUID) magnetometer (MPMS5, Quantum Design, USA) in a field of 4 kOe for the temperatures between 1.8 to 300 K. The isothermal magnetization was measured in the fields up to 5 T. The heat capacity measurement in zero field in the temperature range from 2 to 30 K was performed in a Quantum Design Physical Properties Measurement System (PPMS).

5.3 Results

5.3.1 Magnetic susceptibility and magnetization studies

5.3.1.1 Magnetic susceptibility of $R_2Ir_3Sn_5$ (R = La, Ce - Tm)

The temperature dependence of inverse dc susceptibility (χ^{-1}) of $R_2Ir_3Sn_5$ (R = Ce - Tm) measured in an applied field of 4 kOe is shown in Figure 5.2 and Figure 5.3. Insets show the low temperature susceptibility χ behavior (and $d\chi/dT$ for Gd₂Ir₃Sn₅ and Tb₂Ir₃Sn₅) of the respective compounds.

The high temperature ($100 < T < 300$ K) magnetization is fitted to the modified Curie - Weiss law which is given by:

$$\chi = \chi_0 + \frac{C}{T - \Theta_P} \quad (5.1)$$

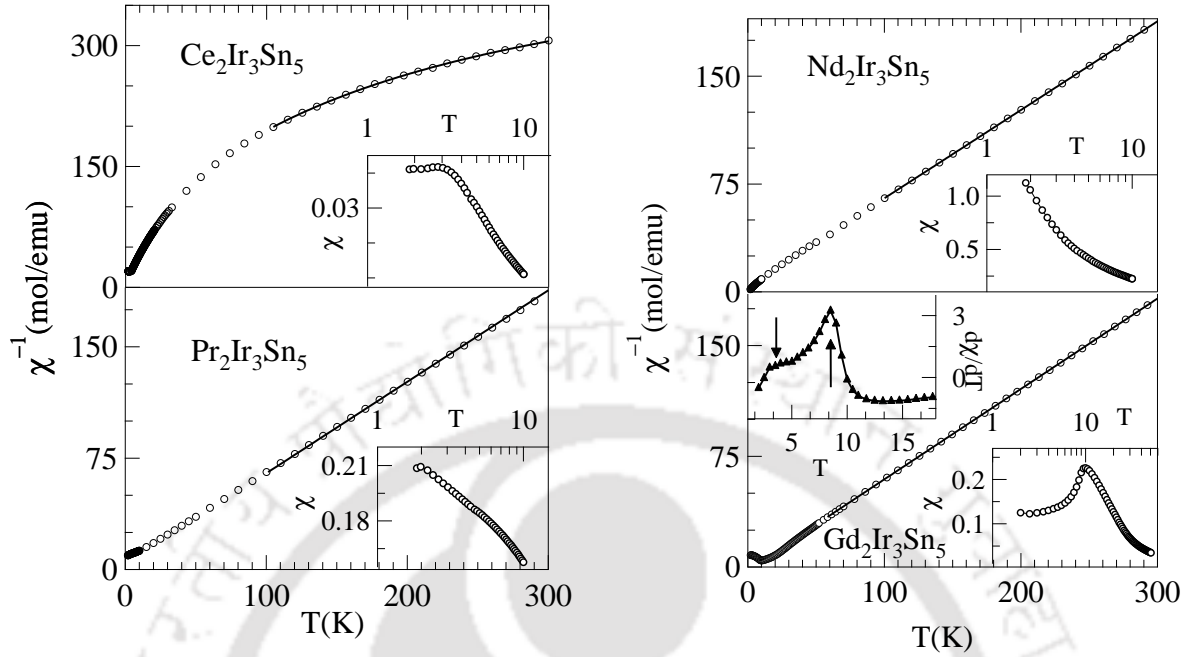


Figure 5.2: Variation of inverse dc susceptibility (χ^{-1}) of $R_2Ir_3Sn_5$ ($R = Ce - Gd$) from 1.8 to 300 K in the field of 4 kOe. The inset shows the susceptibility (χ) behavior in low temperatures. The solid line is a fit to the Curie - Weiss relation.

Here, χ_0 is the temperature - independent term including the diamagnetic susceptibility (χ_{dia}) which arises due to the presence of ion cores, the Pauli spin susceptibility (χ_{pauli}) of the conduction electrons, and Landau susceptibility (χ_{Landau}) of the diamagnetic orbital contribution due to the conduction electrons. Θ_P is the Curie - Weiss temperature and C is the Curie constant which can be written in terms of effective moments as

$$C \text{ (emu K/mol)} = \frac{N_A (\mu_{eff})^2 x}{3k_B} \approx \frac{(\mu_{eff})^2 x}{8}, \quad (5.2)$$

where x is the number of magnetic Rare earth ions (R) per formula, N_A is the Avogadro number and k_B is the Boltzmann constant. The Curie - Weiss fit is marked by a solid line in the main plots of Figure 5.2 and Figure 5.3. The estimated effective moments, listed in Table 5.2, for $R_2Ir_3Sn_5$ ($R = Ce - Tm$) samples are in good agreement with the Russel - Saunders values, $\mu_{eff} = g\mu_B [J(J+1)]^{1/2}$, calculated for R^{3+} free ions which indicate that the magnetic interaction of these compounds are mainly due to that of R^{3+} ions and there is no contribution from the Ir. But in some compounds, the effective moment is found to be smaller than the moment of rare - earth (R^{3+}) free ions which may be due to the

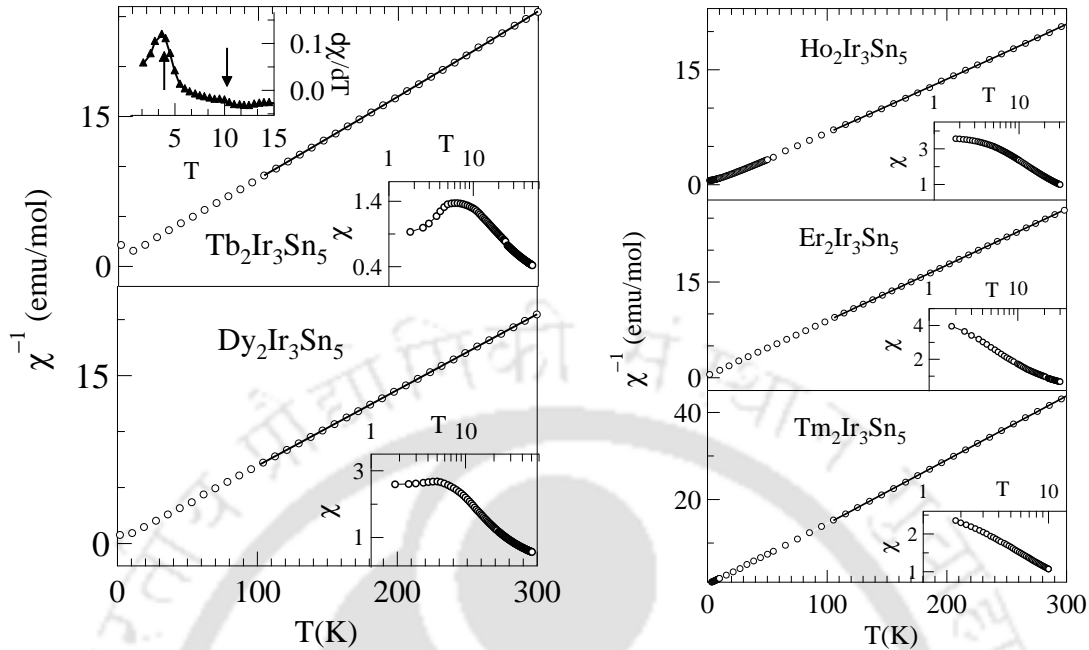


Figure 5.3: Variation of inverse dc susceptibility (χ^{-1}) of $R_2Ir_3Sn_5$ (R = Tb - Tm) from 1.8 to 300 K in the field of 4 kOe. The inset shows the susceptibility (χ) behavior in low temperatures. The solid line is a fit to the Curie - Weiss relation.

presence of crystal field effects. Most of the compounds of lighter rare earth elements show relatively small and negative value of the Curie - Weiss temperature (Θ_p), which implies the presence of antiferromagnetic correlations. The positive Θ_p indicates ferromagnetic correlation at high temperatures for heavier rare earth element based compounds.

The low temperature $\chi(T)$ data for most of the compounds, shown in the inset of Figure 5.2 and Figure 5.3, display small upturn in susceptibility which possibly indicate the signature of the onset of antiferromagnetic ordering in these materials. The susceptibility of $Ce_2Ir_3Sn_5$ exhibits a cusp at 2.5 K corresponding to antiferromagnetic order. $Pr_2Ir_3Sn_5$ and $Nd_2Ir_3Sn_5$ do not reveal any magnetic ordering down to 1.8 K. The low temperature $d(\chi)/dT$ vs T plot for $Gd_2Ir_3Sn_5$ and $Tb_2Ir_3Sn_5$ brings out multiple anomalies which is marked by arrows. $Gd_2Ir_3Sn_5$ demonstrate two magnetic transitions at 3.2 K and 9.5 K while the magnetic ordering temperatures of $Tb_2Ir_3Sn_5$ are at 3.9 K and 10 K. For $Dy_2Ir_3Sn_5$, the low temperature χ data show single magnetic ordering (5 K) in contrast to multiple anomalies in heat capacity. $Ho_2Ir_3Sn_5$, $Er_2Ir_3Sn_5$ and $Tm_2Ir_3Sn_5$, exhibit antiferromagnetic orderings at 2 K, 1.9 K and 1.9 K, respectively.

Sample	χ_0 (emu / mol K)	μ_{eff} (μ_B)	μ_{th} (μ_B)	Θ_p (K)
Ce ₂ Ir ₃ Sn ₅	2.1×10^{-3}	2.57	2.54	-37.5
Pr ₂ Ir ₃ Sn ₅	8.56×10^{-6}	3.60	3.62	-5.28
Nd ₂ Ir ₃ Sn ₅	1.01×10^{-4}	3.58	3.58	-5.65
Gd ₂ Ir ₃ Sn ₅	1.14×10^{-6}	7.23	7.94	2.99
Tb ₂ Ir ₃ Sn ₅	6.5×10^{-4}	9.75	9.7	-5.77
Dy ₂ Ir ₃ Sn ₅	5.8×10^{-4}	10.8	10.65	-1.78
Ho ₂ Ir ₃ Sn ₅	1.2×10^{-4}	10.56	10.61	7.33
Er ₂ Ir ₃ Sn ₅	5.1×10^{-4}	9.43	9.59	1.80
Tm ₂ Ir ₃ Sn ₅	9.5×10^{-4}	7.14	7.56	9.01

Table 5.2: R₂Ir₃Sn₅ compounds obtained from the high temperature susceptibility fit to Curie - Weiss relation. μ_{th} is the theoretical free ion value for trivalent rare - earth ions.

5.3.1.2 M-H of R₂Ir₃Sn₅ (R = Ce, Pr, Gd, Tb, Dy, Ho, Er and Tm)

Figure 5.4 and Figure 5.5 depict the magnetization measurements at various temperatures for R₂Ir₃Sn₅. In the case of Ce₂Ir₃Sn₅, at 3 K and 2 K the $M - H$ behavior is linear till 5 T. The magnetization values of Ce₂Ir₃Sn₅ at high fields are quite small presumably due to the presence of Kondo effect, the presence of Kondo effect is further supported by the resistivity data to be discussed in the next section. At higher temperatures (above transition temperature, $T > T_N$), the usual linear behavior in M vs H is consistent with the paramagnetic state of the compound. The magnetization data for Gd₂Ir₃Sn₅ and Tb₂Ir₃Sn₅ depicts “*S-like*” upward curvature indicating the presence of metamagnetic transitions from a state of low magnetization to one of relatively high magnetization. Similar behavior has already been reported in some other Gd and Tb based compounds of the related crystal structure [98, 104]. The magnetization of Dy₂Ir₃Sn₅ at 2 K and 7 K exhibits non linear behavior which suggests that similar magnetic correlation occurs in between these temperature region. The rest of the heavier rare earth based compounds exhibits non linear behavior at low temperatures suggesting antiferromagnetic correlations in this temperature region. The magnetic moment of Ho₂Ir₃Sn₅ sort to saturate, reaching a value of about $7.7 \mu_B/R$ at 5 T which is much lower than the value of $10.0 \mu_B/R$ for Ho³⁺ saturated moment, at large applied field, which indicates possibility for a metamagnetic transition at high fields. The similar effect is noticed in Er₂Ir₃Sn₅ and Tm₂Ir₃Sn₅. The non - linearity in M vs H above T_N in the case of Dy, Ho, Er and Tm indicate the possibility for short - range magnetic correlation (could arise due to splitting

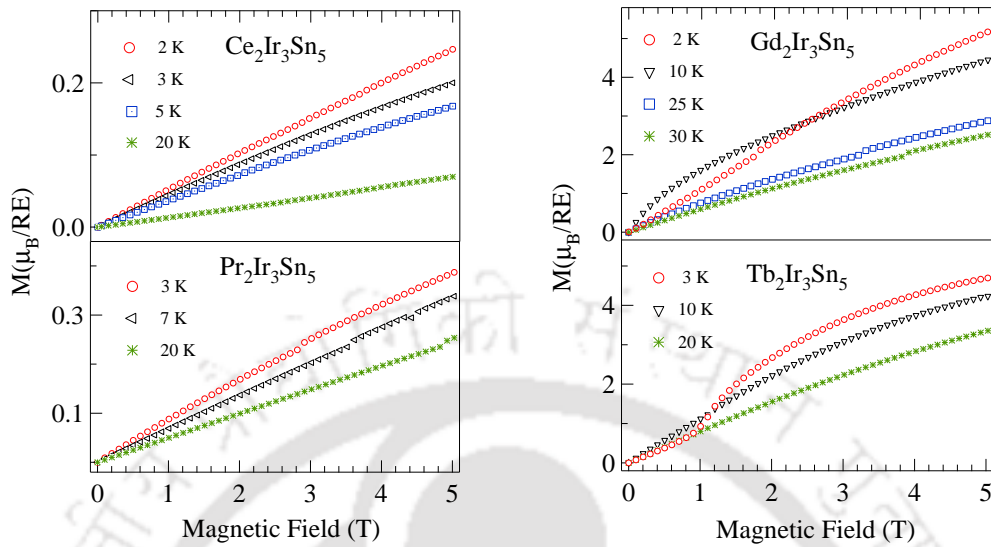


Figure 5.4: Isothermal magnetization measurement of field dependence in $R_2Ir_3Sn_5$ series of compounds with $R = Ce, Pr, Gd$ and Tb .

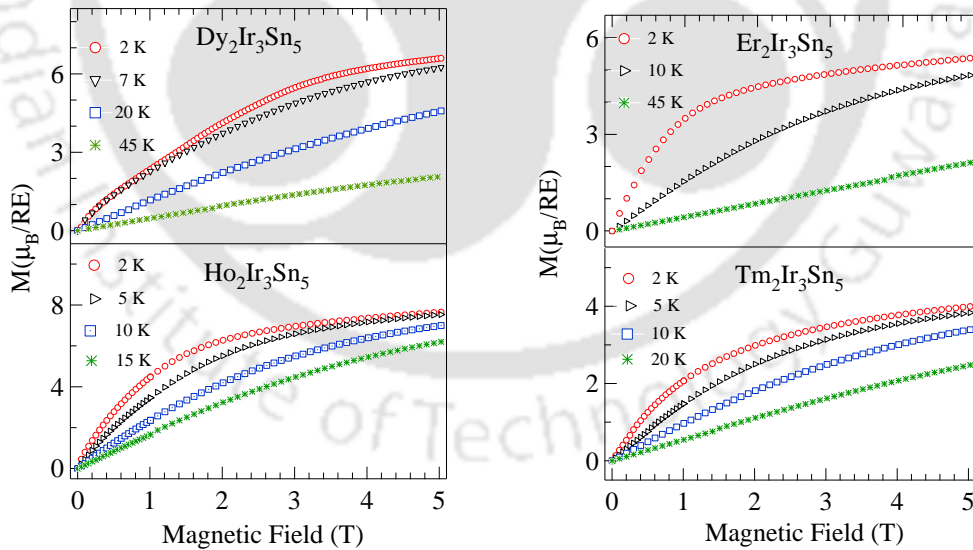


Figure 5.5: Isothermal magnetization measurement of field dependence in $R_2Ir_3Sn_5$ series of compounds with $R = Dy, Ho, Er, Tm$.

of energy levels by crystalline electric field (CEF)) still persists above Neel temperature.

More investigation such as neutron-scattering (elastic and inelastic) measurements are essential to solve the magnetic structures and CEF levels of these compounds.

5.3.2 Resistivity studies of $R_2Ir_3Sn_5$ ($R = La, Ce - Tm$)

The electrical resistivity (ρ) data as a function of temperature in the range 1.8 to 300 K of $R_2Ir_3Sn_5$ ($R = La, Ce - Tm$) are presented in Figure 5.6 and Figure 5.7. The inset shows low temperature ρ [ρ_{mag} for $Ce_2Ir_3Sn_5$] vs T plot of respective compound on an expanded scale. The magnetic contribution is obtained by subtracting the resistivity of $La_2Ir_3Sn_5$ from that of $Ce_2Ir_3Sn_5$. The large value of the residual resistivity is due to the micro-cracks present in the sample. Since the properties of the 2-3-5 stannides are highly anisotropic, single crystals of these samples awaits for complete analysis. The resistivity of $La_2Ir_3Sn_5$ depicts an usual metallic behavior down to 1.8 K in contrast to the other germanides and silicides and other 2-3-5 series [97, 98, 8]. The resistivity of

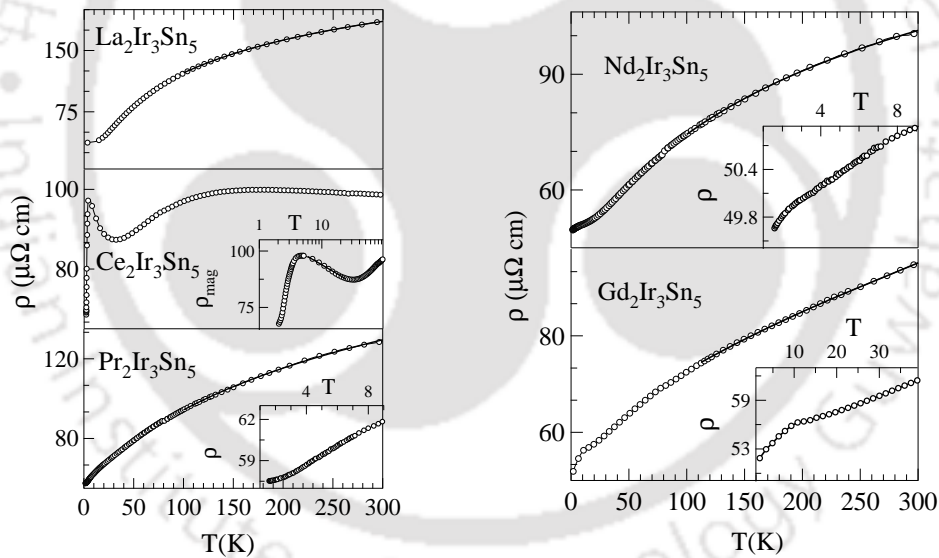


Figure 5.6: The temperature dependence of resistivity (ρ) of $R_2Ir_3Sn_5$ ($R = La - Nd$ and Gd) from 1.8 to 300 K. The inset shows low temperature ρ data. The solid line in the main plots are fit to parallel resistor model.

$Ce_2Ir_3Sn_5$ displays a typical Kondo like response with a minimum (ρ_{min}) around 30 K followed by a maximum of $\rho(T)$ at 4 K indicating the onset of coherence. Subsequently, the resistivity falls sharply below 3 K which clearly exhibits reduction in spin - disorder scattering caused by the antiferromagnetic ordering of the magnetic moments as seen in

susceptibility data. The solid line shown in ρ_{mag} $Ce_2Ir_3Sn_5$ (inset of fig Figure 5.6) is a fit to the relation $\rho_{mag}(T) = \rho_s - C_k \ln(T/T_k)$. This $-\ln T$ behaviour in resistivity data suggests that this is a Kondo system. $Pr_2Ir_3Sn_5$ and $Nd_2Ir_3Sn_5$ do not show any signature of magnetic ordering down to 1.8 K which corroborates the magnetization measurements. The low temperature resistivity data for $Gd_2Ir_3Sn_5$ and $Tb_2Ir_3Sn_5$ reveals the magnetic ordering depicted by a slope change at 5.2 K and 4.7 K, respectively. The plot of the derivative $d\rho/dT$ vs T (not presented here) brings out second anomalies around 10 K and 9.7 K respectively on these compounds as observed in susceptibility data. The changes of the resistivity with temperature for rest of the rare earth compounds (insets in Figure 5.6 and Figure 5.7) manifests clearly the magnetic ordering which matches with susceptibility measurements. The transition temperatures obtained from resistivity measurement is listed in Table Table 5.3 along with those values obtained from susceptibility and heat capacity studies.

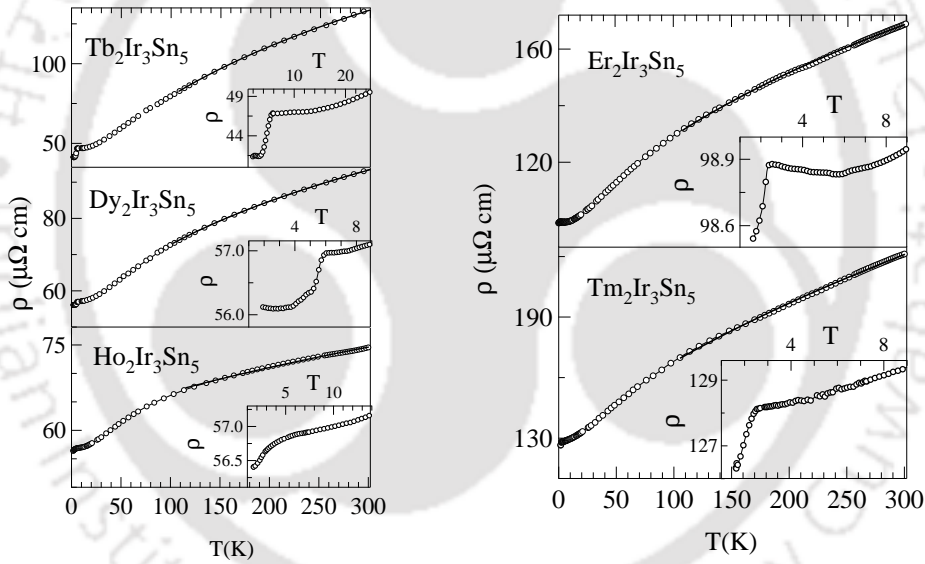


Figure 5.7: The temperature dependence of resistivity (ρ) of $R_2Ir_3Sn_5$ (R = Tb - Tm) from 1.8 to 300 K. The inset shows low temperature ρ data. The solid line in the main plots are fit to parallel resistor model.

In the paramagnetic state, i.e., above magnetic transition temperatures ($T_N < T < 20$ K), the $\rho(T)$ is fitted to power law which can be written as

$$\rho = \rho_0 + aT^n \quad (5.3)$$

The values of ρ_0 , a and n are given in Table 5.4. We obtain a value of $n = 3$ for $La_2Ir_3Sn_5$.

Sample	Resistivity T_N (K)	Susceptibility T_N (K)	Heat capacity T_N (K)
Ce ₂ Ir ₃ Sn ₅	2.5	2.42	2.9
Pr ₂ Ir ₃ Sn ₅	-	-	-
Nd ₂ Ir ₃ Sn ₅	-	-	-
Gd ₂ Ir ₃ Sn ₅	5 , 9.2	3 , 9	3.34 , 9.2
Tb ₂ Ir ₃ Sn ₅	4.7 , 9.73	3.85 , 10	4.9 , 10.11
Dy ₂ Ir ₃ Sn ₅	5.31	5	4.38 , 5.23
Ho ₂ Ir ₃ Sn ₅	2.48	2	<2.5
Er ₂ Ir ₃ Sn ₅	2.2	1.9	<2.5
Tm ₂ Ir ₃ Sn ₅	1.91	1.9	<2.5

Table 5.3: Transition temperatures T_N observed from different measurement techniques.

This value of n agrees with Wilson's $s - d$ scattering model, which predicts a T^3 dependence of resistivity for transition metal alloys below $\theta_D/10$, where θ_D is the Debye temperature. Since the compound Ce₂Ir₃Sn₅ exhibits Kondo effect, we haven't made any attempt for power law fit on Ce₂Ir₃Sn₅. The resistivity of the magnetic rare earth compounds with R = Nd, Dy, Ho and Er show a T^2 dependence in power law fit. For Tb₂Ir₃Sn₅, it exhibits $T^{2.5}$ dependence. However, ρ of both Gd₂Ir₃Sn₅ and Tm₂Ir₃Sn₅ as well as Pr₂Ir₃Sn₅ show a different power law dependence like $T^{1.5}$ and T respectively. At present, we do not understand the reason for this different power law behavior.

Sample	ρ_0 $\mu\Omega$ cm	a $n\Omega$ cm/K ⁿ	n
La ₂ Ir ₃ Sn ₅	37.05	1.05	3
Pr ₂ Ir ₃ Sn ₅	50.87	20.7	1
Nd ₂ Ir ₃ Sn ₅	50.54	5.01	2
Gd ₂ Ir ₃ Sn ₅	55.32	25.01	1.5
Tb ₂ Ir ₃ Sn ₅	46.58	1.03	2.5
Dy ₂ Ir ₃ Sn ₅	56.76	3.02	2
Ho ₂ Ir ₃ Sn ₅	56.74	2	2
Er ₂ Ir ₃ Sn ₅	97.89	21	2
Tm ₂ Ir ₃ Sn ₅	128	40	1.5

Table 5.4: Parameters obtained from power law fit in low temperature resistivity for R₂Ir₃Sn₅.

At high temperatures ($100 \text{ K} < T < 300 \text{ K}$), the resistivity data deviate significantly from the expected linear temperature dependence. Such a deviation from linear temperature dependence has been seen in many alloys and subsequently, it shows a tendency to saturate where the value of ρ becomes sufficiently large. When the mean free path is of the order of a few atomic spacing, the scattering cross section will no longer be linear in the scattering perturbation. Since the dominant temperature - dependent scattering mechanism here is electron-phonon interaction, the ρ will no longer be proportional to the mean -square atomic displacement, which is proportional to T for a harmonic potential. Instead, the resistance will rise less rapidly than T and will show a negative curvature ($d^2\rho/dT^2 < 0$). This behavior was also seen in previous studies on silicides and germanides [105, 106].

The high temperature $\rho(T)$ of these compounds would be treated by well described model, namely as parallel resistor model [107]. In this model, the expression of $\rho(T)$ is given by

$$\frac{1}{\rho(T)} = \frac{1}{\rho_1(T)} + \frac{1}{\rho_{max}}, \quad (5.4)$$

where ρ_{max} is a saturation resistivity which is independent of temperature, and $\rho_1(T)$ is the ideal temperature - dependent resistivity, which can be given by the following expression

$$\rho_1(T) = \rho_0 + C_1 \left(\frac{T}{\theta_D} \right)^5 \int_0^{\theta_D/T} \frac{x^5 dx}{[1 - \exp(-x)][\exp(x) - 1]}, \quad (5.5)$$

where ρ_0 is the residual resistivity and the second term is due to phonon - assisted electron scattering similar to the $s - d$ scattering in transition - metal alloys. $x = h\omega_D/2\pi k_B T$, θ_D is the Debye temperature and C_1 is a numerical constant which describes a temperature independent interaction strength of the conduction electrons with the thermally excited phonons and contains the ionic mass, Fermi velocity, etc. (Equation 5.4) can be derived if we assume that the electron mean free path l is replaced by $l + a$ (a being average interatomic spacing). Such an assumption is reasonable, since infinitely strong scattering can only reduce the electron mean free path to a . Within the framework of Boltzmann transport equation Chakraborty and Allen investigated the consequences of strong electron-phonon interaction. They found that “*nonclassical channels*” opens up due to interband scattering, which accounts for parallel resistor model [108]. The various parameters obtained by fitting the parallel resistor model to the high temperature ($100 \text{ K} < T < 300 \text{ K}$) ρ data of $R_2\text{Ir}_3\text{Sn}_5$ are listed in Table 5.5 and compared with the

θ_D values estimated from heat capacity data.

Sample	ρ_{max} $\mu\Omega$ cm	ρ_0 $\mu\Omega$ cm	C_1 $\mu\Omega$ cm	$\theta_D(\text{fit})$ (K)	$\theta_D(\text{HC})$ (K)
La ₂ Ir ₃ Sn ₅	278	81	1097	180	188
Pr ₂ Ir ₃ Sn ₅	214	106	573	191	189
Nd ₂ Ir ₃ Sn ₅	156	86	554	200	205
Gd ₂ Ir ₃ Sn ₅	236	88	256	260	254
Tb ₂ Ir ₃ Sn ₅	303	60	523	213	217
Dy ₂ Ir ₃ Sn ₅	160	103	144	247	242
Ho ₂ Ir ₃ Sn ₅	137	120	170	274	237
Er ₂ Ir ₃ Sn ₅	318	163	505	190	188
Tm ₂ Ir ₃ Sn ₅	518	198	581	227	215

Table 5.5: $R_2\text{Ir}_3\text{Sn}_5$ series at high temperature ($100 < T < 300$ K) using parallel resistor model. $\theta_D(\text{HC})$ is observed from heat capacity studies.

5.3.3 Heat capacity studies of $R_2\text{Ir}_3\text{Sn}_5$ ($R = \text{La} - \text{Tm}$)

The temperature dependence of the the heat capacity (C_P) and magnetic entropy (S_{mag}) from 1.8 to 30 K for $R_2\text{Ir}_3\text{Sn}_5$ ($R = \text{La} - \text{Tm}$) are shown in Fig Figure 5.8 and Figure 5.9. The inset shows C_{mag}/T (C_P/T for La₂Ir₃Sn₅) vs T^2 at low temperature to illustrate the onset of bulk magnetic ordering in these samples. The temperature dependence of heat capacity (C_P) for $R_2\text{Ir}_3\text{Sn}_5$ ($R = \text{Ce} - \text{Tm}$) is fitted to the expression,

$$C_{Tot} = C_{elec} + C_{Ph} = \gamma T + \beta T^3, \quad (5.6)$$

where γ is due to the electronic contribution and β is due to the phononic contribution. From the β value, we can estimate the value of Debye temperature θ_D by using the relation,

$$\theta_D = \left(\frac{12\pi^4 N r k_B}{5\beta} \right)^{1/3} \quad (5.7)$$

where N is the Avogadro's number, r is the number of atoms per formula unit and k_B is the Boltzmann's constant. The value of θ_D calculated from C_P data are included in Table 5.5 to alleviate the comparison with Debye temperatures from high temperature

resistivity data. The parameters obtained from the analysis of heat capacity measurements can be found in Table 5.6 where we have listed values of the ordering temperature T_N , entropy $S_{mag}(T_N)/R$, $S_{mag}(30K)/R$ for different members of the $R_2Ir_3Sn_5$ series, along with expected value of entropy of trivalent rare earth ion $R \ln(2J + 1)$.

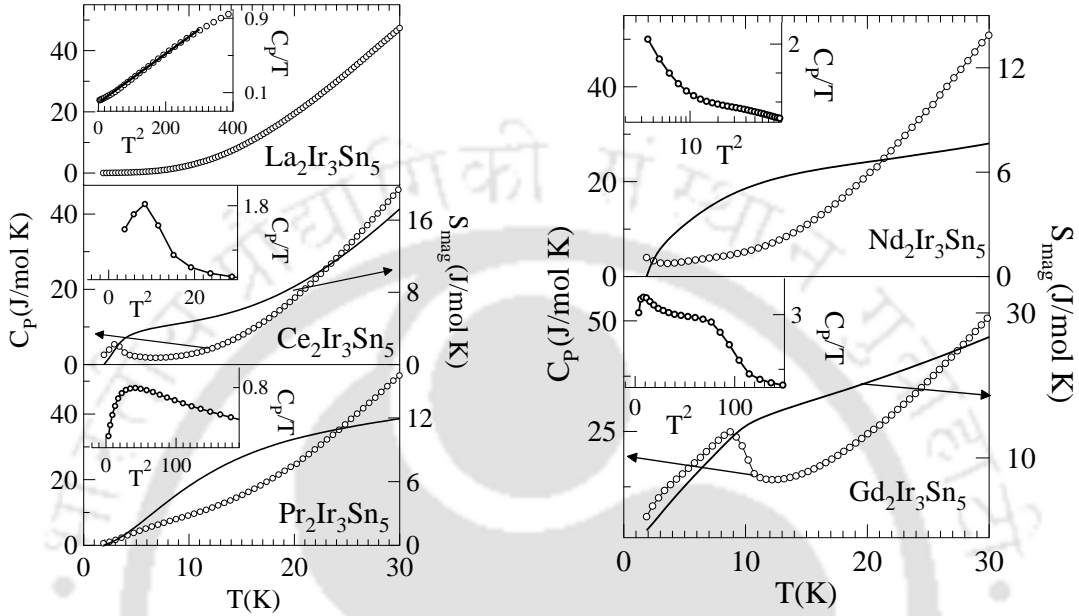


Figure 5.8: Temperature dependence of the heat capacity [(C_P) , marked by $(-\circ-)$] of $R_2Ir_3Sn_5$ ($R = La - Nd$ and Gd) from 1.8 to 30 K. The calculated entropy S_{mag} [solid line] (after subtractions of lattice contribution from C_P of $La_2Ir_3Sn_5$) is shown in the right hand side of the same figure. The inset shows the low temperature C_{mag}/T vs T^2 data.

The fit to C_P/T vs T^2 for $La_2Ir_3Sn_5$ sample (see the inset) estimate the value of Sommerfeld's coefficient γ as 9.4 mJ/mol K^2 , which agrees closely with that observed for the free electrons of the mass of La atom [109]. For $Ce_2Ir_3Sn_5$, the large peak in C_{mag}/T at 2.9 K confirms the bulk magnetic ordering of Ce^{3+} moments. The fit to heat capacity data using Equation 5.6 in the temperature range from 10 K to 20 K yielded the value of γ as 58 mJ/mol K which suggests the $Ce_2Ir_3Sn_5$ is a moderate heavy fermion antiferromagnet.

The temperature dependence of C_P for $Pr_2Ir_3Sn_5$ and $Nd_2Ir_3Sn_5$ reveals no bulk magnetic ordering down to 1.8 K, in these samples. The C_{mag} , derived by subtracting the lattice contribution from C_P , show a broad hump in $Pr_2Ir_3Sn_5$ and $Nd_2Ir_3Sn_5$ around 8 K and 10 K respectively which demonstrate Schottky type anomaly indicating the

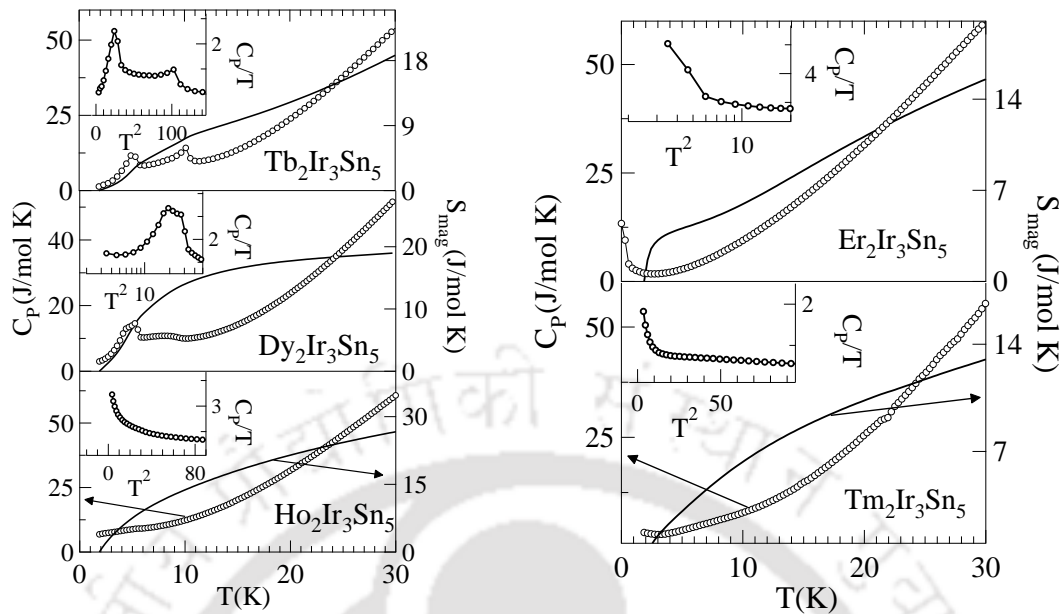


Figure 5.9: Temperature dependence of the heat capacity [C_P], marked by $(-\circ-)$ of $R_2\text{Ir}_3\text{Sn}_5$ ($R = \text{Dy} - \text{Tm}$) from 1.8 to 30 K. The calculated entropy S_{mag} [solid line] (after subtraction of lattice contribution from C_P of $\text{La}_2\text{Ir}_3\text{Sn}_5$) is shown in the right hand side of the same figure. The inset shows the low temperature C_{mag}/T vs T^2 data.

presence of low - lying excited crystal electric field (CEF) level becoming populated with the increase of temperature. The low value of estimated entropy at 30 K as well as the large value of Sommerfeld coefficients may be accounted, either by the CEF effects or by short - range magnetic correlations. The C_{mag} of $\text{Gd}_2\text{Ir}_3\text{Sn}_5$ displays transitions at 4.32 K and 10.21 K indicating bulk magnetic ordering of Gd^{3+} spins which is in agreement with the susceptibility and resistivity data. It is conjectured that second anomaly at 4.32 K may be associated with the moment reorientation effect as noticed in other intermetallic compounds [97, 110, 111]. The entropy at 30 K is found to be 3.19 R which is more than the expected value of $R \ln(2J + 1)$. Even though $\text{La}_2\text{Ir}_3\text{Sn}_5$ and $\text{Gd}_2\text{Ir}_3\text{Sn}_5$ crystallizes in the orthorhombic structure, their space groups are different. Hence, the subtraction of the phonon contribution from $\text{Gd}_2\text{Ir}_3\text{Sn}_5$ using the data of $\text{La}_2\text{Ir}_3\text{Sn}_5$ may not be appropriated and have been underestimated. These has resulted in the large magnetic entropy at 30K.

The C_{mag} data of $\text{Tb}_2\text{Ir}_3\text{Sn}_5$ and $\text{Dy}_2\text{Ir}_3\text{Sn}_5$ reveal two bulk magnetic transitions. The transition for $\text{Tb}_2\text{Ir}_3\text{Sn}_5$, occurs at 4.9 K and 10.2 K which upholds results from the susceptibility and resistivity data. The entropy at 30 K is nearly equal to the expected

Sample	T_N (K)	$S_{mag}(T_N)/R$	J	$\ln(2J+1)$	$S_{mag}(30)/R$	B_2^0 (K)
Ce ₂ Ir ₃ Sn ₅	2.9	0.35	$\frac{5}{2}$	1.79	1.89	-
Pr ₂ Ir ₃ Sn ₅	-	-	4	2.19	1.43	3.2
Nd ₂ Ir ₃ Sn ₅	-	-	$\frac{9}{2}$	2.3	0.92	1.9
Gd ₂ Ir ₃ Sn ₅	3.34 , 9.2	1.6	$\frac{7}{2}$	2.08	3.19	-
Tb ₂ Ir ₃ Sn ₅	4.9 , 10.11	1.4	6	2.57	2.13	-
Dy ₂ Ir ₃ Sn ₅	4.38 , 5.23	0.9	$\frac{15}{2}$	2.77	2.3	1.2
Ho ₂ Ir ₃ Sn ₅	< 2.5	1.09	8	2.83	3.2	2.7
Er ₂ Ir ₃ Sn ₅	< 2.5	1.14	$\frac{15}{2}$	2.77	1.9	4.5
Tm ₂ Ir ₃ Sn ₅	< 2.5	0.45	6	2.56	1.56	2.3

Table 5.6: Parameters obtained from heat capacity studies of $R_2Ir_3Sn_5$.

value of free ion. For Dy₂Ir₃Sn₅, the main transition at 5.23 K is consistent with resistivity and susceptibility measurement. The second anomaly at 4.38 K is observed only in heat capacity data, which may originate due to successive spin reorientation effects. Schottky anomaly is depicted by a broad hump around 15 K.

The heat capacity data for Ho₂Ir₃Sn₅, Er₂Ir₃Sn₅ and Tm₂Ir₃Sn₅ show an upturn at low temperature below 4 K which continues down to the lowest measured temperature, and this confirms the onset magnetic ordering of R³⁺ moments which was seen in susceptibility and resistivity. Schottky type anomaly suggests CEF effects in these compounds. All the heavier rare earths depicts low value of entropy at 30 K and very large γ , which indicates strong influence of hybridization in these compounds.

5.3.4 Crystal - field analysis

The crystalline electric field is derived from the symmetry of environment of the neighbouring ions (ligands) in the crystal. The crystal-field potential due to the surrounding ions at the location of the k^{th} unpaired electron of the magnetic ion, is

$$V_k(\vec{r}_k) = |e| \sum_j \frac{Z_j}{|\vec{R}_j - \vec{r}_k|} \quad (5.8)$$

where $|e|$ is the absolute value of the electron charge. The charge of the j^{th} ligand ion is Z_j and \vec{R}_j and \vec{r}_k are the positions of the j^{th} ligand ion and k^{th} unpaired electron, respectively, where the center of the magnetic ion is taken as the origin. The summation

is carried out over all ligand ions in the crystal.

The crystal-field Hamiltonian is obtained from Equation 5.8 by summing over all n_f unpaired electrons.

$$H_{CEF} = -|e| \sum_{k=1}^{n_f} V_k(\vec{r}_k) \quad (5.9)$$

In the Steven's operator formalism the Equation 5.11 can be written as,

$$H_{CEF} = \sum_{n=0}^{\infty} \sum_{m=-n} B_n^m O_n^m \quad (5.10)$$

where B_n^m and O_n^m are crystal field parameter (which measure the strength of crystal field) and the Steven's operators (in terms of angular momentum operators) respectively. In the orthorhombic symmetry, the Hamiltonian for the crystalline electric field is,

$$\mathcal{H}_{CEF} = B_2^0 O_2^0 + B_2^2 O_2^2 + B_4^0 O_4^0 + B_4^2 O_4^2 + B_4^4 O_4^4 + B_6^0 O_6^0 + B_6^2 O_6^2 + B_6^4 O_6^4 + B_6^6 O_6^6 \quad (5.11)$$

We review the effect of the crystal fields on thermodynamic properties (heat capacity and magnetic susceptibility) of $R_2Ir_3Sn_5$ compounds, which has revealed signatures of CEF at low temperatures. Particularly in the case of Ce system, the entropy and the magnetization is considerably low which signals the CEF and Kondo effect. Hence, we provide an analysis of the magnetic interaction in terms of a combined crystal field and molecular field approach. Figure 5.10 depicts the magnetic contribution of heat capacity of $R_2Ir_3Sn_5$ is isolated by subtracting the heat capacity of the $La_2Ir_3Sn_5$. The Hamiltonian of a system for determining the magnetic properties of the material, consist of spin - orbit coupling, crystalline electric field, Zeeman and exchange field terms, can be written as:

$$\mathcal{H} = \lambda \vec{L} \cdot \vec{S} + \mathcal{H}_{CEF} + \beta \vec{H} \cdot (\vec{L} + 2\vec{S}) + \mathcal{H}_{ex}, \quad (5.12)$$

It is diagonalized within the substates arising from the lowest multiplets of R^{3+} ($R = Pr, Nd, Dy, Ho, Er$ and Tm) to obtain the energy and eigenfunctions of respective ions. In $R_2Ir_3Sn_5$ compounds, R^{3+} ions occupy two site on 4a Wyckoff position in the orthorhombic $Y_2Rh_3Sn_5$ - type structure which belongs to $Cmc2_1$ space group. In the orthorhombic symmetry of $R_2Ir_3Sn_5$, the effect of crystal structure on f electrons are characterized by nine real parameters. The limited experimental data prevented us from the independent determination of all the crystal - field parameters unambiguously. In order to keep the

number of parameters to a minimum, we retained the second order axial distortion term and fourth order cubic terms only. The CEF Hamiltonian for orthorhombic symmetry, after retaining only these terms, can be expressed as

$$\mathcal{H}_{\text{CEF}} = B_2^0 O_2^0 + B_2^2 O_2^2 \quad (5.13)$$

B_2^0 and B_2^2 determine the strength of the crystal field due to axial and rhombic distortion. The diagonalization of the above Hamiltonian together with other detailed calculation can be done by using the standard procedure. By diagonalizing the CEF Hamiltonian, one can estimate consistent sets of energy eigen values and eigen vectors by which the explicit determination of heat capacity (using (Equation 5.14)) is possible. As revealed in other 2-3-5 compounds with similar crystal structure, the parameter B_2^2 is negligible compared to the B_2^0 [112]. Hence in our analysis we have used B_2^0 as the only parameter to determine the strength of the crystalline electric field. The schottky equation for the heat capacity in presence of crystal field effects is given by,

$$C_{sch} = \left[\frac{R \sum_i g_i e^{-E_i/T} \sum_i g_i E_i^2 e^{-E_i/T} \left(\sum_i g_i E_i e^{-E_i/T} \right)^2}{(k_B T)^2 \left(\sum_i g_i e^{-E_i/T} \right)^2} \right] \quad (5.14)$$

where R is a gas constant, E_i is the crystalline field energy levels in units of temperature and g_i is the degeneracy of the energy levels. The estimation of CEF parameters is made by least-square fitting of the experimental heat capacity data using (Equation 5.14). The fit to the Schottky anomaly as well as to the total entropy of the magnetic heat capacities of $R_2Ir_3Sn_5$ (R = Pr, Nd, Dy, Ho, Er and Tm) is displayed in Figure 5.10. The crystal field split energy levels obtained from CEF parameters for one of the rare earth sample $Pr_2Ir_3Sn_5$ is also shown in Figure 5.10. The summarized result from this analysis are listed in Table 5.7. In all the compounds, we found that the best fit was obtained for the positive crystal field parameter B_2^0 .

The magnetic susceptibility of $R_2Ir_3Sn_5$ is analyzed on the basis of CEF model including the exchange parameter. The exchange interaction, in the molecular field framework above the Neel temperature is given by,

$$\mathcal{H}_{ex} = -2zJ \langle \vec{S} \rangle \cdot \vec{S} \quad (5.15)$$

Here z is the number of nearest equivalent neighbors interacting with the exchange interaction J , and $\langle \vec{S} \rangle$ is the expectation value of the spin operator \mathbf{S} . An iterative procedure were used to calculate $\langle \vec{S} \rangle$ self-consistently. The details of this procedure were discussed by Marathe and Mitra [113].

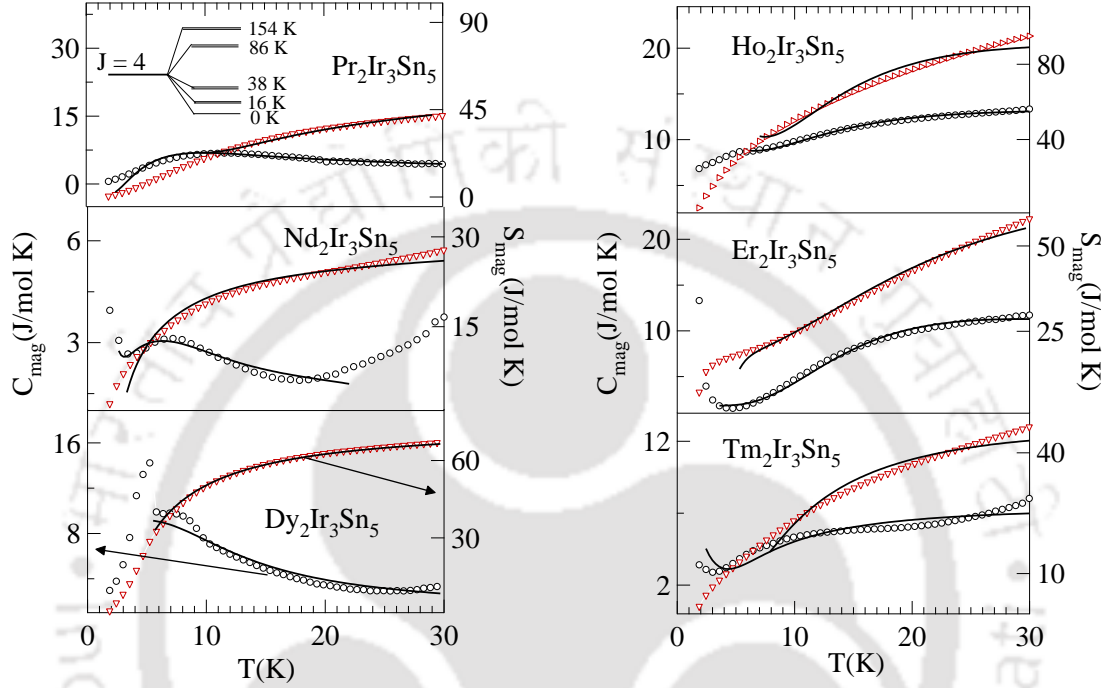


Figure 5.10: Plot of the magnetic contribution to the heat capacity (C_{mag}) and the entropy (S_{mag}) vs T of $R_2Ir_3Sn_5$ ($R = Pr, Nd, Dy, Ho, Er$ and Tm). The solid line are fit to the CEF model.

Sample	J	B_2^0	λ	zJ
			(mol/emu)	
$Pr_2Ir_3Sn_5$	4	3.2	9.76	-0.3
$Nd_2Ir_3Sn_5$	$\frac{9}{2}$	1.9	3.1	-0.28
$Dy_2Ir_3Sn_5$	$\frac{15}{2}$	1.2	5	-2.7
$Ho_2Ir_3Sn_5$	8	2.7	3	-2.6
$Er_2Ir_3Sn_5$	$\frac{15}{2}$	4.5	4	-2.07
$Tm_2Ir_3Sn_5$	6	2.3	6.54	-1.24

Table 5.7: Parameters obtained from CEF fit.

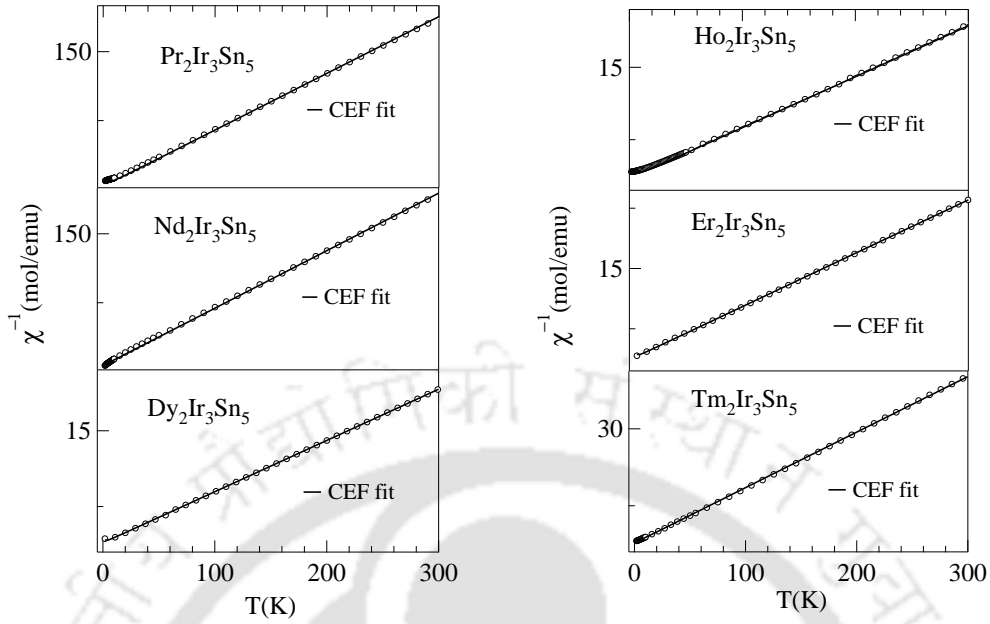


Figure 5.11: Variation of the inverse susceptibility of $R_2Ir_3Sn_5$ ($R = Pr, Nd, Dy, Ho, Er$ and Tm) series in a field of 4 kOe from 2 to 300 K. The solid lines are fits to the CEF model.

In order to show CEF effects on the susceptibility, we have used Van Vleck's susceptibility expression given by C. Cascales *et.al* [114] as follows:

$$\chi_{\text{CEF}} = N\beta^2 \sum_a \left[\frac{\langle \phi_a | \mathcal{H} | \phi_a \rangle^2}{k_B T} - 2 \sum_b \frac{\langle \phi_a | \mathcal{H} | \phi_b \rangle \langle \phi_b | \mathcal{H} | \phi_a \rangle}{E_a - E_b} \right] \times \frac{\exp(-E_a^0/k_B T)}{\sum_a \exp(-E_a^0/k_B T)} \quad (5.16)$$

in which N is the Avogadro's number, β the Bohr magneton, k_B the Boltzmann constant, E and ϕ the non-perturbed eigenvalues and wave functions, respectively, described on the $SLJM_J$ basis. In a fitting procedure the susceptibility has been taken as the average and corrected by a molecular field constant λ , i.e.,

$$\frac{1}{\chi_{\text{exp}}} = \frac{1}{\chi_{\text{CEF}}} - \lambda \quad (5.17)$$

where $\lambda = Jz / (g_J \mu_B)^2$ which parametrizes the strength of the molecular field as a function of the magnetization. We have fixed the crystal-field parameter B_2^0 obtained from an analysis of the heat-capacity data, and varied the exchange parameter zJ so as to obtain

the best fit to the experimentally observed magnetic susceptibility data. The calculated magnetic susceptibility (χ_{CEF}) from (Equation 5.17) is in good agreement with the experimentally observed data of $R_2Ir_3Sn_5$ as shown in Figure 5.11. The estimated value of zJ and molecular field constant λ for various $R_2Ir_3Sn_5$ compounds are listed in Table 5.7.

5.4 Discussion

In this section we will make an attempt to understand the temperature dependence of the measured physical properties and the models which we have used to understand their behavior. We begin with the results derived from transport measurement. In magnetically ordered materials the temperature dependent part of the resistivity at low temperature is mainly due to electron- electron scattering, electron- phonon scattering and electron-spin wave scattering phenomena. In Table 5.4, we see T^2 dependence of certain compounds which suggests that the spin fluctuation play an important role in scattering conduction electrons at these temperatures. In the case of $Pr_2Ir_3Sn_5$ a linear temperature dependence is observed. This type of linear temperature dependence is also observed in other Pr based compounds [115]. For $Tb_2Ir_3Sn_5$, we find a marked deviation from the T^2 law with n being equal to 2.5 and the reasons are not well understood at present. $Gd_2Ir_3Sn_5$ and $Tm_2Ir_3Sn_5$ exhibit $n = 1.5$ power law dependence which may be described in the framework of the spin fluctuation theories of Moriya, Takimoto and Lonzarich [116, 117]. Based on this model, resistivity in the vicinity of three dimensional antiferromagnetic transition scales as $T^{3/2}$ and scales as $T^{5/3}$ in the neighborhood of ferromagnetic transition [118]. It is important to mention that the effect of magnetic correlation in long range order and disorder plays an important role in spin fluctuation model.

At higher temperature above 100 K the $\rho(T)$ dependence is not strictly linear, but has a small negative curvature. This deviation from the Bloch-Gruneisn law is attributed to the shape of the conduction band density of d-states and larger $s-d$ type scattering. The high-temperature dependence of ρ is fitted to the parallel resistor model (see Table 5.5) and estimated value of θ_D agrees with those obtained from heat capacity data for almost all compounds (magnetic or nonmagnetic) of the series $R_2Ir_3Sn_5$. The values of ρ_{max} vary considerably across the series and are quite high in most cases. The exact origin of the ρ_{max} is still not understood properly. In a recent semi classical theory the resistivity is related to the mean-free path λ by the relation $\rho = 3\pi h/e^2 k_F^2 \lambda$. The minimum mean free path is taken as the interatomic distance based on the assumption that the electrons can be scattered at most by every atom. This leads to the saturation resistivity or the

maximum resistivity ρ_{max} , in this scheme. This value of ρ_{max} is called the loffe-Regel resistivity and for most compounds its value is about 150 - 200 $\mu\Omega$ cm. As noticed from Table 5.5 that ρ'_0 's for our samples is quite large, which is also seen in some recent systems with large resistivity, which saturate at values much larger values than the loffe-Regel resistivity [98]. Thus it is clear that both low temperature and high temperature behavior of the transport properties for $R_2Ir_3Sn_5$ compounds require more investigations for better understanding.

We now turn our attention to some of the systematic trends observed in magnetic properties at low and high temperatures. The high temperature susceptibility data for all the compounds are fitted to modified Curie Weiss law. From Table 5.2, it can be seen that the temperature independent susceptibility χ_0 is non-negligible for some cases ($Ce_2Ir_3Sn_5$) which possibly indicates a large density of states at the Fermi level $N(E_F)$. Even in the presence of strong hybridization of $4f$ orbitals of Ce and the conduction electrons, which leads to Kondo effect in resistivity, we observe large value of θ_P (-37.5 K) in $Ce_2Ir_3Sn_5$ indicating the presence of antiferromagnetic correlations. For the rest of the compounds the strength of the interactions between the RE^{3+} ions are similar. We wish to recall here that the polycrystalline data is influenced by the overall behavior of the compound including the anisotropy [119]. The data begins to deviate from the Curie-Weiss behavior at lower temperatures which was explained by CEF. The multiple anomalies in susceptibility and the deviation from linear behavior in magnetization curve below T_N for $Gd_2Ir_3Sn_5$ and $Tb_2Ir_3Sn_5$ can be attributed either to a change in the magnetic structure or to a manifestation of a small anisotropy via spin flop phenomena.

We discuss the nature of the ground state of the energy level of the rare earth ions in these materials on the basis of their magnetic entropy. In this discussion, where double magnetic transition are observed, we consider the value of entropy at the higher T_N as the difference between the $S_{mag}(T_{N1})$ and $S_{mag}(T_{N2})$ is about 1 J/mol K. The $S_{mag}(T_N)$ for $Ce_2Ir_3Sn_5$ reaches to the value of 0.35 R ($\approx 50\% R \ln 2$) and then approaches 1.89 R ($\approx R \ln(2J + 1)$) at 30 K which indicate that doublet ground states dominate the low temperature properties of this compound, which ties in with the knowledge that Ce is a Kramer's ion. The value of entropy at 30 K for $Pr_2Ir_3Sn_5$ (1.43R $\approx R \ln 4$) and $Nd_2Ir_3Sn_5$ (0.92R $\approx R \ln 3$) which is much less than the expected value, $R \ln(2J + 1)$. $Pr_2Ir_3Sn_5$ exhibit singlet ground state arising from CEF splitting of $(2J + 1)$ levels of non-Krammer's Pr^{3+} ion whereas the Krammer's Nd^{3+} ions for $Nd_2Ir_3Sn_5$ exhibit doublet ground state, even though specific heat shows no signature of phase transition till the lowest available temperature. In the case of $Gd_2Ir_3Sn_5$, where no crystal field effects is present, S_{mag} at T_N

($1.6R \approx R \ln 5$) is less than the expected total entropy $2.08R$ for Gd^{3+} ion. But the value of entropy gradually increases above T_N and at 30 K it is $3.19R$. The entropy for $Tb_2Ir_3Sn_5$ reaches a value of $1.4R$ ($\approx R \ln 4$) at T_N which indicate that the ground state is a quartet for this compound. The full entropy is not released at 30 K in $Dy_2Ir_3Sn_5$, $Er_2Ir_3Sn_5$ and $Tm_2Ir_3Sn_5$ compounds indicating that we need to go further high temperatures to access all the higher energy levels created by the CEF. For $Ho_2Ir_3Sn_5$, the slightly higher value of entropy at 30 K from the expected $R \ln (2J + 1)$ value suggests the possibility of inclusion of contribution to the magnetization from the transition element. From crystal field analysis, we found that the ground state of Dy and Er compounds are doublet while $Tm_2Ir_3Sn_5$ and $Ho_2Ir_3Sn_5$ shows singlet ground state.

We have determined magnetic ordering temperatures for $R_2Ir_3Sn_5$ using ρ , χ , and C_P measurements (see Table 5.3). Both Gd and Tb show multiple transitions in all measurements whereas Dy compound exhibits multiple orderings only in heat capacity data. For the purpose of analysis, we have considered transition temperatures obtained from the dc susceptibility measurements. In general, the antiferromagnetic ordering temperature T_N is given by [120],

$$T_N = \theta_P = \frac{3\pi n^2}{k_B E_F} J_{sf}^2 (g_J - 1)^2 J (J + 1) \times \sum_{i \neq 0} F(2k_o R_{O_i}) \cos(k_o \cdot R_{O_i}) \quad (5.18)$$

where E_F is the Fermi energy, J_{sf} is the exchange integral, k_o is the propagation vector of spins, R_{O_i} is the distance between the central ion O with its nearest neighbors i , and n is the density of conduction electrons. $F(x)$ is the Ruderman-Kittel-Kasuya-Yosida (RKKY) interaction, and is given by

$$F(x) = \frac{[\sin(x) - x \cos(x)]}{x^4} \quad (5.19)$$

Normally, if CEF effects are not taken into account, the T_N of rare -earth members of the series are expected to follow the well-known de Gennes scaling [121] as $(g_J - 1)^2 J (J + 1)$ where g_J is the Lande g factor and J is the total angular momentum of the local moment. If the angular momentum (L) is quenched then T_N is expected to scale as $S(S + 1)$. Figure 5.12 depicts the comparison of T_N for those rare earth compounds which undergo magnetic ordering (normalized to T_N value of Gd) with those expected on the basis of de Gennes scaling $(g_J - 1)^2 J (J + 1)$ (solid line) as well as spin quantum number $S(S + 1)$ (dashed line). It is evident that the ordering temperature of $Ce_2Ir_3Sn_5$ and $Tb_2Ir_3Sn_5$ are anomalously large compared to both de Gennes scaling $(g_J - 1)^2 J (J + 1)$

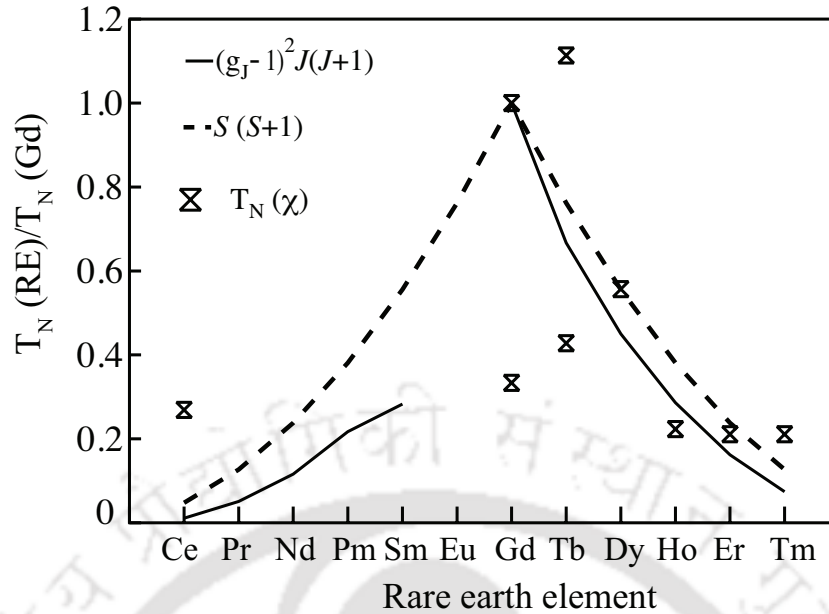


Figure 5.12: Plots of the ordering temperature of the compounds of the series $R_2Ir_3Sn_5$ (R = Ce - Nd, Gd - Tm) normalized to the T_N value for Gd. The dashed lines is the theoretical de Gennes scaling with only spin quantum number and the solid lines is related to de Gennes scaling with total angular momentum

and $S(S+1)$ while T_N 's for rest of the compounds follow the scaling curve of spin quantum number $S(S+1)$ better than de Gennes scaling $(g_J - 1)^2 J(J+1)$. It implies that the magnetic transitions occurs not solely due to RKKY interaction. It is well known that the CEF (in the case of doublet ground state) can enhance the magnetic transition temperature and this could in principle account for the difference between the observed data and de Gennes scaling [122]. However, it can also suppress the transition when singlet ground states are involved and the exchange interaction is weak. But we believe that the reason for the discrepancy between observed T_N and that found from de Gennes scaling is not solely due to CEF.

5.5 Summary

In this chapter, we have synthesized rare earth intermetallic compounds of the series $R_2Ir_3Sn_5$ with R = La, Ce - Nd, Gd - Tm. All the compounds containing magnetic rare earth elements show antiferromagnetic ordering with the exception of $Pr_2Ir_3Sn_5$ and $Nd_2Ir_3Sn_5$ which do not show any transition down to 1.8 K. Among those, $Gd_2Ir_3Sn_5$, $Tb_2Ir_3Sn_5$ and $Dy_2Ir_3Sn_5$ exhibit multiple transitions. We have observed that Curie-

Weiss fit to $R_2Ir_3Sn_5$ give an estimated effective moment μ_{eff} close to the free ion R^{3+} values. The obtained value of θ_D from parallel resistor model do agree well with those obtained from heat capacity data. Most of the compounds belonging to $R_2Ir_3Sn_5$ series exhibit expected T^2 power dependence the resistivity data. A simple analysis of crystal-field model is proposed to account for the contribution to the magnetic entropy and susceptibility of magnetic-rare-earth samples of this series.





Chapter 6

Transport and Magnetic properties of $\text{Ce}_2\text{Ir}_3\text{Sn}_5$ single crystal

6.1 Introduction

Studies of many the rare-earth intermetallic compounds, particularly the Ce-based compounds, have led to the discovery of unusual properties at low temperatures such as Kondo effect, valence instabilities, heavy fermion behavior, coexistence of mixed valence and superconductivity and so on [97, 123, 124, 125]. Such a variety of phenomena arises because of the fact the strength of hybridization can be varied across a very wide range. In addition to this, the presence of crystalline electric field (CEF) in majority of the compounds lifts the degeneracy of the ground state to yield a Kramer-type doublet. Moreover, the trivalent Ce-ion ($4f^1$) marks the beginning of the filling of the $4f$ -shell. It is well known that the anomalous behavior of Ce-based intermetallics, and especially the Kondo effect, is closely connected with the presence of a $4f$ level close to the Fermi level which produces large resonance-scattering effect. [2, 126]. In view of this rather unique features of the Ce-ions, synthesis of new Ce-based intermetallics and investigations of their magnetic properties has always been of considerable interest [127, 128]. In this chapter, we present the synthesis of single crystal of $\text{Ce}_2\text{Ir}_3\text{Sn}_5$ and observed the interesting properties, such as, transport, magnetic and thermal properties.

6.2 Experiment

For the sake of completeness, we briefly reiterate the procedure of synthesis here. $\text{Ce}_2\text{Ir}_3\text{Sn}_5$ Single-crystal has been grown in a tetra-arc furnace using a modified Czochralski technique. The purity of the elements were, Ce: 99.999%; Ir: 99.99%; Sn: 99.999%. The stoichiometric ratio of the elements were taken separately to make a 12 g (polycrystal) melt in a tetra-arc furnace. A thin tungsten seed rod was immersed into the melt and pulled at a speed of 11 mm/h in pure and dry argon atmosphere. After confirming the phase homogeneity of the grown crystal by using powder x-ray diffraction, we used the first grown single crystal rod as a seed in order to synthesize good quality single crystals of $\text{Ce}_2\text{Ir}_3\text{Sn}_5$. The as-grown ingot was approximately 2-3 mm in diameter and 6 cm in length. The magnetic measurements were performed in a commercial superconducting quantum interference device (SQUID) magnetometer (MPMS5, Quantum Design, USA). The temperature dependence of electrical resistivity was measured using a standard dc four probe technique. The heat-capacity measurement was performed using the physical properties measurement systems (PPMS).

6.3 Results & Discussion

1.3.1 X-ray studies

The samples have been analyzed by EDAX to prove its 2-3-5 stoichiometry. The single crystallinity has been verified by x-ray Laue diffraction. The as-grown single crystal and the observed and simulated Laue pattern of an oriented crystal are shown in Figure 6.1. In order to confirm the phase homogeneity of the compounds with proper crystallographic and lattice parameters, a Reitveld analysis of the observed x-ray pattern was done using the FULLPROF program as shown in Figure 6.2 [78]. It was found that $\text{Ce}_2\text{Ir}_3\text{Sn}_5$ adopts orthorhombic $\text{Y}_2\text{Rh}_3\text{Sn}_5$ type crystal structure with space group $Cmc2_1$. The lattice parameters obtained from the Rietveld analysis for $\text{Ce}_2\text{Ir}_3\text{Sn}_5$ are $a = 4.486 \text{ \AA}$, $b = 26.463 \text{ \AA}$ and $c = 7.242 \text{ \AA}$ which are in close agreement earlier reported polycrystalline result. For anisotropic thermal and magnetic measurements, the single crystals were oriented along the principle crystallographic directions using back-reflection Laue diffraction method. The samples were cut to the required size by using spark erosion cutting machine.

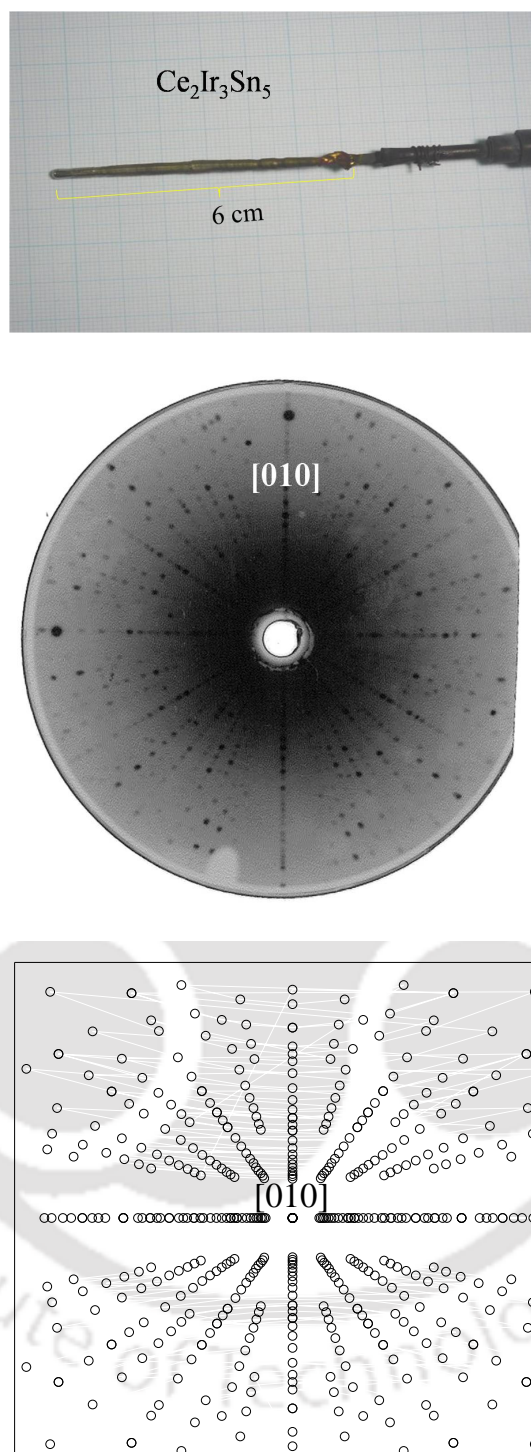


Figure 6.1: The as-grown single crystal and Laue pattern of $\text{Ce}_2\text{Ir}_3\text{Sn}_5$ along the $[010]$ direction. Right figure shows simulated pattern of Laue picture along the $[010]$ axis.

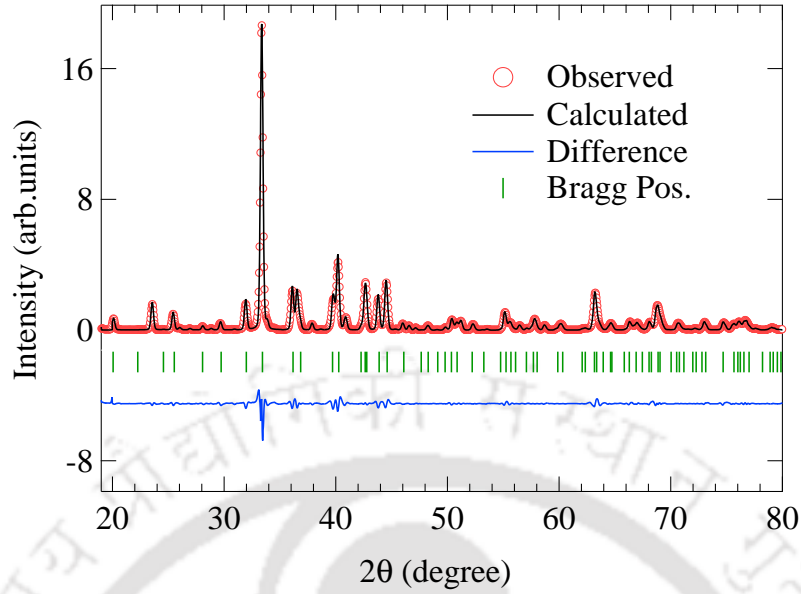


Figure 6.2: Powder x-ray diffraction data of the $\text{Ce}_2\text{Ir}_3\text{Sn}_5$. The solid line is the simulated data using FULLPROF (Reitveld Program).

6.3.1 Resistivity studies

The dc electrical resistivity, measured parallel to [100], [010] and [001] directions, in the temperature range between 1.8 and 300 K is shown in Figure 6.3. In Figure 6.3(a), the resistivity of $\text{Ce}_2\text{Ir}_3\text{Sn}_5$ displays a typical kondo-type response with a minimum (ρ_{min}) around 30 K followed by a maximum of $\rho(T)$ at around 3.6 K. Subsequently, $\rho(T)$ falls sharply below 3.6 K due to the onset of coherence. The increase in the electrical resistivity at low temperatures can be attributed to the presence of kondo-type interaction. With further decrease in temperature below 3.6 K, the resistivity changes its slope and drops due to the reduction in spin-disorder scattering, caused by the antiferromagnetic ordering of the magnetic moments, which is in agreement with the susceptibility data. As we can see from Figure 6.3 the absolute value of electrical resistivity at 300 K is 87, 81 and 158 $\mu\Omega\text{cm}$, respectively, for the current density J parallel to the [100], [010] and [001] directions and at 3.6 K is 70, 104 and 154 $\mu\Omega\text{cm}$ for J parallel to the [100], [010] and [001] directions respectively. Hence the residual resistivity ratio is of the order of unity along all the directions.

Figure 6.3(b) shows a semi-logarithmic scale of resistivity data where one can see two broad peaks centered around 5 K and 150 K. This type of double-peaked structure is often observed in Kondo lattice compounds, demonstrating the presence of magnetically ordered

ground states. The broad maximum at low temperature is a characteristic of Kondo effect as it is usually done for resistivity data. It is a consequence of the spin-disorder scattering due to high localization of the $4f$ shell in Ce atom. But the broad hump at 150 K is an indication of the existence of strong crystal fields. As a $4f$ shell comes close to Fermi level, it produces a large resonant-scattering effect and hence the influence of crystalline fields on the Kondo effect has to be taken into account in conjunction with the spin and orbit exchange scattering. Thus presence of the double-peaked structure may be attributed to the combined influence of the crystal fields and Kondo effect. According to Cornut and Coqblin, this type of behaviour is expected for Kondo-type interaction in the presence of strong crystal field splitting [129]. In a limited temperature range ($5\text{ K} < T < 30\text{ K}$), resistivity can be fitted using the expression $\rho = \rho_0 + c_{ph}T - c_k \ln T$ [130], where the linear term, $c_{ph}T$ describes the electron-phonon scattering contribution and the third term corresponds to a magnetic (Kondo) contribution to the electrical resistivity, while c_k is the Kondo coefficient.

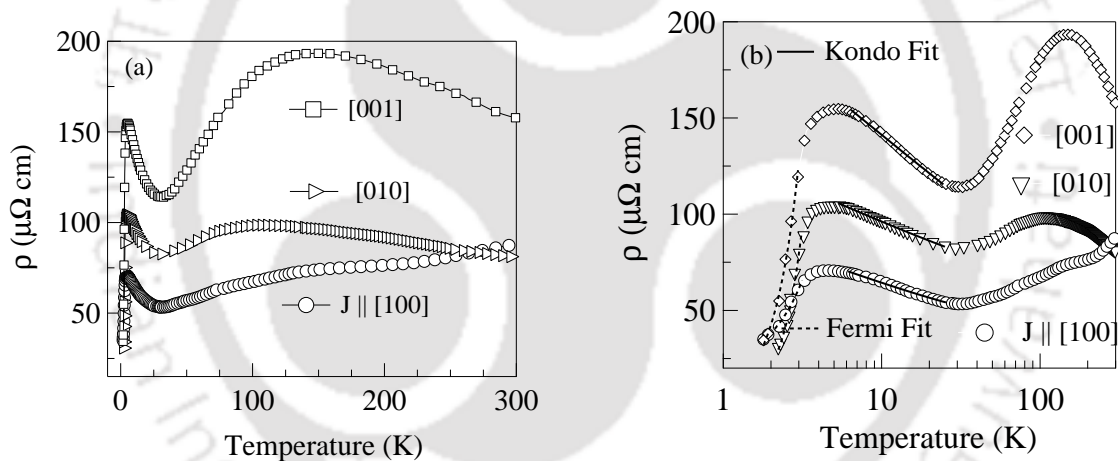


Figure 6.3: (a) The dc electrical resistivity in the temperature range from 1.8 to 300 K for $\text{Ce}_2\text{Ir}_3\text{Sn}_5$ along the [100], [010] and [001] directions. (b) Logarithmic temperature dependence of resistivity for $\text{Ce}_2\text{Ir}_3\text{Sn}_5$. Solid line at high temperature is a fit to the Kondo equation and the dotted line in low temperature part is a fit to Fermi liquid behaviour.

According to Kondo's theory [131], the Kondo coefficient is proportional to the density of states at the Fermi level. The best fit to the above equation are shown in Figure 6.3(b) (black solid line) and the estimated values are given in Table 3.1. The low temperature part of the resistivity curve (1.8 to 4 K) is fitted to the power law relation, $\rho = \rho_0 + AT^n$. The solid dashed line in the Figure 6.3(b) shows the Fermi fit and estimated

axis	Kondo Fit			Fermi Fit		
	ρ_0 $\mu\Omega\text{ cm}$	c_{ph} $\mu\Omega\text{ cm}/K$	c_k $\mu\Omega\text{ cm}$	ρ_0 $\mu\Omega\text{ cm}$	A $\mu\Omega\text{ cm}/K$	n
[100]	93	0.126	13	20	4.5	2.02
[010]	132	0.096	16	22	10	2.72
[001]	209	0.048	29	27	19.5	1.83

Table 6.1: The fitting parameters extracted from the resistivity data of Ce₂Ir₃Sn₅.

parameters are listed in Table 3.1. Here the exponent n is close to 2-3, which in principle signals the presence of electron-electron scattering.

6.3.2 Magnetic susceptibility studies

The temperature dependence of inverse magnetic susceptibility in the temperature range from 1.8 to 300 K measured in the field of 1 kOe along the three principle directions, that is, H parallel to [100], [010] and [001] directions, are shown in Figure 6.4. The inset shows the low temperature behaviour for susceptibility, χ . The low temperature $\chi(T)$ data display small upturn in susceptibility, which is the signature of the onset of an antiferromagnetic ordering in this material. The antiferromagnetic ordering temperature, $T_N = 3.6$ K is shown clearly as indicated by an arrow in Figure 6.4. The inverse dc susceptibility data over the temperature range from 100 to 300 K are very well fitted to the modified Curie-Weiss law, which is given by,

$$\chi = \chi_0 + \frac{C}{T - \Theta_P} \quad (6.1)$$

where χ_0 is the temperature independent term that includes the diamagnetic susceptibility (χ_{dia}), which arises due to the presence of ion cores, the Pauli spin susceptibility (χ_{pauli}) due to the conduction electrons, and the Landau susceptibility (χ_{Landau}) of the diamagnetic orbital contribution due to the conduction electrons. Θ_P is the Curie Weiss temperature and C is the Curie constant which can be written in terms of effective moments as C ($emu\text{ K/mol}$) = $\frac{N_A(\mu_{eff})^2 x}{3k_B} \approx \frac{(\mu_{eff})^2 x}{8}$, where x is the number of magnetic Rare earth ions (R) per formula, N_A is the Avogadro number and k_B is the Boltzmann

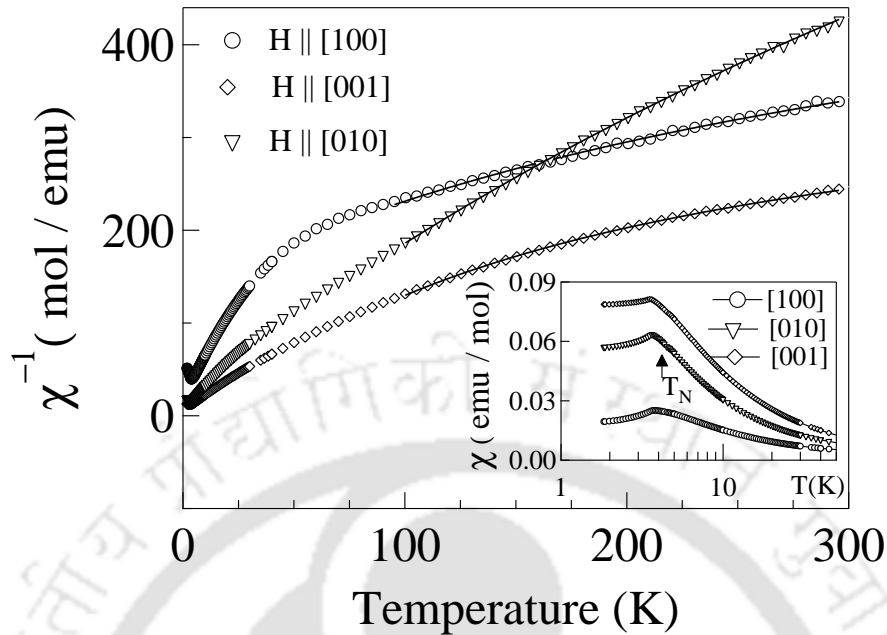


Figure 6.4: The inverse dc susceptibility in $\text{Ce}_2\text{Ir}_3\text{Sn}_5$ for $H \parallel [100]$, $[010]$ and $[001]$ directions in the temperature range from 1.8 K to 300 K in the field of 1 kOe. The inset shows the susceptibility (χ) behaviour in low temperature is shown in a log scale. The solid line is a fit to the Curie Weiss relation.

constant. The best fit curves to the model are shown in Figure 6.4.

axis	χ_0 (emu / mol K)	μ_{eff} (μ_B)	μ_{th} (μ_B)	Θ_p (K)
[100]	1.7×10^{-3}	2.74	2.54	-84
[010]	8.5×10^{-4}	2.64	2.54	5.4
[001]	2.6×10^{-3}	2.6	2.54	18.4

Table 6.2: $\text{Ce}_2\text{Ir}_3\text{Sn}_5$ compounds along three different principle axes, $[100]$, $[010]$ and $[001]$, obtained from the high temperature susceptibility fit to Curie Weiss relation. μ_{th} is the theoretical free ion value for trivalent rare earth ions.

The estimated values of the effective moments, $2.74 \mu_B/\text{Ce}$, $2.64 \mu_B/\text{Ce}$ and $2.7 \mu_B/\text{Ce}$ and Curie temperatures are -84 K, 5.4 K and 12.4 K along $[100]$, $[010]$ and $[001]$ directions respectively, are listed in Table 6.2. The estimated effective moment of $\text{Ce}_2\text{Ir}_3\text{Sn}_5$ is

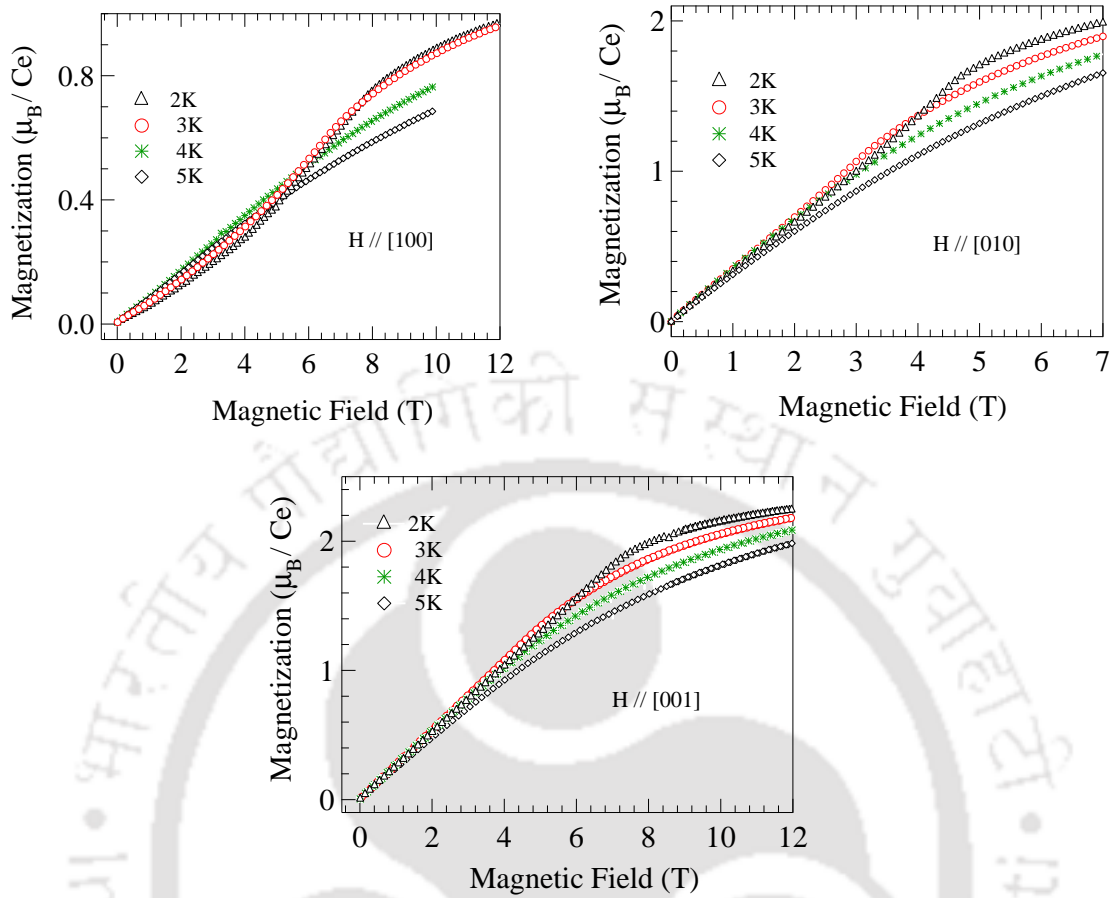


Figure 6.5: Isothermal magnetization curves of the magnetic field dependence in $\text{Ce}_2\text{Ir}_3\text{Sn}_5$ along [100], [010] and [001] axes.

found to be slightly large compared to a free ion value of Ce^{3+} ions $2.54 \mu_B$, the Russell-Saunders value, $\mu = g\mu_B [J(J+1)]^{1/2}$, thereby indicating a strong hybridization effect between f - d shell. The negative sign of the Curie temperature $\Theta_p = -84 \text{ K}$ for the [100] direction implies the presence of antiferromagnetic correlations. Nevertheless, the situation is rather different along the other two axes, namely [010] and [001] directions, where the positive Θ_p values indicate ferromagnetic correlations at high temperatures. Such an anisotropy is not unexpected, given the relatively low symmetry of the Ce sites, which further lowers the degeneracy of the Ce^{3+} quartet. The deviation of the $\chi^{-1}(T)$ curve from the straight line below 100 K can possibly be due to the crystal field effects and/or Kondo-type interactions.

The field dependence of isothermal magnetization at various temperatures for $\text{Ce}_2\text{Ir}_3\text{Sn}_5$ along three principle axes, with the field parallel to [100], [010] and [001] directions, are

shown in Figure 6.5. The non-linear behavior in M vs H at about transition temperature $T_N \sim 2-3$ K suggests of antiferromagnetic correlations. The magnetization data for [100] direction depicts “*S-like*” upward curvature indicating the presence of metamagnetic transitions, that occur from a state of low magnetization to one of relatively high magnetization. Here, the magnetization values at high fields are quite small, presumably due to the presence of Kondo effect, which quenches the magnetic ions. The non-linearity in M vs H above T_N indicate the possibility for short-range magnetic correlation (could arise due to splitting of energy levels by crystalline electric field (CEF)) that still persists above the Neel temperature. Above the transition temperature ($T > T_N$), the usual linear behavior in M vs H is consistent with the paramagnetic state of the compound.

6.3.3 Heat-capacity studies

The temperature dependence of the specific heat capacity of the single crystalline $\text{Ce}_2\text{Ir}_3\text{Sn}_5$ is shown in Figure 6.6. The plot of low temperature part of C/T vs T^2 is shown in inset of Figure 6.6(a). It clearly shows a jump at $T_N = 3.6$ K, confirming a

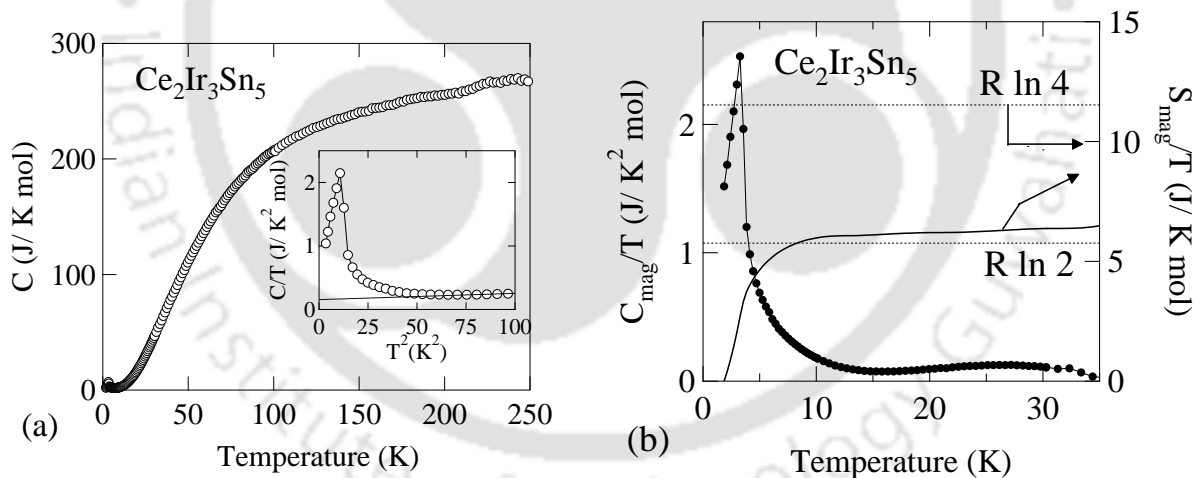


Figure 6.6: The temperature dependence of the specific heat capacity of $\text{Ce}_2\text{Ir}_3\text{Sn}_5$. In Fig (a), main panel shows C vs T in the temperature range between 1.8 to 250 K and the inset shows specific heat fit in C/T vs T^2 plot. (b) C_{mag}/T vs T of $\text{Ce}_2\text{Ir}_3\text{Sn}_5$. The calculated entropy is plotted on the right axis.

bulk magnetic ordering in this compound, as observed in the earlier studies on polycrystalline samples. The heat capacity data above the transition in the temperature range, ($6 < T < 10$ K), is fitted to the expression $C/T = \gamma + \beta T^2$, where γ is due to electronic

contribution and β is due to phononic contribution. The extrapolated value for Sommerfeld coefficient, γ is found to be 269 mJ/mol. K which classifies this compound as a moderate heavy-fermion antiferromagnet. The Debye temperature is estimated using the relation $\theta_D = \left(\frac{12\pi^4 N r k_B}{5\beta} \right)^{1/3}$ (where N is the Avogadro's number, r is the number of atoms per formula unit and k_B is the Boltzmann constant) was estimated to be $\theta_D = 255$ K. Figure 6.6(b) shows the C_{mag}/T vs T and calculated entropy, S_{mag} . At T_N , the value of S_{mag} reaches to 0.5 R ($\approx 73\%$ of $\ln 2$) anticipated for a doublet ground state. The reduced value of $R \ln 2$ further confirms the presence of Kondo effect in $\text{Ce}_2\text{Ir}_3\text{Sn}_5$.

6.4 Summary

Single crystal of $\text{Ce}_2\text{Ir}_3\text{Sn}_5$ is grown by Czochralski technique. The x-ray analysis confirms the orthorhombic $\text{Y}_2\text{Rh}_3\text{Sn}_5$ type crystal structure ($Cmc2_1$). The compound shows the Kondo behaviour which is clearly manifested by $-\ln(T)$ behaviour in resistivity. It also undergoes antiferromagnetic ordering at about 3.6 K which is confirmed from resistivity, dc susceptibility and heat capacity measurements. As a preliminary investigation of the Schottky-type anomaly observed in the specific heat data reveal a CEF-split doublet ground state. However, a detailed CEF analysis is desired for an improved understanding of the low lying energy states in $\text{Ce}_2\text{Ir}_3\text{Sn}_5$. The specific heat capacity data at low temperatures exhibit an enhanced Sommerfeld coefficient of 269 mJ/mol K^2 , thereby suggesting of the heavy fermion nature of $\text{Ce}_2\text{Ir}_3\text{Sn}_5$.

Chapter 7

Conclusion

In this chapter, we conclude this dissertation by summarizing our contributions and discussing the prospects of the future work. The thesis has explored the study on the interplay/competition between superconductivity (SC) and charge density wave (CDW) ordering in $\text{Lu}_2\text{Ir}_3\text{Si}_5$, and strongly correlated electron behavior in ternary class of rare earth intermetallic compounds, namely $\text{R}_2\text{Ir}_3\text{Sn}_5$ ($\text{R}=\text{La-Tm}$). The polycrystalline compound $\text{Lu}_2\text{Ir}_3\text{Si}_5$ with a three-dimensional orthorhombic $\text{U}_2\text{Co}_3\text{Si}_5$ type structure, shows a clear evidence of coexistence of SC and CDW order. The interplay and competition between the SC and CDW in the $\text{Lu}_2\text{Ir}_3\text{Si}_5$ have been undertaken by a detailed investigation on the evolution of the SC and CDW ordering in the pseudo-ternary alloy systems $(\text{Lu}_{1-x}\text{Sc}_x)_2\text{Ir}_3\text{Si}_5$, $\text{Lu}_2(\text{Ir}_{1-x}\text{Rh}_x)_3\text{Si}_5$ and $\text{Lu}_2\text{Ir}_3(\text{Si}_{1-x}\text{Ge}_x)_5$. The superconducting and CDW transition temperature have been determined by magnetic susceptibility and resistivity measurements and we have been able to construct a detailed temperature-concentration phase diagram for these systems. In $\text{Lu}_2\text{Ir}_3(\text{Si}_{1-x}\text{Ge}_x)_5$, we have found that a small concentration of Ge substitution at the Si sites suppresses the CDW strongly and simultaneously enhances the superconducting transition temperature. Afterwards, for higher concentration of Ge substitution, the CDW ordering starts to shift towards higher transition temperature, while, the SC transition temperature decreases. This non-monotonicity of the transition temperatures, T_{CDW} and T_{SC} as a function of Ge doping constitutes a new observation in this system. It is interesting to note that both SC and CDW ordering do not vanish even with 20% of the Ge substitution in the alloy. In our study, we also find that CDW is suppressed even though there is an expansion of the lattice volume. In addition, the suppression of the T_{SC} and enhancement of the T_{CDW} in certain alloys are related to the increase in density of states in its narrow d -band. Moreover, it is clear to see that the effect of ionic size plays an important role for the CDW transition in this class of materials.

We further examined the influence of the electronic density of states near the Fermi level in $\text{Lu}_2\text{Ir}_3\text{Si}_5$ by Rh substitution at the Ir sites, $\text{Lu}_2(\text{Ir}_{1-x}\text{Rh}_x)_3\text{Si}_5$. As Rh concentration increases, T_{CDW} enhances quasi-linearly while it suppresses T_{SC} . It reveals the fact that the increase in Rh concentration changes electron density at the FS. This fall in the density of states and impairment of the FS nesting account for the formation of chemical pressure. It therefore stabilizes the CDW formation in $\text{Lu}_2(\text{Ir}_{1-x}\text{Rh}_x)_3\text{Si}_5$ by the increase in d -bandwidth under chemical pressure. We also noted that both CDW and SC orderings are not noticeable at and above $x=30\%$ of Rh concentration, which accounts for the formation of the chemical pressure. These results suggest that the SC and CDW are strongly correlated and mutually incompatible to suppress each other in the $\text{Lu}_2\text{Ir}_3\text{Si}_5$ system. Furthermore, we have used Sc alloying at the Lu sites in $\text{Lu}_2\text{Ir}_3\text{Si}_5$, to study the effect of atomic disorder on both SC and CDW transitions. In $(\text{Lu}_{1-x}\text{Sc}_x)_2\text{Ir}_3\text{Si}_5$, it may be noted that the Sc substitution at Lu sites displays a slight change in CDW transition temperature, without affecting the SC ordering temperature too much. This indicates that the CDW is suppressed not because of the reduction of electron density of states at the Fermi level, but due to the difference in the atomic weights of Sc and Lu. It does not hinder the transfer of electrons of the FS from the CDW site to the SC site. We have identified that the Lu site is possibly related to the origin of CDW ordering in $\text{Lu}_2\text{Ir}_3\text{Si}_5$ system. In addition, our study reveals that the CDW anomalies in all the substituted alloys are broadened and smeared out, probably, by substitutional disorder effects. Also we find from the analysis of heat capacity data using a model of critical fluctuations in the vicinity of the CDW phase transition, that the CDW ordering gradually changes from a first-order-like to a second-order-like transition with the increase in concentration of the substituted alloys.

Next we extended the study of coexistence of CDW and SC in a single crystal of $\text{Lu}_2\text{Ir}_3\text{Si}_5$. We have prepared high quality single crystal of $\text{Lu}_2\text{Ir}_3\text{Si}_5$ for the first time. We observe superconductivity at 3.5 K and charge-density wave transition at high temperatures (≈ 235 K), accompanied by a huge thermal hysteresis. The heat capacity data show a very narrow and huge jump (55 J/mol K) across CDW transition signifying first order transition and the entropy involved here is substantial (0.33 R). The large specific heat jump is possibly due to fluctuation effects in the vicinity of CDW phase transition. The heat capacity data near the CDW transition has been analyzed by using the model of critical fluctuation combined with a mean-field contribution plus a smooth lattice background. The extracted parameters such as critical exponent, $\alpha \sim 2$, and the ratio of BCS coupling constant $\gamma^*/\gamma = 8.9$ are much higher than that of the mean field values $\alpha = 0.5$ and weak-coupling limit value for $\gamma^*/\gamma = 1.43$ respectively. This indicates strong coupling nature

of the CDW transition. In addition, superconducting parameters are deduced from the anisotropic Ginzburg-Landau theory. It is noted about type-II superconducting nature of $\text{Lu}_2\text{Ir}_3\text{Si}_5$ with a large $\kappa = \lambda/\xi$ value as well as the anisotropy parameter ($H_{C_2}^c/H_{C_2}^a$) of about 1.8, suggest of low anisotropy and hence a strong coupling between the planes.

In our studies, we have synthesized, for the first time, good quality of polycrystalline samples of the complete series of $\text{R}_2\text{Ir}_3\text{Sn}_5$ and investigated their low temperature magnetic properties using bulk measurements. Our work has revealed some interesting results:

- The polycrystalline samples are prepared for $\text{R} = \text{La}, \text{Ce} - \text{Nd}, \text{Gd} - \text{Tm}$. The compound $\text{La}_2\text{Ir}_3\text{Sn}_5$ crystallizes in the $\text{U}_2\text{Co}_3\text{Si}_5$ type orthorhombic crystal structure with the space group $Ibam$, whereas all the other compounds of $\text{R}_2\text{Ir}_3\text{Sn}_5$ ($\text{R} = \text{Ce} - \text{Nd}, \text{Gd} - \text{Tm}$) crystallize in the orthorhombic $\text{Y}_2\text{Rh}_3\text{Sn}_5$ ($Cmc2_1$) type of structures.
- $\text{La}_2\text{Ir}_3\text{Sn}_5$ do not show any transition down to 1.8 K. Most of the magnetic compounds $\text{Gd} - \text{Tm}$ in this series exhibit antiferromagnetic ordering below 10 K. The samples with $\text{Gd}_2\text{Ir}_3\text{Sn}_5$, $\text{Tb}_2\text{Ir}_3\text{Sn}_5$ and $\text{Dy}_2\text{Ir}_3\text{Sn}_5$ are found to be multiple transitions. $\text{Ce}_2\text{Ir}_3\text{Sn}_5$ shows a Kondo lattice behavior and undergoes an antiferromagnetic ordering at 2.9 K, while no magnetic ordering was observed in $\text{Pr}_2\text{Ir}_3\text{Sn}_5$ and $\text{Nd}_2\text{Ir}_3\text{Sn}_5$ down to 1.8 K.
- Schottky anomaly is noticed in most of the compounds, $\text{Pr}-\text{Nd}$ and $\text{Dy}-\text{Tm}$. A simple analysis of crystal field model is proposed to account for the contribution to the magnetic entropy and susceptibility of above mentioned samples. $\text{Pr}_2\text{Ir}_3\text{Sn}_5$ exhibits singlet ground state arising from CEF splitting of $(2J+1)$ levels of non-Krammer's Pr^{3+} ions whereas the Krammer's Nd^{3+} ions for $\text{Nd}_2\text{Ir}_3\text{Sn}_5$ exhibit doublet ground state, even though specific heat shows no signature of phase transition till the lowest available temperature. From the crystal field analysis, we also found that the ground state of Dy and Er compounds are doublets, while $\text{Tm}_2\text{Ir}_3\text{Sn}_5$ and $\text{Ho}_2\text{Ir}_3\text{Sn}_5$ show singlet ground states.
- The de Gennes scaling has been performed on $\text{R}_2\text{Ir}_3\text{Sn}_5$ compounds and found that T_N for most of the magnetic rare-earth samples of this series follow the scaling curve of spin quantum number S ($S + 1$), better than de Gennes scaling $(g_J - 1)^2 J (J + 1)$. Thus it implies that the magnetic transitions do not occur solely due to the RKKY interaction. In our study we find that the RKKY interaction need to be modified by including crystal field effects to account for the observed magnetic transition temperatures across the series.

Lastly, to study the competition between the Ruderman-Kittel-Kasuya-Yosida (RKKY) interaction and the Kondo effect, we have prepared the single crystal of $\text{Ce}_2\text{Ir}_3\text{Sn}_5$, for the first time to the best of our knowledge. From resistivity and magnetic susceptibility data, it clearly shows Kondo behavior and antiferromagnetic ordering. In the resistivity data, one can see two broad peaks centered around 5 and 150 K. This type of behavior is expected for Kondo-type interaction in the presence of strong crystal field splitting. The magnetic moment, as estimated from a Curie-Weiss fit of the high temperature susceptibility data is around $2.74 \mu_B/\text{Ce}$. This value is found to be larger compared to the free ion value of Ce^{3+} ions $2.54 \mu_B$, indicating a strong hybridization effect between the f - d shells. Besides, the specific heat capacity data at low temperatures exhibit an enhanced Sommerfeld coefficient of 269 mJ/mol K^2 , thereby suggesting of a heavy fermion nature of $\text{Ce}_2\text{Ir}_3\text{Sn}_5$.

In the present thesis we have carried out a detailed analysis on charge density wave, superconductivity and magnetic behaviour of ternary rare earth intermetallic compounds $\text{Lu}_2\text{Ir}_3\text{Si}_5$ and $\text{R}_2\text{Ir}_3\text{Sn}_5$ ($\text{R}=\text{La-Tm}$). The results of this dissertation point to different possibilities for further work. As the most important and interesting issues the following can be mentioned:

- The compound $\text{Lu}_2\text{Ir}_3\text{Si}_5$ shows the CDW transition around 180 K. For this, I-V characteristic study of the compound can constitute future plan. For a CDW transition this is expected to give a non-linear behaviour below the transition temperature and the scaling relationships will also be consistent with the other CDW materials.
- One can construct the phase diagram of $\text{Lu}_2\text{Ir}_3\text{Si}_5$. For this, a high pressure study (resistivity and susceptibility measurement) on this compound is required.
- Since the CDW transition accompanied with structural deformation, the single crystal XRD analysis and the electronic band structure calculations are required for a better understanding of the unique phase transition found in $\text{Lu}_2\text{Ir}_3\text{Si}_5$.
- Further, experimentation on single crystal $\text{Lu}_2\text{Ir}_3\text{Si}_5$ is required. This concerns the structural fluctuation (synchrotron radiation), the lattice softening (in elastic neutron scattering) and NMR measurements that are expected to a better understanding of CDW behaviour beyond the weak-coupling limit.
- Besides, there exists a series of magnetic rare earth 2-3-5 compounds that allow a new investigation of the coexistence and or/competition of magnetism and CDW.
- In an isostructural, isoelectronic series of rare earth compound $\text{R}_2\text{Ir}_3\text{Sn}_5$, the preliminary studies reveal about rich magnetic phase diagram between d and f moments.

This gives motivation for neutron diffraction studies on polycrystalline samples of $R_2Ir_3Sn_5$. The study is needed for a better understanding of magnetic structure of the compounds.

- Synthesis and measurements on single crystalline compounds of $R_2Ir_3Sn_5$ are important to substantiate our understanding of the properties, which we have derived from polycrystalline materials.





Bibliography

- [1] P. Rogl, “*Handbook of Physics and Chemistry of Rare Earths*”, edited by K. A. Gschneidner, Jr. and L. Eyring, Elsevier Science Publishers/North-Holland, Amsterdam, Vol 7, pp. 1-264, (1984).
- [2] J. Leciejewicz and A. Szytula, “*Handbook of Physics and Chemistry of Rare Earths*”, edited by K. A. Gschneidner, Jr. and L. Eyring Elsevier Science Publishers/North-Holland, Amsterdam, Vol 12, pp. 133, (1989).
- [3] C. B. Vining and R. N. Shelton, *Phys. Rev. B* **28**, 2732 (1983).
- [4] H. F. Braun, *Phys. Lett.* **75A**, 386 (1980).
- [5] H. F. Braun, C. U. Segre, F. Acker, M. Rosenberg, S. Dey and U. Deppe, *J. Magn. Magn. Mater.* **25**, 117 (1981).
- [6] A. R. Moodenbaugh, D. E. Cox, and H. F. Braun, *Phys. Rev. B* **25**, 4702 (1981).
- [7] H.F. Braun, “*Ternary superconductor*”, edited by G. K. Shenoy, B. D. Dunlop and F. Y. Fradin, (North- Holland, Amsterdam, 1980) P.225.
- [8] Yogesh Singh, D. Pal and S. Ramakrishnan, *Phys. Rev. B* **70**, 064403 (2004).
- [9] H. D. Yang, P. Klavins, and R. N. Shelton, *Phys. Rev. B* **43**, 7688 (1991).
- [10] Y. Kamihara, Takumi Watanabe, Masahiro Hirano, and Hideo Hosono, *J. Am. Chem. Soc.* **130**, 3296 (2008).
- [11] I.I. Mazin and M.D. Johannes, *Nature Phys.* **5**, 141 (2008).
- [12] F. Han, Fei Han, Xiyu Zhu, Peng Cheng, Gang Mu, Ying Jia, Lei Fang, Yonglei Wang, Huiqian Luo, Bin Zeng, Bing Shen, Lei Shan, Cong Ren, and Hai-Hu Wen, *Phys. Rev. B* **80**, 024506 (2009).
- [13] R. E. Peierls, “*Quantum Theory of Solids*” (Oxford University Press, New York, 1955).

- [14] G. Gruner, “*Density Waves in Solids*” (Addison-Wesley, Reading, 1994).
- [15] R. C. Morris, Phys. Rev. Lett. **34**, 1164 (1975)
- [16] E. Revolinski, G. A. Spiering And D. J. Beerntsen, J. Phys. Chem. Solids **26**, 1029 (1965).
- [17] Kazushige Machida and Masaru Kato , Phys. Rev. B **36**, 854 (1987).
- [18] Yogesh Singh, R. Nirmala, S. Ramakrishnan, and S. K. Malik , Phys. Rev. B **72**, 045106 (2005).
- [19] Yogesh Singh, Dilip Pal, S. Ramakrishnan, A. M. Awasthi, and S. K. Malik, Phys. Rev. B **71**, 045109 (2005).
- [20] R. N. Shelton, L. S. Hausermann-Berg, P. Klavins, H. D. Yang, M. S. Anderson and C. A. Swenson, Phys. Rev. B **34**, 4590 (1986).
- [21] K. Miyazawa, K. Kihou¹, P. M. Shirage¹, Chul- Ho Lee, H. Kito, H. Eisaki and A. Iyo, Journal of the Physical Society of Japan **78**, 034712 (2009).
- [22] M. S. Torikachvili, S. L. Bud’ko, N. Ni, P. C. Canfield, Phys. Rev. Lett. **101**, 057006 (2008) .
- [23] K. H. J. Buschow and F. R. De Boer, “*Physics of Magnetism and Magnetic Materials*”, Kluwer Academic Publishers (2004).
- [24] Yoshichika Ōnuki, Akira Hasegawa, “*Handbook of Physics and Chemistry of Rare Earths*”, edited by K. A. Gschneidner, Jr. and L. Eyring Elsevier Science Publishers/North-Holland, Amsterdam, Vol 20, pp. 3, (1995).
- [25] Karl A Gschneidner Jr, L Eyring; “*Handbook of physics and chemistry of rare earths*” vol. 1; North-Holland publishing company (1978).
- [26] M. A. Ruderman and C. Kittel; Phys. Rev. **96**; 99-102 (1954).
- [27] T. Kasuya; Progress of Theoretical Physics - Japan **16**; 45 (1956).
- [28] K. Yosida; Physical Review **106**; 893-898 (1957).
- [29] Stephen Blundell; Book on “*Magnetism in condensed matter*; Oxford mater series in condensed matter physics, Oxford university press (2001).
- [30] M. Coledea, M. Neumann, M. Demeter; Journal of Alloys and Compounds **323-324**, 431-434 (2001).
- [31] Laurent Cario, Pierre Palvadeau, Alain Lafond, Catherine Deudon, Yves Moeelo, Benoit Corraze, Alain Meerschaut; Chemistry of Materials **15**(4), 943-950 (2003).

- [32] Yutaka Kishimoto, Yu Kawasaki, Takashi Ohno; Physical Letters A **317**; 308-314 (2003).
- [33] J. Kondo, Prog. Theor. Phys. **32**, 37 (1964).
- [34] Charles P. Poole Jr., Horacio A. Farach, Richard J. Creswick and Ruslan Prozorov, "*Superconductivity*", Elsevier academic press, second edition (2007); Rolf. E. Hummel, "*Electronic properties of Materials*", Springer publishers, Third edition (2001).;
- [35] Satoshi Sasaki, M. Kriener, Kouji Segawa, Keiji Yada, Yukio Tanaka, Masatoshi Sato, Yoichi Ando, Phys. Rev. Lett. **107**, 217001 (2011)
- [36] J. M. Vandenberg and B. T. Matthias, Proc. Natl. Acad. Sci., USA, **74**, 1336 (1977).
- [37] H. F. Braun, J. Less-Common Met. **100**, 105 (1984).
- [38] H. F. Braun, C. U. Segree, Solid State Comm. **35**, 735 (1980).
- [39] G. P. Meisner, Physica 108B, **763** (1981).
- [40] "*Superconductivity in Ternary Compounds*" Vol.II edited by M.B. Maple and ϕ . Fisher, Springer-Verlag, Berlin (1984).
- [41] H. E. Horng and R. N. Shelton "*Ternary Superconductors*", edited by G. K. Shenoy, B. D. Dunlap and F. Y. Fradin, North Holland, Amsterdam, p.213 (1981).
- [42] R. W. McCullum, D. C. Johnston, R. N. Shelton "*Ternary Superconductors*", edited by G. K. Shenoy, B. D. Dunlap and F. Y. Fradin, North Holland, Amsterdam, p.99 (1981).
- [43] T. Tamegai, Y. Nakajima, T. Nakagawa, G. J. Li, and H. Harima, Journal of Physics: Conference Series **150**, 052264 (2009)
- [44] G. Gruner, Reviews of Modern Phys. **60**, 1129 (1988).
- [45] K. Krogmann and D. Hausen, Z. Anorg. Allg. Chem. **358**, 67 (1968).
- [46] J. L. Hodeau, M. Marezio, C. Roucau, R. Ayroles, A. Meerschaut, J. Rouxel and P Monceau, J. Phys. C: Solid State Phys., **11** (1978).
- [47] N. Ru and I. R. Fisher, Phys. Rev. B **73**, 033101 (2006).
- [48] B. Becker, N. G. Patil, S. Ramakrishnan, A. A. Menovsky, G. J. Nieuwenhuys, J. A. Mydosh, M. Kohgi, and K. Iwasa, Phys. Rev. B **59**, 7266 (1999).

- [49] F. J. Disalvo, J. V. Waszczak and K. Yamaya, *J. Phys. Chem. Solids*, **41**, 1311-1313 (1980).
- [50] P. Monceau, *Physica* 109 & **110B**, 1890-1900 (1982).
- [51] S. Nagata, T. Aochi, T. Abe, S. Ebisu, T. Hagino, Y. Seki, K. Tsutsumi, *J. Phys. Chem. Solids* **53**, 1259 (1992).
- [52] T. Kumakura, H. Tan, T. Handa, M. Morishita, H. Fukuyama, *Czech. J. Phys.* **46**, 2611 (1996).
- [53] D. Jaiswai, A. A. Tulapurkar, S. Ramakrishnan, A. K. Grover, G. J Nieuwenhuys, Mydosh, *Phys. B* **312**, 142 (2002).
- [54] R.C Morris, R. C., *Phys. Rev. Lett.* **34**, 1164 (1975).
- [55] H. Suhl, B. T. Matthias, and L. R. Walker, *Phys. Rev. Lett.* **3**, 12 (1959).
- [56] M. Nunezregueiro, J. M. Mignot, M. Jaime, D. Castello, P. Monceau, *Synthet. Metals* **56**, 2653 (1993).
- [57] L. Fang, Y. Wang, P. Y. Zou, L. Tang, Z. Xu, H. Chen, C. Dong, L. Shan, H. H Wen, *Phys. Rev. B* **72**, 14534 (2005).
- [58] C. Berthier, P. Molinie and D. Jerome, *Solid State Commn.* **18**, 1393 (1976).
- [59] Kazushige Machida and Masaru Kato, *Phys. Rev. B* **36**, 854 (1987).
- [60] M. Ichimura, M. Fujita and K. Nakao, *Phys. Rev. B* **43**, 175 (1991).
- [61] F. Han, Fei Han, Xiyu Zhu, Peng Cheng, Gang Mu, Ying Jia, Lei Fang, Yonglei Wang, Huiqian Luo, Bin Zeng, Bing Shen, Lei Shan, Cong Ren, and Hai-Hu Wen, *Phys. Rev. B* **80**, 024506 (2009).
- [62] G. F. Chen, Z. Li, D. Wu, G. Li, W. Z. Hu, J. Dong, P. Zheng, J. L. Luo, and N. L. Wang, *Phys. Rev. Lett.* **100**, 247002 (2008).
- [63] Xiangde Zhu, Hechang Lei, and C. Petrovic, *Phys. Rev. Lett.* **106**, 246404 (2011).
- [64] Proceedings of National Workshop on Advanced Methods for Materials Characterization; Organised by Materials Research Society of India (2004).
- [65] N.W. Ashcroft and N.D. Mermin, *Solid State Physics* (Thompson), 2003 edition.

- [66] <http://www.ill.eu/sites/fullprof/>
- [67] Review of Scientific Instruments **30**; 548-547 (1959).
- [68] J. S. Hwang, K.J. Lin and C Tein, Rev. of Scientific Instruments **68**, (1997) 94.
- [69] T. Hatakeyama and Z. Liu, "*Handbook of Thermal Analysis*", John Wiley & Sons, Chichister (1998).
- [70] Y. K. Kuo and K. M. Sivakumar, T. H. Su and C. S. Lue, Phys. Rev. B **74**, 045115 (2006).
- [71] M. H. Lee, C. H. Chen, M.-W. Chu, C. S. Lue, and Y. K. Kuo, Phys. Rev. B **83**, 155121 (2011).
- [72] Y. Singh, D. Pal, and S. Ramakrishnan, Phys. Rev. B **70**, 064403 (2004).
- [73] K. Ghosh, S. Ramakrishnan, and G. Chandra, Phys. Rev. B **48**, 4152 (1993).
- [74] R. N. Shelton, L. S. Hausermann-Berg, P. Klavins, H. D. Yang, M. S. Anderson and C. A. Swenson, Phys. Rev. B **34**, 4590 (1986).
- [75] Y. Singh, and S. Ramakrishnan, Phys. Rev. B **69**, 174423 (2004).
- [76] J. A. Gotaas, J. W. Lynn, R. N. Shelton, P. Klavins, and H. F. Braun, Phys. Rev. B **36**, 7277 (1987).
- [77] S. Ramakrishnan, N. G. Patil, A. D. Chinchure and V. R. Marthe, Phys. Rev. B **64**, 064514 (2001).
- [78] Juan Rodriguez-Carvajal, Phys. B (Amsterdam) **55**, 192 (1993).
- [79] Y. -K. Kuo, F. H. Hsu, H. H. Li, H. L. Huang, C. W. Huang, C. S. Lue, and H. D. Yang, Phys. Rev. B **67**, 195101 (2003).
- [80] Y. -K. Kuo, C. S. Lue, F. H. Hsu, H. H. Li, and H. D. Yang, Phys. Rev. B **64** 125124 (2001).
- [81] R. A. Craven, S. F. Meyer, Phy. Rev. B **16**, 4583 (1977).
- [82] R. S. Kwok and G. Gruner, S. E. Brown, Phys. Rev. Lett. **65**, 365-368 (1990).
- [83] R. S. Kwok and S. E. Brown, Phys. Rev. Lett. **63**, 895-898 (1989).
- [84] M. Chung, Y.-K. Kuo, X. Zhang, E. Figueroa, J. W. Brill, and G. Mozurkewich, Synth. Met. **71**, 1891 (1995).

- [85] J L Hodeau, M Marezio, C Roucau, R Ayrolest, A Meerschautg, J Rouxels and P Monceau, *J. Phys. C: Solid State Phys.* **11**, (1978).
- [86] Friedel J, "*The Physics of Metals*", Edited by ZIMAN J. M, Chap. 8. Cambridge University Press (1969).
- [87] R.H. Friend, D. Jérôme, D.M. Schleich, P. Molinié, *Solid State Communications* **27**, 169-173 (1978).
- [88] F. Galli, S. Ramakrishnan, T. Taniguchi, G. J. Nieuwenhuys, J. A. Mydosh, S. Geupe, J. L udecke and S. van Smaalen, *Phys. Rev. Lett.* **85**, 158 (2000).
- [89] N. R. Werthamer, E. Helfand, and P. C. Hohenberg, *Phys. Rev.* **147**, 295 (1966).
- [90] J. W. Brill, M. Chung, Y.-K. Kuo, X. Zhan, and E. Figueroa, *Phys. Rev. Lett.* **74**, 1182 (1995).
- [91] S. Tomi, K. Biljakovi, D. Djurek, J.R. Cooper, P. Monceau, A. Meerschaut, *Solid State Commun.* **38** (1981) 109.
- [92] M. Chung, Y.-K. Kuo, Zhigang Xu, L. E. DeLong, and J. W. Brill, *Phys. Rev. B* **50**, 1329 (1994).
- [93] A. R. Moodenbaugh, D. E. Cox, and H. F. Braun, *Phys. Rev. B* **25**, 4702 (1982).
- [94] Tadataka Watanabe, Hiroki Sasame, Hiroaki Okuyama, Kouichi Takase, and Yoshiki Takano, *Phys. Rev. B* **80**, 100502(R) (2009).
- [95] S. Noguchi and K. Okuda, *Physica B* **194-196**, 1975 (1994).
- [96] Y. Muro, Y. Yamane, M. S. Kim, T. Takabatake, C. Godart, and P. Rogl, *J. Phys. Soc. Jpn.* **72**, 1745 (2003).
- [97] N. G. Patil and S. Ramakrishnan, *Phys. Rev. B* **59**, 12054 (1999).
- [98] Yogesh Singh and S. Ramakrishnan, *Phys. Rev. B* **69**, 174423 (2004).
- [99] V. K. Anand, Z. Hossain, and C. Geibel, *Phys. Rev. B* **77**, 184407 (2008).
- [100] R. Pöttgen, A. Lang, R.-D. Hoffmann, B. Knen, G. Kotzyba, R. Millmann, B. D. Mosel, C. Rosenhahn, *Z. Kristallogr.* **214**, 143-150 (1999).
- [101] Y. V. Galadzhun, R. D. Hoffmann, R. Pöttgen, M. Adam, *J. Solid State Chem.* **148**, 425-732 (1999).

- [102] E. Parthe and B. Chabot, “ *Handbook of Physics and Chemistry of Rare Earths*”, (Ref. 1, pp. 113-333).
- [103] M. Meot-Meyer, G. Venturini, B. Malaman, J. Seinmetz and B. Roques, Mater. Res. Bull. **18**, 1181 (1984).
- [104] N. G. Patil and S. Ramakrishnan, Phys. Rev. B **59**, 14 (1999).
- [105] S. Ramakrishnan, K. Ghosh and Girish Chandra, Phys. Rev. B **45**, 10 769 (1992).
- [106] S. Ghosh, S. Ramakrishnan and Girish Chandra, Phys. Rev. B **48**, 10 440 (1993).
- [107] H. Wiesmann, M. Gurvitch, H. Lutz, A. K. Ghosh, B. Schwarz, M. Strongin, P. B. Allen and J. W. Halley, Phys. Rev. Lett. **38**, 782 (1977).
- [108] B. Chakraborty and P. B. Allen, Phys. Rev. Lett. **38**, 372 (1979).
- [109] Charles Kittel, “ *Introduction to solid state physics*”, Seventh edition, Chap. 6. (2006).
- [110] P. C. Canfield, J. D. Thompson, W. P. Beyermann, A. Lacerda, M. F. Hundley, E. Peterson, Z. Fisk and H. R. Ott, J. Appl. Phys. **70**, 5800 (1991).
- [111] M. Bouvier, P. Lethuillier and D. Schmitt, Phys. Rev. B **43**, 13137 (1991).
- [112] S. Ramakrishnan, N. G. Patil, Aravind D. Chinchure and V. R. Marathe, Phys. Rev. B **64**, 064514 (2001).
- [113] V. R. Marathe and S. Mitra, J. Chem. Phys. **78**, 915 (1983).
- [114] C. Cascales, P. Porcher and R. Saez-Puche, J. Phys. Chem. Solids **54**, 1471-1474 (1993).
- [115] N. G. Patil and S. Ramakrishnan, Phys. Rev. B **56**, 6 (1997).
- [116] T. Moriya and T. Takimoto, J. Phys. Soc. Jpn. **8**, 960 (1995).
- [117] G. G. Lonzarich, “ *The Electron*”, edited by M. Springford, Cambridge University Press, Cambridge, Chap. 6 (1997).
- [118] L. Klein, L. Antognazza, T. M. Geballe, M. R. Beasley and A. Kapitulnik, Physics B **261**, 431 (1999).
- [119] R. J. Birgeneau, M. T. Hutchings, J. M. Baker, and J. D. Riley, J. Appl. Phys. **40**, 1070 (1969).

- [120] D. C. Mattis, "*Theory of Magnetism*" (Harper & Row, New York, 1965).
- [121] P. G. de Gennes, J. Phys. Radium **23**, 510 (1962).
- [122] D. R. Noakes and G. K. Shenoy, Phys. Lett. **91A**, 35 (1982).
- [123] J. M. Lawrence, P. Riseborough and R. D. Parks, Rep. Progr. Phys. **44**, 1 (1981) [SPIRES].
- [124] D. T. Adroja and S. K. Malik, J. Magn. Magn. Mater. **100**, 126 (1991) [CAS].
- [125] E. Bauer, Adv. Phys. **40**, 417 (1991).
- [126] A. C. Hewson, "*The Kondo Problem to Heavy Fermions*", Cambridge University Press, Cambridge, England (1993).
- [127] Yasuyuki Ishii, Masashi Kosaka, Hideki Abe, Hideaki Kitazawa, Giyuu Kido, Yoshiya Uwatoko, J. Magn. Magn. Mater. **277**, 60 (2004).
- [128] G. Venturini, M. Meot-Meyer, S.F. Marcche, B. Malaman and B. Roques, Mat. Res. Bull. **21** 33 (1986).
- [129] B. Cornut, B. Coqblin, Phys. Rev. B **5**, 4542 (1972).
- [130] M A López de la Torre, M A Arranz, M Ellerby and K A McEwen, J. Phys.: Condens. Matter. **15**, 2599 (2003).
- [131] Kondo J, Prog. Theor. Phys. Japan **32**, 37 (1964).

Vitae

Sangeetha N. S. was born on 30 May, 1983 in Kerala, India. She obtained her Bachelors in Physics from Sree Krishna College, Guruvayoor, Kerala and completed Masters in Physics from C. M. S. College, Kottayam, Kerala. She pursued her research career with experimental condensed matter physics, at Department of Physics, IITG under the supervision of Dr. Dilip Pal and Prof. Saurabh Basu. Her current research interests include low temperature magnetism, superconductivity, charge density wave and strongly correlated electron systems.

